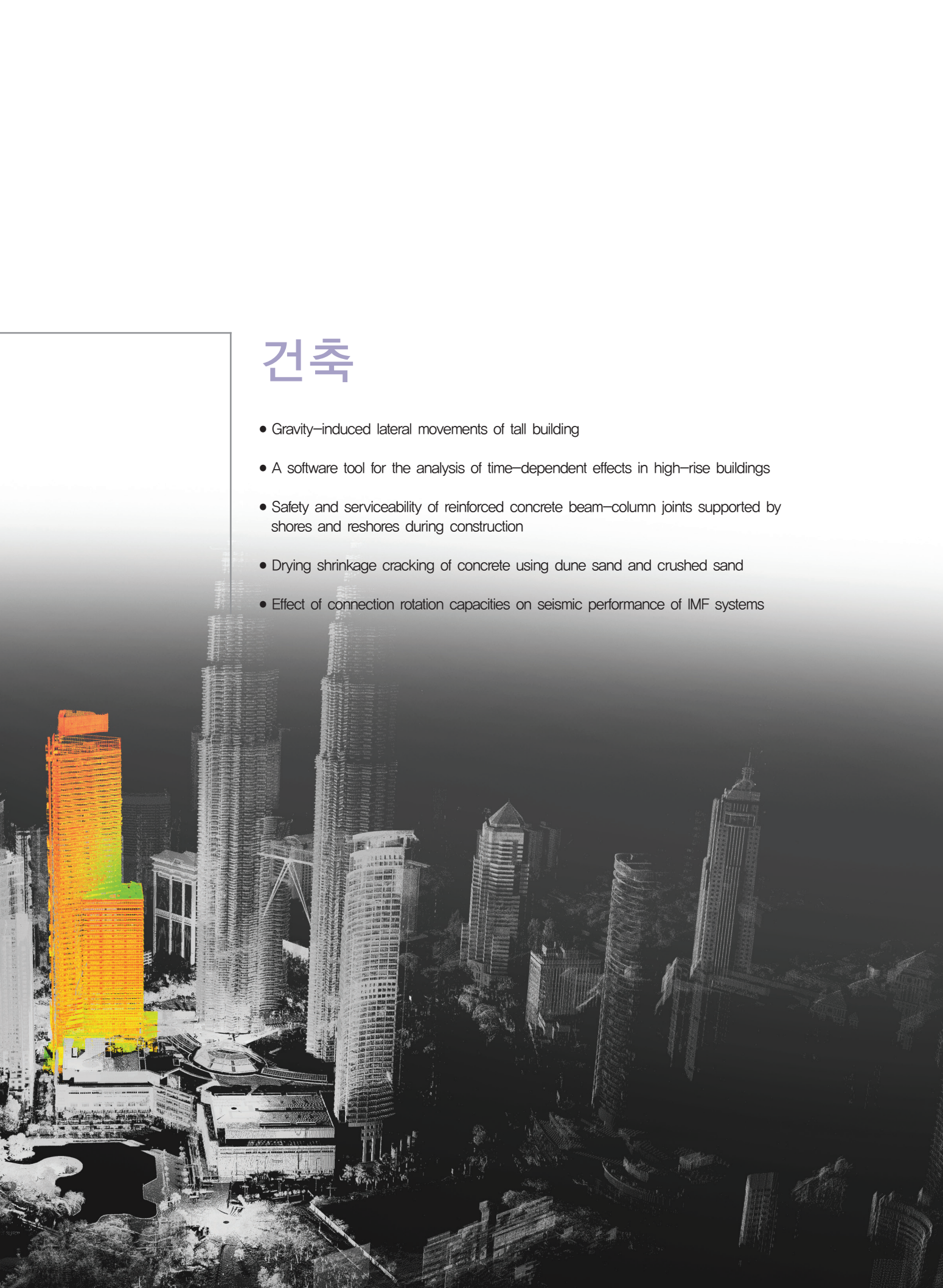
02

Daewoo Construction Technology Report



건축

- Gravity-induced lateral movements of tall building
- A software tool for the analysis of time-dependent effects in high-rise buildings
- Safety and serviceability of reinforced concrete beam-column joints supported by shores and reshores during construction
- Drying shrinkage cracking of concrete using dune sand and crushed sand
- Effect of connection rotation capacities on seismic performance of IMF systems



Gravity-induced lateral movements of tall building

Sungho Lee
Architectural Research Team, Principal Researcher
sungho.lee@daewooenc.com

본 논문은 2016년 Structures and Buildings VOL.169, NO. 9, 702–714에 게재되었던 논문을 재게재한 것입니다.

Abstract

High-rise buildings move during construction due to time-dependent material properties of concrete (creep and shrinkage), construction sequences and structural shapes. The building movements including vertical and horizontal displacements result from the sum of axial and lateral deformations of vertical members at each level. In addition to the vertical shortenings, the lateral movement induced by differential shortening can have adverse effects on the construction tolerances and serviceability of non-structural elements such as lifts and curtain walls. A construction stage analysis method was developed to predict deviation from verticality induced by shortening including the effect of creep and shrinkage. The algorithm of construction stage analysis was combined with FE analysis program. The developed method was used to predict the lateral movement of 58 story reinforced concrete building which was constructed in Kuala Lumpur, Malaysia. Field three dimensional laser scanning survey was carried out to verify the prediction results and satisfactory agreement was obtained.

Keywords : Columns; Concrete structures; Field testing & monitoring

1_INTRODUCTION

Aging effects of concrete such as creep and shrinkage are considered in the design and construction of bridges, of which deformation-related structural stability during construction is as much important as for the finished structure (Grabow, 2004). This requirement is equally applicable to high-rise buildings. Today's high-rise buildings usually exhibit some extraordinary features such as super-tall height, elevation set-backs, overhangs, or free-form exterior surface, all of which makes the construction difficult, complex, and even unsafe at some construction stages. In addition to the elaborately planned construction sequence, prediction and monitoring of the building's movement during construction and after completion are required for precise and safe construction. The building movement in this context means the vertical and horizontal displacements which result from the sum of axial and lateral deformations of vertical members at each level. The major factors affecting building movement include loads, geometry, and time-dependent material properties of concrete, and sequence of construction.

The building movement has an impact on the load distribution to the structural elements and can cause substantial serviceability problems. The shortened vertical structural elements inevitably transfer some forces to neighboring non-structural elements such as partitions, cladding, piping, and lift rails, which are not designed to carry the additional loads. The effects of differential

shortening between adjacent vertical members are evident particularly in tall buildings with central core and perimeter columns. As the central core is generally less stressed than the perimeter columns and may be constructed in advance using climbing form, the amount of shortening is much less than that of the perimeter columns. For buildings with mass eccentricity or irregularity, the differential shortening combined with the applied moment could also make the building move laterally since accumulated differential shortenings cause curvature, which is integrated along the height of the building resulting in vertical and lateral movements depending on the symmetry and arrangements of the vertical elements. Lateral displacements induced by lateral loads under service states transiently remain in the structures because when the effects of the lateral loads disappear, the deformations are generally recovered. However, the lateral movement induced from the differential shortening permanently remains in the building. This lateral movements gradually develops during construction and constantly increases after its completion due to time-dependent creep and shrinkage properties of the concrete (Lavery et al., 2015). These can have adverse effects on the serviceability of non-structural elements such as partitions, lifts and curtain walls. Therefore, the lateral movement induced by differential shortening as well as vertical shortening should be accurately predicted for the high-rise buildings.

Most of the previous research studies were focused on the prediction of the vertical shortenings only. In an earlier study (Fintel et al., 1986), individual vertical members were analyzed without the restraining actions of horizontal members and deviation from verticality was not considered. Although two dimensional frame analysis including time-dependent properties of concrete was developed in recent researches (Lu et al., 2013; Kurc et al., 2013; Kim, 2013; Maru et al., 2001; and Chiorino et al., 2011), the prediction and monitoring of the lateral movement induced by differential shortenings have not been adequately researched.

This research describes a theoretical study on the behavior of the lateral movement induced by differential shortenings, and proposes a construction stage analysis method including the time-dependent effects of creep and shrinkage. The developed analysis method was used to predict the horizontal deviation from verticality for a 58 story reinforced concrete building. The time-dependent properties causing the horizontal deviation were discussed. Finally, the analysis results were verified against field survey data and good correlation was found.

2_TIME-DEPENDENT CONCRET PROPERTIES

There are two main issues which distinguish construction stage analysis from ordinary structural analysis - consideration of construction sequences and the effect of time-dependent properties of concrete that happen during construction. Not only the internal forces and deformations of individual structural members at a particular floor at the time of loading but also those of the overall structure at final stage which become different as construction progresses. The discrepancies become significant as the number of floors increases. The accumulated differences in forces and deformations in structural members, when comparing between construction stage analysis and ordinary structural analysis, get bigger due to the effect of creep and shrinkage of concrete that occur during the long-term construction period of tall buildings. While elastic deformations are simply calculated from the applied load and the modulus of elasticity, creep and shrinkage deformations are influenced by various factors such as member size and shape, reinforcement ratio, relative humidity, modulus of elasticity, duration of load application, and age of curing at the start of loading. Input values for concrete properties during construction stage analysis are based on provisions from codes of practices and published papers. Examples of codes of practices are from the committees of ACI 209 (2008) and Eurocode 2. B3 (Bazant and Murphy, 1995) and GL2000 (Gardner, 2004) models are generally accepted models for the prediction of creep and shrinkage. B3 and GL2000 models are different from each other and also from the codes of practices in terms of the pattern of development of deformation according to elapsed time. Although these theoretical models for creep and shrinkage give a good guideline at the preliminary stage of construction stage analysis, tests on concrete

used in the actual construction should be performed as early as the mix design of the concrete is established due to the following reasons: Firstly, laboratory database for the theoretical models is relatively outdated in terms of current progress of technology development in the concrete industry. Concrete with high-strength and multi-performance has quite different creep and shrinkage properties from ordinary normal strength concrete; Secondly, measured database for the theoretical models is mainly obtained from bridges, not from buildings. The effect of creep and shrinkage on bridge girders is the increased deflection, while that on buildings is related to the axial shortening of concrete columns, which are usually acting in compression during its entire life. Since the structural behavior of bending and compression is different, the creep behavior under sustained loading should also be differentiated. The material tests for creep and shrinkage are conducted at least for three months long in climate-controlled chambers where the temperature and relative humidity can be maintained at levels specified in the codes. Values of specific creep and ultimate shrinkage are derived from nonlinear regression analysis on the test results.

3_TIME-DEPENDENT LATERAL MOVEMENT

In a rigid frame, the differential shortening between vertical members cause the horizontal members such as slabs and beams to tilt with resulting additional moment and shear forces due to differential displacement. To find the relations between differential shortening and lateral movement, consider a simple rigid frame, where differential shortening (Δ_{Diff}) is developed as shown in Figure1.

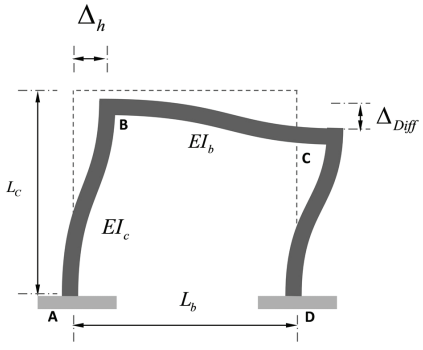


Fig. 1. Deformation of a rigid frame with differential shortening between columns

$$M_B = \frac{6E_cI_b}{L_b^2}\Delta_{Diff} \tag{1}$$

According to the condition of the end rotation (i.e. boundary condition) at vertical member and the principle of moment area theorem (Chajes, 1990), the horizontal deviation from verticality caused by the differential shortening can be written as Eq. (2).

$$\Delta_h = \left(\frac{M_B}{E_cI_c}\times L_c\times\frac{1}{2}\right)\times\frac{L_c}{3} - \left(\frac{M_A}{E_cI_c}\times L_c\times\frac{1}{2}\right)\times\frac{2L_c}{3} = -\frac{M_BL_c^2}{6E_cI_c} = \frac{I_b/L_b^2}{I_c/L_c^2}\Delta_{Diff} \tag{2}$$

From Eq. (2), it is noted that the differential shortening is an important factor that affects the lateral movement of high-rise building in addition to that caused by lateral loads. The differential shortening in tall buildings results from the differences between axial shortenings of adjacent columns and walls. Time-dependent effects such as creep and shrinkage influence axial shortening and differential shortening of columns and walls. Therefore, to predict the horizontal deviation precisely, the time-dependent effects should be considered in the construction stage analysis.

4_CONSTRUCTION STAGE ANALYSIS

The proposed construction stage analysis is a series of nonlinear static analyses where new construction stages are applied to a stressed and deformed structure of the previous stage. The proposed analysis method consists of a deformation analysis of individual structural members to evaluate the creep and shrinkage deformation, and a frame analysis of the overall structure to consider the restraining effect of horizontal members. The algorithm of the construction stage analysis is to perform a series of structural analyses for every main construction stages such as concrete casting of a floor and installation of curtain walls, and to combine the results with time-dependent deformation to determine the overall

vertical and horizontal deformation. For every construction stage, two-step analysis is iterated in order to proceed to the next stage.

At the first step, shrinkage and creep deformation of individual structural members including columns and walls are calculated. The calculations are done for the time interval between construction stages. The column shortening due to shrinkage and creep are changed to strain load for the second step analysis. At the first construction stage, the calculation of shrinkage and creep is not performed because the elapsed time is equal to zero.

At second step, structural analysis on deformed structure is carried out to account for newly applied loads and strain loads which are calculated from the first step. Structural restraints of neighboring members on the shrinkage and creep shortening are considered in this step. The current location of each node including vertical and horizontal displacements is designated and stored for the next stage analysis. The construction sequence of a building is modelled by assigning birth date or extinction date to each element of the structural model for self-weight and to other additional loading stages. The overall algorithm for the staged analysis is shown in Figure 2. After each iteration of the staged analysis is performed (refer to the left side of Figure 2), the results are classified into UPTO and SUBTO components (refer to the middle part of Figure 2) and non-structural construction (refer to the right side of Figure 2).

The total movement of a single member at a specific level can be classified in relation to construction schedule by the following criteria. A movement up to slab installation (hereafter called UPTO) at a specific time refers to the movement amount which has already developed and accumulated up to the time when the building elements under consideration are installed from the start of structure construction. This amount vanishes if a building is constructed so that every element of the building conforms to its designed location at the time of construction. A movement subsequent to slab installation (hereafter called SUBTO) at a specific time refers to the movement amount which has developed and accumulated at target time subsequent to the time when the building elements under consideration are installed.

5_CASE STUDY

5.1. Structural layout

KLCC Tower No. 3 which is located in Kuala Lumpur, Malaysia is the 3rd tallest building in the city with a height of 267m (refer to Figure 3(a)). This building has 58 floors above ground and four basement levels. The gross area of the building is 84,000m^2. The first six floors above street level contain commercial space. Upper floors of the building contain office spaces. The structure is symmetrical to horizontal axis with a plan of 63×55 m. As shown

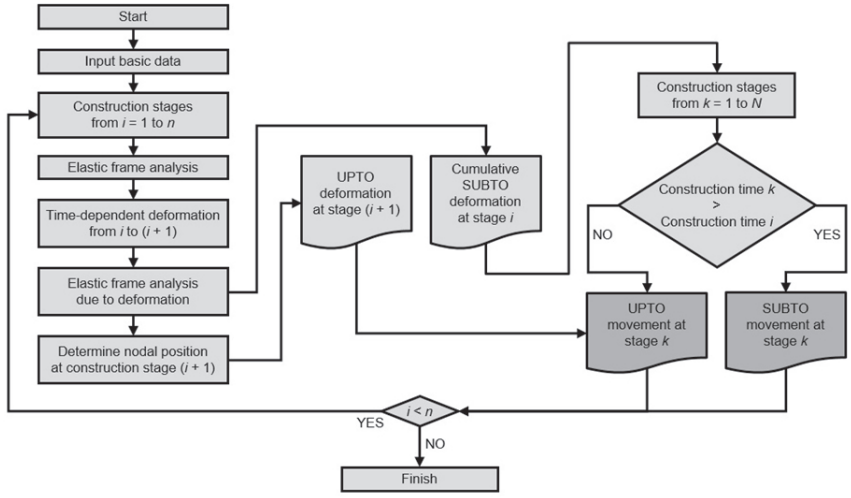


Fig. 2. Algorithm of the proposed construction stage analysis

in Figures 3(b) and 3(c), the shape of the floor plan is rectangular. Starting at the level 30, it changes from rectangle to triangle. The structural systems are composed of RC cores and columns. Central cores and transfer floors at levels 29~31 are acting as outrigger and are provided to resist lateral loads. Perimeter columns and flat slabs are designed to carry vertical loads.

5.2. Construction staged analysis

5.2.1 Input data

Based on the structural drawings, the three dimensional construction staged analysis model was created as shown in Figure 4. Properties of concrete used in vertical members are summarized in Table 1. Creep and shrinkage values are taken from laboratory test results. Three categories of loadings were considered in the model - dead load (DL), superimposed dead load (SDL) and live load which were applied to vertical and horizontal members. Reduction factor for live load was chosen to be 0.5, which is sufficient as compared with the minimum 0.4 (ASCE/SEI 7-10, 2010). Target time is set to 7 years after the completion of the construction as provided by the project's particular specification of construction. Creep and shrinkage components of axial shortening are influenced by the environmental condition such as relative humidity. Relative humidity of Kuala Lumpur is set to 80 %.

Loading sequence used in the analysis is based on the construction schedule as was planned by the construction team. The core walls are set up first followed by the construction of perimeter columns and the slab outside of core walls. The slab inside the core walls are intentionally assumed to be cast at the same time as the slab outside of core walls due to lack of information and to avoid complexity. The date of application of SDL is set equivalent to the installation sequence of the curtain walls in the construction schedule and the live load is assumed to be applied on 1,008 days after the start of construction, at which time construction works was assumed to be completed and the building was utilized. The construction live loads were neglected because it is applied temporarily and does not have significant time-dependent effects on the building.

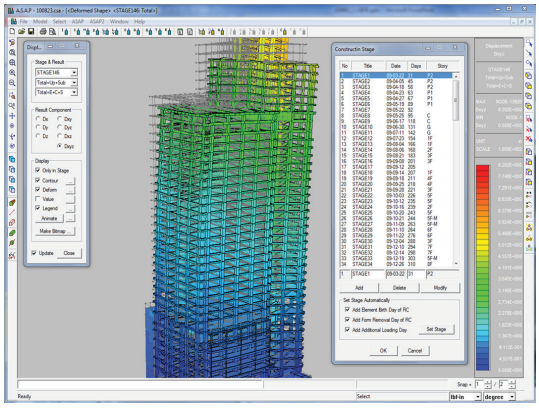
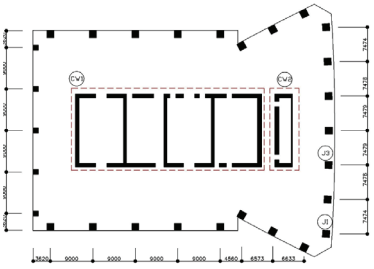


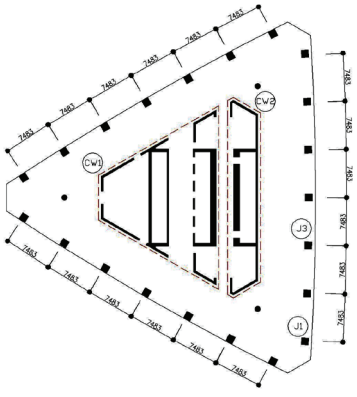
Fig. 4. Three dimensional construction stage analysis model of KLCC Tower No. 3



(a) Full view of KLCC Tower No. 3



(b) Floor plan of the lower part



(c) Floor plan of the higher part

Fig. 3. KLCC Tower No. 3

5.2.2 Time-dependent material properties

While elastic deformations are simply calculated from the applied load and modulus of elasticity, creep and shrinkage deformations are influenced by various factors such as member size and shape, reinforcement ratio, relative humidity, modulus of elasticity, duration of load application, and age of curing at the start of loading. Currently, several predicting models such as ACI 209, CEB-FIP, PCA, B3 and GL2000 are recommended. From these models, the PCA model, which can consider the restraint effect of steel reinforcement, are selected to predict the shrinkage and creep deformations.

Estimation of the concrete's modulus of elasticity is carried out by Eq. (3), which combines the equation from ACI 318 (2014) for calculating the modulus of elasticity from the compressive strength and that from ACI 209 for calculating the time-dependent strength of moist-cured concrete using Type I cement.

$$E_{ct} = 0.043 w_c^{1.5} \sqrt{\frac{t}{4.0 + 0.85t}} f_{cm28} \tag{3}$$

where ω_c is the unit weight of concrete and f_{am28} is the 28 days cylinder compressive strength of concrete. For high-strength concrete, a reduced value of the elastic modulus recommended by ACI 363 (2010) can be used instead of Eq. (3). The second moment of inertia of the cocnrete members were calculated based on the uncracked section and the transformed area considering the difference of stiffness between the concrete and the reinforcement.

Estimation of creep strain is carried out by Eq. (4), where various factors including loading time, concrete age, size effect, and relative humidity are considered (Fintel et al., 1986).

$$\varepsilon_{cr} = \varepsilon_{cr\infty} CR_t CR_{la} CR_{us} CR_{RH} CR_{sr} \tag{4}$$

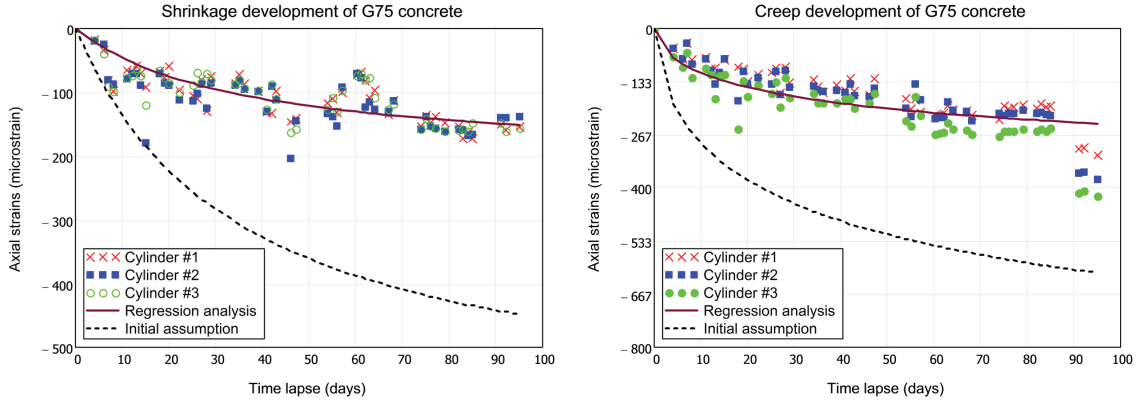
where $\varepsilon_{cr\infty}$ is the specific creep, CR_t is a factor to allow for progress of creep with time, CR_{la} is a factor for the age of concrete at loading, CR_{us} is a member size factor, CR_{RH} is a relative humidity factor and CR_{sr} is a factor for the reinforcement.

Estimation of shrinkage is carried out by Eq. (5), where various factors including concrete age, size effect, and relative humidity are considered (Fintel et al., 1986).

$$\varepsilon_{cr} = \varepsilon_{shu} SH_t SH_{us} SH_{RH} SH_{sr} \tag{5}$$

where ε_{shu} is the ultimate shrinkage, SH_t is a factor to allow for progress of shrinkage with time, SH_{us} is a member size factor, SH_{RH} is a relative humidity factor and SH_{sr} is a factor for the reinforcement.

To enhance the accuracy of the prediction values, the material tests for creep and shrinkage were conducted during three months in climate-controlled chamber where the temperature and relative humidity can be maintained at levels specified in



(a) Shrinkage (b) Creep

Fig. 5. Creep and shrinkage test results for G75 concrete

ACI 209R-92. 150 × 300 mm test cylinders were cast at the construction site from concrete being used in the vertical members. On the day after casting, these were delivered to the laboratory with the moisture curing cover. The specimens were moist-cured for 28 days, followed by the tests of compressive strength and modulus of elasticity. Three creep specimens were loaded up to 30% of the ultimate cylinder strength and stored in the constant temperature and humidity environments. Concrete strain gauges were attached on the side surface of the cylinders in the middle and the obtained data were averaged using nonlinear regression analysis. Manual hydraulic jack with appropriate capacity was used to apply the constant load under the spring-type creep test machine. The applied load in the creep test was monitored and the relaxation in the load was recovered to the initial value at the time of data readings. Shrinkage test specimens were kept in the same environment as the creep test specimens without any loading.

Data readings from the strain gauges were recorded daily for three months. As shown in Figure 5, values of specific creep and ultimate shrinkage derived from nonlinear regression analysis on the test results are significantly smaller than the theoretically assumed ones. Laboratory test results used in the construction staged analysis are presented in Table 1.

5.3. Analysis results

5.3.1 Lateral movement induced by differential shortenings

Columns J1, J3, and core walls CW1, CW2 were selected to analyze the horizontal deviation of the building. Their cross sections and reinforcement ratios changed along the building height as shown in Table 2.

The predicted results of lateral movement are presented in Figures 6 and 7 for columns and walls, respectively. The total lateral movements are divided into elastic, shrinkage, and creep components. The maximum lateral movement of columns J1 and J3 at the top floor are predicted to 93.2 mm and 93.0 mm, which consist of 47 % elastic, 17 % shrinkage, and 36 % creep. Therefore, the total lateral movement including the shrinkage and creep effects increases to 2.13 times the elastic movement at the top floor.

The maximum lateral movement of walls is larger than that of column due to the shrinkage component. It is considered that wall member, which has relatively small volume-surface ratio, shows the larger shrinkage value. The maximum lateral movements of CW1 and CW2 at the top floor are predicted to be 117.6 mm and 123.4 mm, which consist of 41 % elastic, 24 % shrinkage, and 34 % creep. The total lateral movement of the core walls including

Table 1. Properties of concrete used in vertical members

Compressive strength (MPa)			Elastic modulus (MPa)	Specific creep (mm/mm/MPa)	Ultimate shrinkage (mm/mm)	Poured levels
$f_{ck\text{-}cube}$	f_{cm28}	$f_{cm28.test}$				
75	68	77	43,064	23E−06	253E−06	B4 ~ L17
65	61	71	40,995	17E−06	1,216E−06	L18 ~ L32
60	58	–	40,076	–	–	L33 ~ L44
55	53	60	38,495	29E−06	276E−06	L45 ~ L59

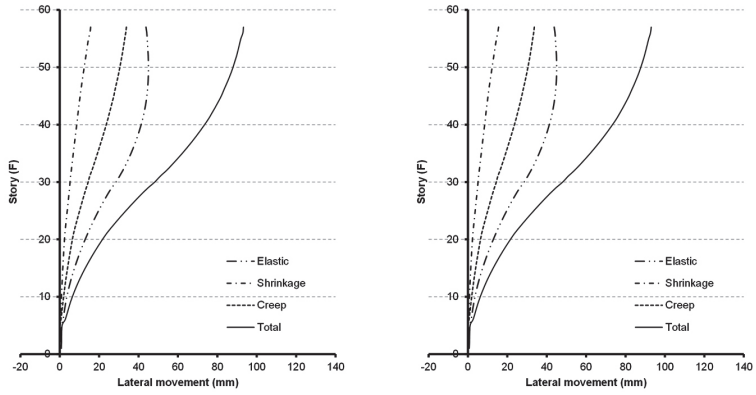
Note: Test values of the compressive strength of G60 concrete, and those of the elastic modulus of G65, G60 and G55 concretes were not available.

Table 2. Properties of analyzed columns and walls

Level	Column size, m and reinforcement ratio, %				Wall thickness, m and reinforcement ratio, %			
	J1		J3		CW1		CW2	
B4−B1	1.55×2.0	1.04	1.45×2.0	1.05	1.0	0.67	0.7	0.98
L1~L8	Ø1.8	1.01	Ø1.8	1.01	1.3	1.97	0.55	0.80
L9~L20	1.55×1.55	1.07	1.55×1.55	1.07	0.77	0.58	0.67	0.65
L21~L29	1.45×1.45	1.07	1.45×1.45	1.07	0.7	0.63	0.67	0.65
L30~L56	0.85×0.85	1.07	0.85×0.85	1.09	0.48	1.04	0.67	0.70

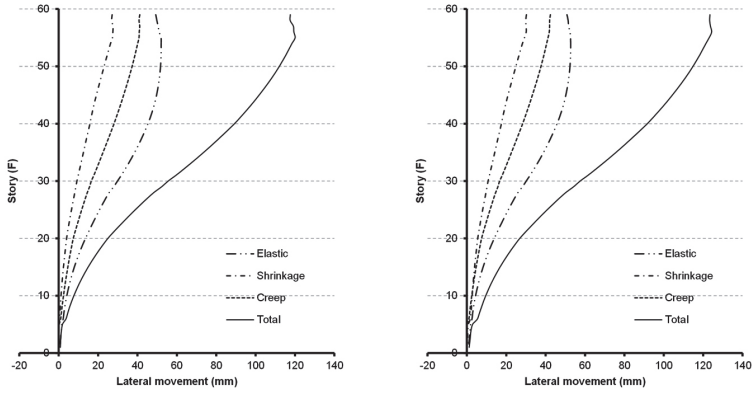
the time-dependent effects increases to 2.4 times the elastic movement. The greater amount of the maximum lateral movement and the ratio of total to elastic movements for core walls than columns are judged to have originated from the fact that the walls are more prone to the creep and shrinkage effect compared with columns due to higher ratio of surface area to volume of walls.

ed from the level 30 resulted in increasing the rate of deviation from verticality below the level 30. The SUBTO values increases to some extent level where it decreases again. The maximum SUBTO lateral movement of J1 and CW2 occurs at Level 39 and 41. It is because loads from the upper floors, which contribute to SUBTO value, decrease with increasing stories.



(a) Column J1 (b) Column J3

Fig. 6. Lateral movements of columns



(a) Core wall CW1 (b) Core wall CW2

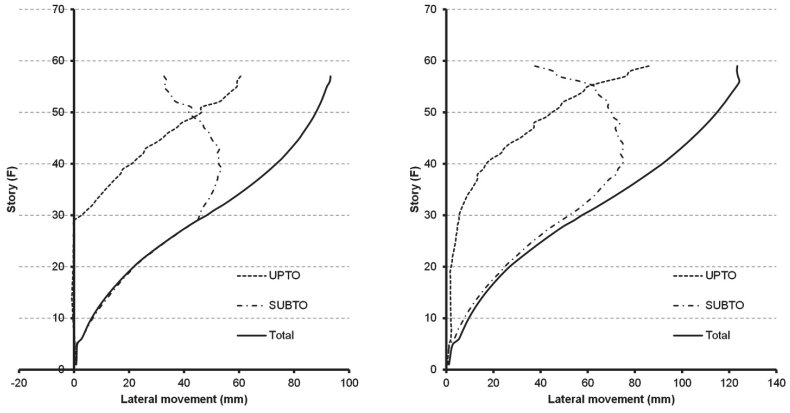
Fig. 7. Lateral movements of core walls

5.3.2 UPTO and SUBTO lateral movement

Lateral movements of column J1 and core wall CW2 are presented in Figure 8. The UPTO movement of column and core wall abruptly increase from the level 30, where framing plan is changed from rectangle to triangle. The eccentricity of mass start-

5.3.3 Time history of lateral movement

Figure 9 shows the variation of the predicted lateral movement over time. The total maximum deformation values for J1 and CW2 along the height of the building are divided into elastic, shrinkage, and creep according to the cause of movement. The



(a) Column J1 (b) Core wall CW2

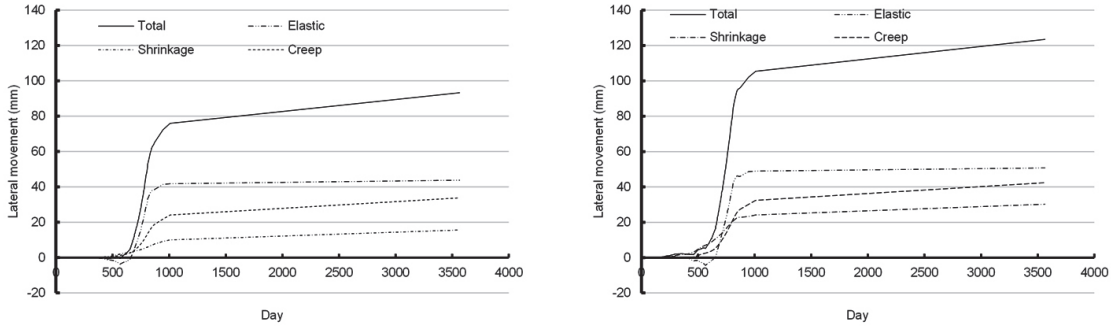
Fig. 8. UPTO and SUBTO components of lateral movement

concrete of the structural members at the top floor was poured at 872 days after the construction of the lowest vertical members. The whole construction work was finished at 1,007 days. The lateral movement abruptly increases after the slab at Level 30 was casted. It is considered that the mass eccentricity, which starts at the Level 30, affects the UPTO values at the top floor. After the construction was finished, the lateral movement continuously developed due to the effect of shrinkage and creep. The percentage of the lateral movement that was developed after the completion of construction for wall CW2 and column J1 was 14.6% and 18.3%, respectively. Although a significant part of the lateral movements occur during construction, horizontal deviation continuously develops after its completion. The significance of the part of movement occurring before and after construction greatly depends on the time-dependent properties of material as well as the distribution and stiffness of the structural elements, geometry of the building and the sequence of construction.

6_VERIFICATION

6.1. Field survey by three dimensional laser scanning

To monitor building movement during construction, various methods such as field measurement by strain sensors (Kijewski-Correa et al., 2013; Su et al., 2013; and Russell et al., 1989), survey using total station and GPS were introduced and used. In addition to these methods, three dimensional laser scanning is also used for the survey of architectural buildings. The beam



(a) Column J1 (b) Core wall CW2

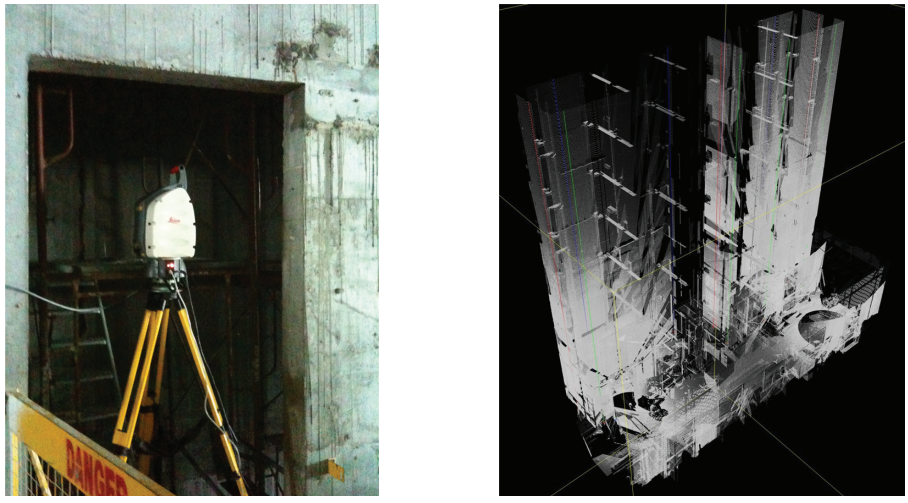
Fig. 9. Time history of lateral movement

from the laser scanner accurately scans the point or surface target and measures the distance by calculating the round trip time of laser or pulse. It can create a point cloud of geometric shape on the surface of subjects. The movements of the entire building can be monitored by three dimensional laser scanning with short working time. This method was mostly used for the survey of low or mid- rise buildings due to the limit of the scanning range. A long range laser scanner, HDS8800, which was recently developed and has a scanning range of over 1,000 m, was used in this study combined with a middle range scanner, C10 which has a shorter scanning range of 300m than HDS8800 but has a higher speed of scanning of 50,000 pts/sec and an increased tolerance of 6mm. HDS8800 was used to survey the higher part of the building exterior, while C10 was used to survey the lower part of the building exterior, foundation of the building, and the inside the lift cores.

Scanning the lift core was performed inside CW2 before the installation of lifts in the lift cores to evaluate the verticality of CW2, where the maximum lateral movement is predicted. The lift core of CW2 was scanned both at the entrance of the lift as shown in Figure 10(a) and at the center of the lift core using a temporary lift. After the scanning was carried out at every floor, the separate sets of obtained data were integrated to make a complete scanned results called "point clouds" as shown in Figure 10(b). Once the point clouds are available, they can be further processed to derive a set of useful data. For comparing with the predicted lateral movement of CW2, nine locations were selected in the plan of the scanned data at every floor and their lateral deviation values were averaged to produce the amount of the lift core's lateral movement at the level. Each point in the graph of Figure 11 represents the result of this process.

6.2. Comparison with field survey

To synchronize the time of survey with that of the analysis results, the SUBTO component of the predicted lateral movement of CW2 was further divided into another UPTO and SUBTO components based on the time of lift installation according to the software's algorithm shown in Figure 2. The surveyed lateral movements increased up to 73mm at the level 38 and steadily decrease again. When compared with predicted movements, distribution of surveyed movements shows similar pattern as shown in Figure 11. The mean of the differences between surveyed and predicted movements is 6mm, which is not bigger than the tolerance of the laser scanner. Considering the tolerances of construction and surveying instruments, the surveyed results using three dimensional laser scanning techniques showed good agreements with the predicted values.



(a) Scanning the interior of lift core (b) Point clouds of scanned results

Fig. 10. Three dimensional laser scanning of lift core

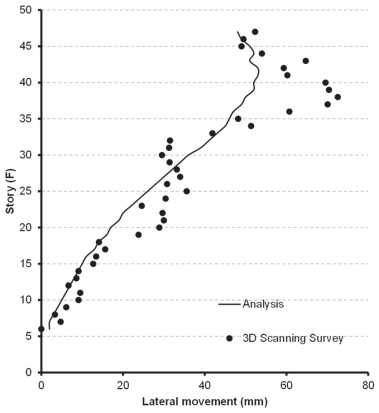


Fig. 11. Comparison of predicted and surveyed lateral movements of CW2

7_CONCLUSION

This research described a theoretical study on the behavior of the horizontal deviation for tall buildings that is induced by vertical shortenings considering time-dependent properties of the concrete. The developed analysis method was used to predict the horizontal deviation from verticality for a 58 story reinforced concrete building. The aging effects of concrete on the tall building were analyzed and analysis results were verified by field survey. Based on these studies, the following conclusions were made.

1) Differential shortenings induced by the eccentricities of building's mass or stiffness may cause a significant amount of lateral movement, and the time-dependent effects of concrete accelerate the movement.

2) The total movement of the high-rise buildings can be divided into elastic, shrinkage, and creep components. For the investigated case study building, the total lateral movement including the shrinkage and creep effect increased up to 2 times the elastic values. Therefore the lateral movement caused by aging effects including shrinkage and creep of concrete that occur during the construction stage of high-rise buildings should be considered and allowed for in design.

3) The percentage of lateral movement that was developed after the completion of the construction works for the investigated case study building was in the range of 14% to 18%, while bigger part occurred during the construction stage. Therefore, deformation occurring during the construction stage shall not be underestimated or ignored.

4) Three dimensional laser scanning field survey was carried out to verify the predicted analysis results and satisfactory agreement was obtained. These results show that the lateral movement induced by differential shortening can be calculated with a reasonable degree of accuracy by the developed construction stage analysis method. It was also concluded that three dimensional laser scanning can be efficiently used for the monitoring of the vertical and horizontal movements of tall buildings.

REFERENCES

1. ACI Committee 209, (2008). 209R-92: Prediction of Creep, Shrinkage, and Temperature Effects in Concrete Structures. American Concrete Institute, Farmington Hills, MI, USA.
2. ACI Committee 318, (2014). 318-14: Building Code Requirements for Structural Concrete and Commentary. American Concrete Institute, Farmington Hills, MI, USA.
3. ACI Committee 363, (2010). 363R-10: Report on High-Strength Concrete. American Concrete Institute, Farmington Hills, MI, USA.
4. ASCE/SEI 7-10, (2010). Minimum Design Loads for Buildings and Other Structures. ASCE Standard. American Society of Civil Engineers, Reston, Virginia, USA.
5. Bazant, Z. P. and Murphy, W. P., (1995). Creep and Shrinkage Prediction Model for Analysis and Design of Concrete Structures – Model B3. Materials and structures 28(6): pp. 357-365.
6. Chajes, A., (1990). Structural Analysis. Prentice Hall, New Jersey, USA.
7. Chiorino, M. A., Casalegno, C., Fea C., and Sassone M., (2011). Numerical Analysis of Creep and Shrinkage Effects

in High-Rise Concrete or Steel-Concrete Buildings. Pro - ceedings fib Symposium 2011, Prague, Czech: pp. 835-838.

8. Fintel, M., Ghosh, S. K., and Iyengar, H., (1986). Column Shortening in Tall Structure – Prediction and Compensation (EB108.01D). Portland Cement Association, Washington, D.C, USA.
9. Gardner, N. J., (2004). Comparison of Prediction Provisions for Drying Shrinkage and Creep of Normal-Strength Concretes. Canadian Journal of Civil Engineering 31(5): pp. 767-775.
10. Grabow, M. J., (2004). Construction Stage Analysis of Cable-Stayed Bridges. Diplom Ingenieur, Technische Universität Hamburg-Harburg.
11. Kijewski-Correa, T., Kwon, D. K., Kareem, A., Bentz, A., Guo, Y., and Bobby, S., (2013). SmarSync: An Integrated Real-Time Structural Health Monitoring and Structural Identification System for Tall Buildings, Journal of Structural Engineering October: pp. 1675-1687.
12. Kim, H. S., (2013). Effects of Horizontal Members on Column Shortening of Reinforced Concrete Building Structures, The Structural Design of Tall and Special Buildings 22: pp. 440-453
13. Kurc, O., and Lulec, A., (2013). A Comparative Study on Different Analysis Approaches for Estimating the Axial Loads on Columns and Structural Walls at Tall Building, The Structural Design of Tall and Special Buildings 22: pp. 485-499.
14. Lavery, M., Kelly, T., and Hira, A., (2015). Interconnectivity of Design and Construction for Complex Towers in Relation to Movement Issues, Proceedings of the CTBUH 2015 International Conference, New York: pp. 517-523.
15. Lu, J., Wu, J., Luo, X., and Zhang, Q., (2013). Time-dependent Analysis of Steel-Reinforced Concrete Structures, The Structural Design of Tall and Special Buildings 22: pp. 1186-1198.
16. Maru, S., Asfaw M. and Nagpal, A. K., (2001). Consistent Procedure for Creep and Shrinkage Effects in RC Frames. Journal of Structural Engineering 127(7): pp. 726-732.
17. Russell, H. G. and Larson, S. C., (1989). Thirteen Years of Deformations in Water Tower Place. ACI Structural Journal 86(S21): pp. 182-191.
18. Su, J., Xia, Y., Chen, L., Zhao, X., Zhang, Q. L., Xu, Y. L., and Ding J. M., (2013). Long Term Structural Performance Monitoring System for Shanghai Tower, Journal of Civil Structural Health Monitoring 3: pp. 49-61

A software tool for the analysis of time-dependent effects in high-rise buildings: development, validation and application to a real case-study

Sungho Lee
Architectural Research Team, Principal Researcher
sungho.lee@daewooenc.com

본 논문은 2016년 CTBUH Journal Issue 3, pp. 40–45에 게재되었던 논문을 재게재한 것입니다.

Abstract

The expansion of the use of concrete in high-rise buildings has made these structures sensitive to the effects of delayed deformations (creep and shrinkage) in the construction stage and along their service life. The problem becomes particularly relevant in supertall buildings. Besides delayed absolute shortening of the building structure, differences in stress conditions and geometrical and material characteristics of vertical elements – which may include steel or steel /concrete elements in hybrid structures – can induce delayed differential shortening of adjacent members. The time-dependent behavior of the structure is also influenced by the sequential construction process, being characterized either by successive increments of loads on vertical supports, and by multiple changes in the structural system. In cases of lack of symmetries in the building structure or in the construction sequences, lateral displacements and consequent deviations from verticality of the entire building can develop as well, affecting the load distribution in vertical elements. If not properly governed and accounted for, all these phenomena may create serviceability and safety concerns by giving rise to various adverse structural effects as e.g. impaired levelness of floors, redistribution of internal actions, related cracking in horizontal structures, and load redistribution among vertical supports. Serviceability of non-structural components may be affected as well. The authors present the results of the development of a software tool specifically conceived by Daewoo Engineering and Construction Company for the prediction of time-dependent behavior of high-rise buildings in both the construction stage and the long term. The specific features of the software are illustrated, and the results of a review and validation work carried out in collaboration with the Politecnico di Torino are presented. Finally, the application to a real case study of a high-rise building currently under construction in Malaysia is discussed.

Keywords : column shortening, construction stage analysis, high rise building

1_INTRODUCTION

In the last decades the use of reinforced concrete as the main construction material for high-rise buildings has significantly increased (Fig. 1). As a consequence, these structures have become sensitive to the effects of time-dependent concrete properties such as creep and shrinkage (CCIP-058 and fib, 2014). The problem becomes particularly relevant in super-tall and record breaking buildings (Baker & al., 2007).

While the construction of the building proceeds, vertical supporting members as columns and cores are subjected to successive load and axial strain increments due to the construction of the overlying floors. In concrete elements, these initial strains increase due to creep and shrinkage, generating along the time and in the long term both overall shortening of the building and shortening differences among columns, between cores and columns,

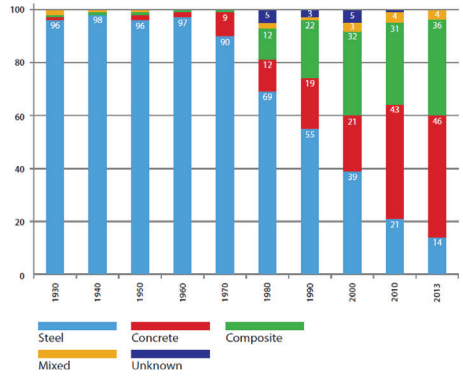


Fig. 1. World's tallest 100 buildings by structural material [Safarik et al., 2014]

or, in the case of hybrid structures, between concrete cores and steel or concrete-and-steel composite columns. The differences in the initial and time-dependent strains among concrete vertical members are normally due to differences in the stress levels and/or in the creep and shrinkage properties, as a consequence for example of members' volume-to-surface ratio (effective thickness) and/or longitudinal reinforcement ratio. Such differences in the strains are intrinsic in hybrid concrete-and-steel structures due to the different initial deformability of the two materials and the absence of creep and shrinkage in steel elements. The problem is further complicated by the continuous changes of the structural configuration inherent to the construction sequences.

Redistributions of stresses and internal actions, as vertical loads in the supporting members and shear stresses and bending moments in horizontal members, are normally associated to all these effects in the case of rigid connections between floor structures and vertical elements, and especially in the case of a presence of stiff horizontal bracing or transfer structures. In cases of lack of symmetries in the building structure or in the construction sequences, lateral displacements and consequent deviations from verticality of the entire building can develop as well, affecting the load distribution in vertical elements.

If all these phenomena are not adequately understood and analysed in the design and construction phases, several serviceability concerns may arise (Carreira and Poulos, 2007; CCIP-058 and fib, 2014; Chiorino et al., 2011; Fintel et al., 1986; Lagos et al., 2012) affecting structural members as well as non-structural components, such as sloping of floors, cracking of horizontal structures, floor slabs and interior partitions, buckling of elevator guides and of piping, misaligned elevator stops relative to floors, as well as damage to curtain walls and column cladding. In case of increments of the loads in vertical elements, their influence on the ultimate strength cannot be neglected; at this respect, special attention must be paid in the case of hybrid structures (being normally characterized by significant shifts of axial loads from concrete to steel vertical elements), especially when buckling of slender steel elements must be feared.

In concrete structures up to 50-100 m the effects of the delayed deformations are often disregarded without serious consequences. In higher structures, as well as in hybrid structures also in case of lower heights, ignoring the effects of creep and shrinkage can lead to undesirable service conditions and in some cases also to concerns for the structural safety of the building.

Axial shortening of a tall building can be predicted relatively easily during the preliminary design stage as the sum of elastic, creep and shrinkage deformations in the single vertical elements, taking into account the construction sequence (Fintel et al., 1986). This prediction method is usually referred to as "one-column shortening analysis". The most significant limit of this approach is the fact that the restraining effects against differential shortening of the beams or slabs connected to the column or wall are not considered, or are considered in an approximate way. The method has been widely used for decades, but over recent years there has been a move towards sequential construction stage analyses and time-history analyses of 3D models of the entire building structures.

A construction-stage and time-history analysis using a 3D FE model that incorporates the time-dependent constitutive relations for concrete gives more accurate and comprehensive results than a one-column shortening analysis for building movements. This more advanced and refined analysis considers the effects of sequences of gravity loading and consecutive changes in the structural system as construction progresses, and concurrently evaluates the effects of the various time-dependent properties of

the concrete elements of the structure on the building structural response. Movements of the building are calculated along the time in the construction stage and at long term, as well as redistributions of internal actions in vertical and horizontal members.

To this second kind of analysis tools belongs the software presented in the following, specifically developed by Daewoo Engineering and Construction Company for the prediction of the time-dependent behaviour of high-rise buildings along the construction stage and at long term. The main specific features of the software are illustrated, and the results of a review and validation work carried out in collaboration with the Politecnico di Torino are presented. Finally, the application to a real case-study relative to a high-rise building is discussed.

2_TIME-DEPENDENT CONCRET PROPERTIES

Although there are several analysis software which can simulate sequential construction, it must be considered that in general their main focus was originally set mostly on the construction stage analysis of bridges. As a result, current commercial software may normally have some functional limitations and incompatibilities to solve problems typical of high-rise building and their complex construction stage sequences, consisting of a very large number of multifaceted steps smeared along an extended time, and to model intrinsic aspects of these types of structures like axial shortening,

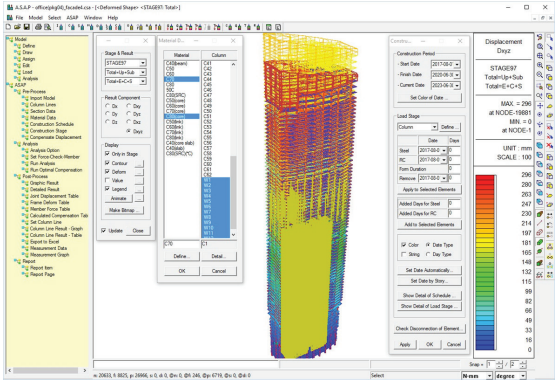


Fig. 2. User interface of ASAP for post-processing of results

deviation from verticality and redistribution of internal actions.

The Advanced Stage Analysis Program (ASAP) is a 3D FEA software specifically conceived for the analysis of the time-dependent behaviour of high-rise buildings during the construction stages and along the service-life (Fig. 2). The software has been developed by Daewoo E&C's structural engineers associated with software programmers since 2007 (Ha et al., 2011).

The program allows predicting building movements in the vertical and horizontal directions at any stage of construction as well as at any desired target time. Redistribution of internal actions and stresses, consequent to the delayed concrete strains and the related differential shortenings and deviations from verticality, and to the progressive changes in the structural system, can also be evaluated at any time. In particular the program allows calculating the variations along the time of internal actions and stresses in rigidly connected floor structures and in stiff horizontal structural members such as transfer beams, outriggers, and belt walls/trusses, as well as the concurrent variations of loads in vertical elements.

Once the loading date and duration of columns forms and slabs supports are defined, the software automatically generates the construction stages. The user can also create specific construction sequences for his own needs.

It is possible to import FE models from SAP2000, ETABS and MIDAS/GEN. Beam and plane FE elements (such as shell, plate, plane stress etc.) are implemented in the software. For the time-dependent behavior of concrete, ACI 209R-92 (ACI, 2008), Eurocode 2 (EN, 2005), B3 (ACI, 2008), GL2000 (ACI, 2008) and PCA (Portland Cement Association) (Fintel et al., 1986) creep and shrinkage prediction models can be used in the analysis. Interaction between foundation and superstructure can also be simulated by iteration during the staged analysis.

The software's algorithm facilitates programming and control of compensation procedures by classifying components of movement in vertical direction and allowing the insertion of diverse compensation (preset) options, and by identifying progressive horizontal movements and allowing the adoption of the related suitable corrections. The effects along the time of all these geometrical counteractions is taken into account in the analysis.

The software structure allows as well the incorporation of results of anticipated or concomitant tests on the time-dependent properties of the concrete used in the construction, permitting the updating of the implemented creep and shrinkage prediction models, and the incorporation of data on the behaviour along the time of the structure in terms of strains and stresses, deformations, movements and forces, resulting from on-site survey and monitoring campaigns during the construction stage and along the service life, permitting the verification of the corresponding outputs of the program and appropriate program updating procedures.

3_SOFTWARE VALIDATION

A review and validation process of the Advanced Stage Analysis Program (ASAP) has been carried out in collaboration between Daewoo E&C and the Politecnico di Torino.

The final goal of this process is to guarantee the appropriateness of ASAP in the evaluation of all structural effects of the time-dependent behaviour of concrete in concrete and concrete-and-steel high-rise buildings in the construction stage and along their service-life, in accordance with the most advanced formats defined within international guidance documents (CCIP-058 and fib, 2014;ACI, 2011; fib, 2013; Chiorino and Carreira, 2012; Chiorino and Casalegno, 2012) and scientific literature (Ghali et al., 2002; Chiorino and Gardner, 2007; Jirásek and Bažant, 2002).

More specifically, the review process is intended to ensure that the computational algorithm of ASAP is able to:

- Evaluate in accordance with these formats the structural effects of the delayed deformations of concrete, either in terms of development of deformations and movements, and of changes of distributions of internal stresses and actions in all vertical and horizontal structural elements;
- Consider the intrinsic sequential character of high-rise buildings in their construction phase, and consequently address the effects not only of the progressive sequential application of actions, in terms either of applied loads and, of imposed deformations, but also the effects of the progressive sequential changes in the structural system as the construction proceeds.

In what concerns the initial and time-dependent properties of concrete , the review concerns the ability of the ASAP program to correctly incorporate the different prediction models deriving from the most advanced scientific literature and/or technical guidance documents at the international level. In particular, the program must guarantee to be able to evaluate, in accordance with these models, the specific shrinkage and creep properties of each single structural element as influenced by inherent internal and external physical and geometrical parameters, time of casting and age. For the moment being, the correct incorporation of the Eurocode 2 (EN, 2005), B3 (ACI, 2008), GL2000 (ACI, 2008) prediction models has been checked.

As for the evaluation of the structural effects induced by the delayed deformations of concrete, with particular regard to creep, the review is intended to control that the outputs of the ASAP shall be coherent with the results obtained according to the formats of all current advanced creep prediction models, which are formulated within the frame of the theory of aging linear of viscoelasticity, with due account for the aging properties of concrete and heritage character of its behaviour along the time. For complex sequential structures, histories of application of external actions and progressive changes of structural systems, this implies the progressive solution of linear integral equations, or the adoption of equivalent rate-type approaches.

On the basis of these premises a few actions have been undertaken to check the validity of ASAP with respect to some reference properly selected case studies.

The two terms of reference being confronted in each case study are the numerical values obtained, on the one hand, from ASAP and, on the other hand, from the integral-type general computational approach for the analysis of structural effects of time-dependent behaviour of concrete developed at the Politecnico di Torino (Casalegno et al., 2010; Chiorino et al., 2011; Chiorino and Casalegno, 2012; Sassone et al., 2007a and 2007b; Sassone and Casalegno, 2012). This program ensues from the coupling

of the finite elements method with the integral-type formulation of aging linear viscoelasticity and the numerical solution of the inherent hereditary integral equations. The program allows taking into account non-homogeneities due to the presence of materials with different elastic and viscoelastic characteristics. Successive changes in the structural system can be considered as well, due to changes in the restraint conditions or to the introduction or subtraction of structural elements. Only beam and truss elements are implemented in the program and the analysis is limited to 2D models.

In particular, the following simple scholastic case studies – representing (1) extreme one time-step type problems, and (2) a scholastic example of a staged construction of a multi-storey structure - have been analysed in order to check the validity of the ASAP:

a) an unloaded concrete column, in order to check the correct implementation in the software of the shrinkage prediction models;
b) a concrete column, in absence of shrinkage, subjected to a constant unit axial stress (a creep type problem), in order to check the correct implementation of the creep prediction models;
c) a concrete column, in absence of shrinkage, subjected to a constant imposed axial deformation, in order to check the accuracy of the solution of the software in terms of the stress response to imposed deformations (a relaxation type problem);
d) a concrete column, in absence of shrinkage, in which a rigid restraint is introduced at mid height at time t1 after the application of an axial force at the top of the column at time t0 (a problem of creep induced redistribution of internal stresses and actions as a consequence of a change in the structural system due to the introduction of a delayed rigid restraint after the application of constant external loads) (Fig. 3);
e) a frame structure with concrete core and steel columns (the horizontal steel bracing element is considered as a rigid body) analysed to check the solution of the software for a case of a non-homogeneous hybrid structure in which the stress migrates in time from the viscoelastic part of the structure to the elastic one; for this case study also the evaluation of the effects of shrinkage and of the interaction between creep and shrinkage has been checked, taking into account, in addition to creep, the shrinkage deformations of the central core (Fig. 4);

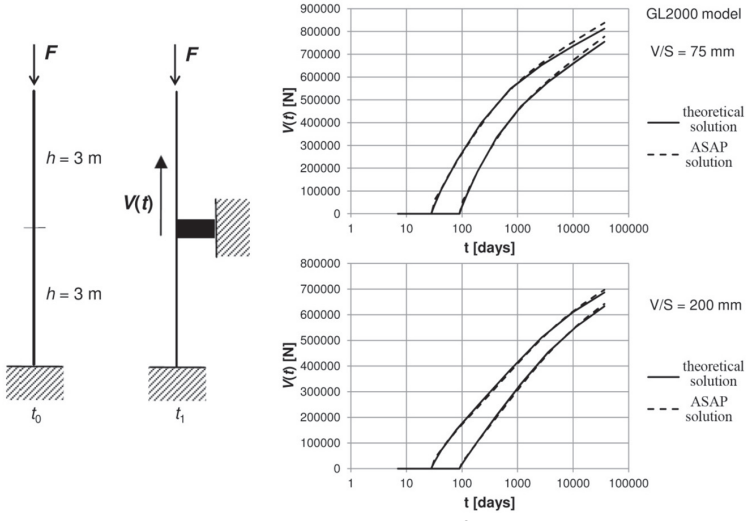


Fig. 3. ASAP software validation: case study of a column loaded at time t0 = 7 days subjected to the application of an additional delayed restraint at mid height at time t1 = 28 or t1 = 90 days

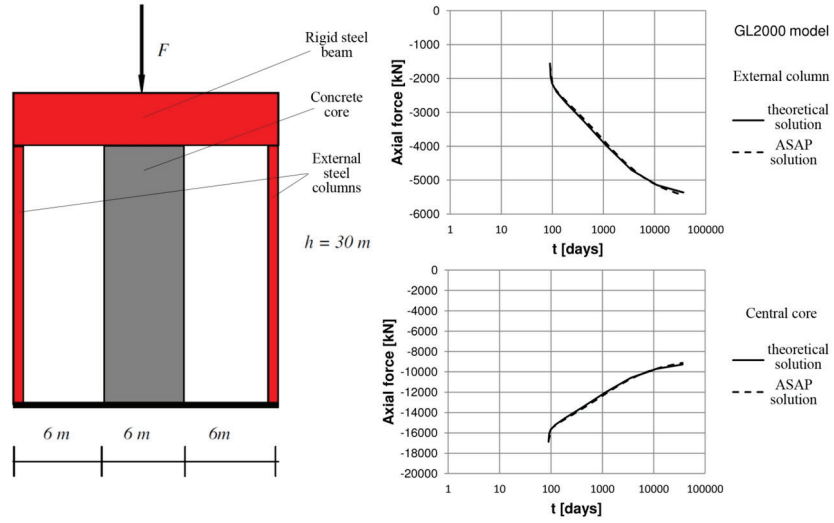
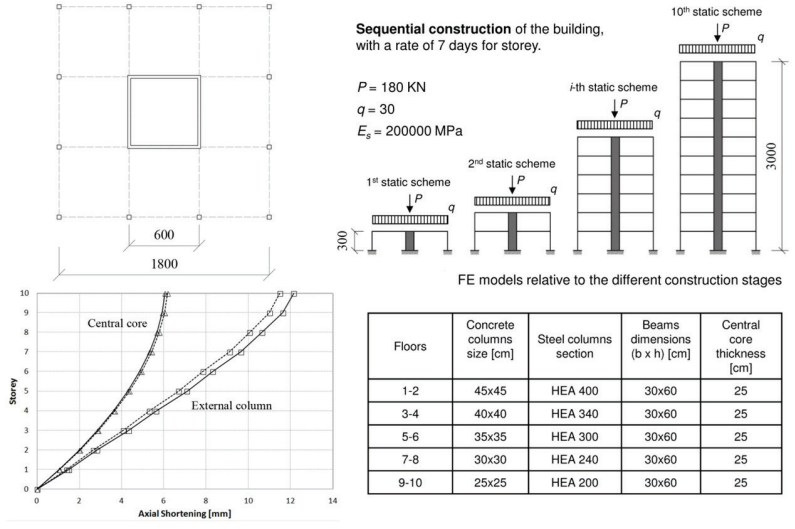


Fig. 4. ASAP software validation: case study relative to a non–homogeneous hybrid structure with concrete core and steel columns loaded at time t0 = 90 days (the horizontal bracing element is considered as a rigid body)

f) a simple demonstrative case of multi-storey building realized through a sequential construction procedure; two options have been considered, that is (1) the whole structure being made of reinforced concrete and (2) the external columns being made of steel; horizontal floor structures are in concrete; shrinkage deformations have not been taken into account in this case study (Fig. 5).

The analyses have been carried out for different sets of influencing parameters (loading age, volume to surface ratio, etc.). Cases a) and b) do not require the solution of any hereditary problem, but the simple numerical computation of shrinkage and concrete strains and consequent deformations according to the implemented shrinkage and creep models. The results given by ASAP are correct for all the case studies considered. Small differences be-



Floors	Concrete columns size [cm]	Steel columns section	Beams dimensions (b x h) [cm]	Central core thickness [cm]
1-2	45x45	HEA 400	30x60	25
3-4	40x40	HEA 340	30x60	25
5-6	35x35	HEA 300	30x60	25
7-8	30x30	HEA 240	30x60	25
9-10	25x25	HEA 200	30x60	25

Fig. 5. ASAP software validation: case study relative to a multi–storey building with concrete core and concrete or steel columns (sequential construction)

tween the results of the ASAP and the numerical solutions of the inherent hereditary integral equations are obtained only for the case study f) relative to the multi-storey building (Fig. 5). For the moment being, only GL 2000 (ACI, 2008) prediction model was considered in all these checks; for other prediction models checks were limited to the correct implementation of the models, by analysing only the first two simple case studies.

4_APPLICATION TO A REAL CASE STUDY

After the thorough review and validation of ASAP code as a result of previous steps, the code has been applied to the case of a real high-rise building represented by the "Public Bank", currently under construction in Kuala Lumpur, Malaysia (Fig. 6).

The tower block is 179 m high (42 storeys with 6 levels of basement). The structure is made of reinforced concrete mega-columns, in combination with post-tensioned beams for horizontal floor structures. The tower block comprises two zones, namely, the low rise office floors from level 6 to level 22 and the high rise office floors from level 23 to level 38. The high rise office floors have a larger usable office space due to the low rise lift core stopping at level 22.

In brief, the structural framing consists of the following:

- post-tensioned beams with span lengths of 14 m to 16 m; the beam depths for main and secondary beams are 750 mm and 650 mm, respectively;
- reinforced concrete beams at shorter span areas with beam depths of 600 mm;
- reinforced concrete beams are also provided at level 5, level 22, level 39 and level 40 due to the heavier loadings on these floors; the beam depths adopted are 1.0 m, 1.1 m and 1.5 m for level 5, level 22, level 39 and level 40 respectively;
- the biggest columns are located along grid line 4 and 6 (Fig. 6), with sizes varying from 2.4 m x 2.4 m to 2.6 m x 2.4 m; these columns reduce in size to 1.7 m square from level 22 to 31 and 1.35 m square from level 31 upwards;
- the size of four corner columns varies from 1.8 m x 1.8 m to 1.4 m x 1.8 m and subsequently reduce to 1.1 m x 1.8 m and 1.1 m x 1.4 m from level 6 upwards;
- core wall thickness varies from 450 mm to 250 mm depending on structural requirements.

A FE model of the building has been realized using ASAP. Every significant phase of the construction has been modelled, for a



Fig. 6. The "Public Bank" in Kuala Lumpur, Malaysia: rendering and typical layout plan

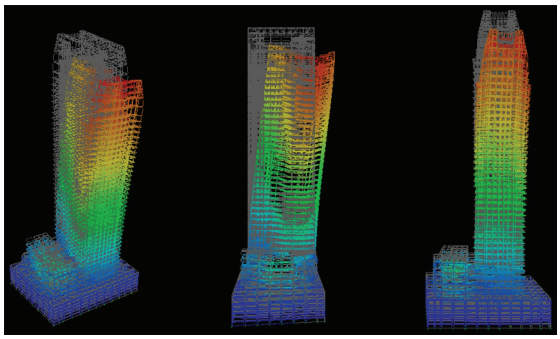


Fig. 7. Deformed shape at 100 years

total of 86 construction stages. A construction-stage and time-history analysis has been carried out for a final target time of 100 years. In order to evaluate the influence of time-dependent deformations of concrete on the long-term behaviour of the building, no compensation of displacements is applied in the analysis.

The deformed shape obtained at the final target time of 100 years (Fig. 7) shows, besides the shortening of columns and walls, a significant deviation from verticality. The results in terms of diagrams representing the total shortening – up to the completion of the floor (UPTO)+ subsequent to the completion (SUBTO) – at the different levels at 100 years (Fig. 8) show that the maximum values at the top of the building are in the order of 35 cm.

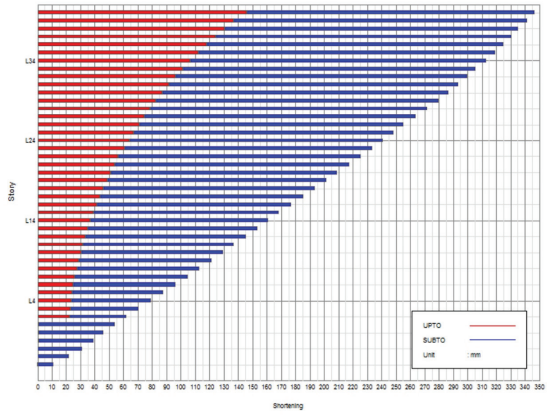


Fig. 8. Shortening at the different levels in column J6 at 100 years. UPTO (red) + SUBTO (blue) shortening

The horizontal displacements present a maximum value at the top of the building of about 25 cm (Fig. 9). The differential shortening between adjacent vertical members results about 5-6 cm at the top of the building (Fig. 10). Although these displacements values are very significant, it must be noted that the shortening that occurs up to the completion of the floors is usually not very important, at least for a cast-in-place concrete structure, since the slabs are levelled at the time of casting. Nevertheless, the shortening that occurs after the completion of the floors appears also significant, the absolute maximum values being in the order of about 20 cm (Fig. 8) and the relative ones (between adjacent vertical members) in the order of 2-3 cm (Fig. 10).

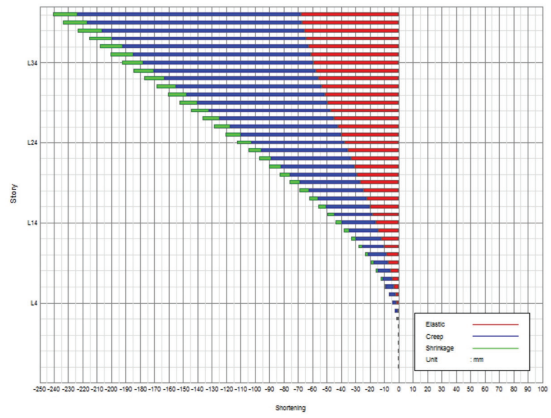


Fig. 9. Horizontal displacements at the different levels in column J6 at 100 years. Total (UPTO + SUBTO) displacements. Elastic (red) + Creep (blue) + Shrinkage (green)

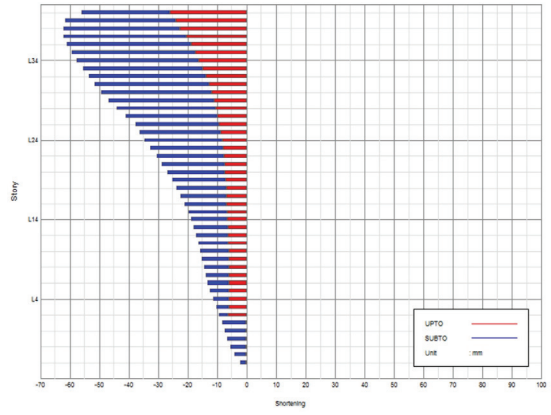


Fig. 10. Differential shortening between column H4 and wall J4 at 100 years. UPTO (red) + SUBTO (blue) shortening

5_CONCLUSIONS AND FUTURE DEVELOPMENTS

The time-dependent deformations of concrete play a significant role on the performance along the time of high-rise buildings and need to be properly taken into account in the design stage in order to avoid serviceability and structural concerns. The presented ASAP, specifically developed by Daewoo E&C for the prediction of time-dependent behaviour of high-rise buildings along the construction stage and at long term, allows structural engineers to evaluate these effects by combining 3D FE analysis and time-dependent analysis of structures. The validation process carried out in collaboration with the Politecnico di Torino evidenced the reliability of the software for the case studies and the prediction model considered. The analysis of the real case study relative to the Public Bank high-rise building evidenced a very significant influence of the time-dependent deformations of concrete on the long-term behaviour of the building, highlighting the need to take into account these phenomena and to adopt proper countermeasures, such as compensation of displacements (preset). The presented software allows taking into account in the analysis the effects of the adoption of different compensation measures.

In the future, fib 2010 (fib, 2013) and B4 (RILEM, 2015; Wendner et al., 2015a, 2015b and 2015c) prediction models will be also implemented in ASAP. For what concerns the review and validation process of the software, in this first step only GL2000 prediction model was considered. The next steps will concern the check of the correct implementation in the software of all other referenced prediction models. Other reference cases relative to sequential construction processes and compensation procedures may be considered as well. Finally, an effort will be made to set up monitoring programs in high-rise buildings. From long-term monitoring a positive feed-back may be obtained for the calibration of prediction models.

REFERENCES

1. ACI 209.2R-08 (2008), Guide for Modeling and Calculation of Shrinkage and Creep in Hardened Concrete.
2. ACI 209.3R-XX (2011), Analysis of Creep and Shrinkage Effects on Concrete Structures. Final Draft, Chiorino M.A. (Chairm. of Edit. Team), ACI Committee 209.
3. BAKER W. F., KORISTA S., NOVAK C., PAWLIKOWSKI J., YOUNG B. (2007), Creep & Shrinkage and the Design of Supertall Buildings. A Case Study: The Burj Dubai Tower, in Gardner J. and Chiorino M.A. (Editors) (2007), Structural Implications of Shrinkage and Creep of Concrete, ACI SP 246-07, 2007, pp. 135-150.
4. CARREIRA D. J. & POULOS T. D. (2007), Designing for effects of creep and shrinkage in high-rise concrete buildings. ACI SP 246-07, pp. 107-132.
5. CASALEGNO C., SASSONE M., CHIORINO M.A. (2010), Time dependent effects in cable-stayed bridges built by segmental construction. Proceedings of the Third International fib Congress, Precast/Prestressed Concrete Institute (USA), Washington, USA 29 May - 2 June.
6. CCIP-058 (2014), Tall Buildings. Structural design of concrete buildings up to 300 m tall. The Concrete Centre and fib (Fédération internationale du béton) Task Group 1.6. Also published as fib (2014), Tall Buildings. Structural design of concrete buildings up to 300 m tall, State-of-the-art report. fib Bulletin 73, August 2014.
7. CHIORINO M.A. & CARREIRA D. (2012), Factors affecting creep and shrinkage of hardened concrete and guide for modelling. A state-of-the-art report on international recommendations and scientific debate. The Indian Concrete Journal, Vol. 86, No. 12, pp. 11-24. Errata, Vol. 87, No. 8, August 2013, p.33.
8. CHIORINO M. A. & CASALEGNO C. (2012), Evaluation of the structural response to the time-dependent behaviour of concrete: Part 1 - An internationally harmonized format. The Indian Concrete Journal, Vol. 86, No. 12, pp. 25-36.
9. CHIORINO M.A., CASALEGNO C., SASSONE M. (2011), Numerical analysis of creep and shrinkage in high-rise concrete or steel-concrete buildings. Proceedings of the fib Symposium: Concrete engineering for excellence and efficiency, Prague, June 8-10.

10. CHIORINO M. A. & GARDNER J. (Eds.) (2007), Structural Implications of Shrinkage and Creep of Concrete. ACI SP-246.
11. EN 1992-1-1 (2005), Eurocode 2 - Design of concrete structures - Part 1-1: General rules and rules for buildings.
12. FINTEL M., GHOSH S. K., IYENGAR H. (1986), Column shortening in tall structures - prediction and compensation. Portland Cement Association.
13. GHALI A., FAVRE R., ELBADRY M. (2002), Concrete Structures - Stresses and Deformations. Spon Press. fib (2013), Model Code for Concrete Structures 2010. Ernst & Sohn.
14. HA T., LEE S., OH B. (2011), Prediction and control of movement of high-rise buildings during construction. Proceedings of the fib Symposium: Concrete engineering for excellence and efficiency, Prague, June 8-10.
15. Jirásek M. & Bažant Z. P. (2002), Inelastic Analysis of Structures. Wiley.
16. LAGOS R. C, KUPFER M. C., SANHUEZA T. S., CORDERO F. V. (2012), Costanera Center - Shortenings due to elastic deformation, creep and shrinkage of concrete in a 300-m tall building. The Indian Concrete Journal, Vol. 86, No. 12, pp. 53-60.
17. RILEM Technical Committee TC-242-MDC (Zdeněk P. Bažant, chair) (2015), RILEM draft recommendation: TC-242-MDC multi-decade creep and shrinkage of concrete: material model and structural analysis. Model B4 for creep, drying shrinkage and autogenous shrinkage of normal and high-strength concretes with multi-decade applicability. Materials and Structures, Vol. 48, pp. 753-770.
18. SAFARIK D., WOOD A., CARVER M., GEROMETTA M. (2014), CTBUH Year in Review: Tall Trends of 2013 – Small Increase in Completions Marks Return to Upward Trend. Annual Building Review. www.ctbuh.org.
19. SASSONE M., BIGARAN D., CASALEGNO C. (2007a), Numerical Approach to Viscoelastic Analysis of Concrete Structures Using Equilibrium and FEM. In: Gardner N. J., Chiorino M. A. (Eds.) Structural Implications of Shrinkage and Creep of Concrete, ACI SP 246, American Concrete Institute, Farmington Hill, Michigan, pp. 21-36.
20. SASSONE M. & CASALEGNO C. (2012), Evaluation of the structural response to the time-dependent behaviour of concrete: Part 2 - A general computational approach. The Indian Concrete Journal, Vol. 86, No. 12, pp. 39-51. Errata, Vol. 87, No. 8, August 2013, p. 33.
21. SASSONE M., CHIORINO M. A., BIGARAN D., CASALEGNO C. (2007b), Effects of creep and shrinkage on serviceability limit state. Proceedings of fib Symposium: Concrete Structures - Stimulators of Development. Dubrovnik, Croatia, pp. 623-632.
22. Wendner R., Hubler M. H., Bažant Z. P. (2015a), Optimization method, choice of form and uncertainty quantification of Model B4 using laboratory and multi-decade bridge databases. Materials and Structures, Vol. 48, pp. 771-796.
23. Wendner R., Hubler M. H., Bažant Z. P. (2015b), Statistical justification of Model B4 for drying and autogenous shrinkage of concrete and comparisons to other models. Materials and Structures, Vol. 48, pp. 797-814.
24. Wendner R., Hubler M. H., Bažant Z. P. (2015c), Statistical justification of model B4 for multi-decade concrete creep using laboratory and bridge databases and comparisons to other models. Materials and Structures, Vol. 48, pp. 815-833.

Safety and serviceability of reinforced concrete beam-column joints supported by shores and reshores during construction

하태훈
건축연구팀, 책임연구원
taehun.ha@daewooenc.com

본 논문은 2016년 Journal of Structural Engineering Vol.142, No.7에 게재되었던 논문을 재게재한 것입니다.

Abstract

Reshoring makes a floor support its own weight and decreases the construction load in the lower levels. However, a significant concern regarding reshoring lies in its safety and serviceability when shores are replaced while the construction load of the upper levels is applied. To investigate this concern and compare the construction load in shores and reshores, reinforced concrete (RC) beam-column joints at early ages were tested in the laboratory and were also monitored at a construction site. The specimens at ages of 2 and 3 days showed a shear-compression failure, and the specimens at ages of 7 or more days showed sufficient flexural behaviors. The test also found that the beam-column joints have sufficient stiffness even at the earliest ages that the joint can be safely assumed to be fully restrained regardless of the concrete age. Analysis of the test results showed that reshoring at five days of concrete age is 55% safer than keeping the shores until the age of 28 days, and no serviceability problems were identified, such as deflection, deformation, or cracks under the expected construction loads. The safety and serviceability concerns were also addressed by the field monitoring of beam deflections and the strain of the longitudinal rebar in the beams. The maximum beam deflection was only L/5,000, and the maximum rebar strain was only 3.6% of the yield strain. Field monitoring of the construction load showed that the load on the shores decreased by 50% after reshoring and was also 35% lower than the load on shores that have been kept. This result coincides well with the predicted values from the simplified analysis of ACI 347.2R-05.

Keywords : shore, reshore, safety, serviceability, early age concrete, construction load, field monitoring

1_INTRODUCTION

Construction loads in multistory reinforced concrete (RC) buildings are distributed by shores to the stories below (AIA 2014 and ACI 301 2005). As construction technologies progress and the demand for rapid construction increases, interest in reducing the construction time of shores increases, but early removal of shores is still considered to be one of the main causes of construction safety accidents. To prevent the collapse of RC floors during concrete pouring, shores are usually kept under a floor until the concrete of the floor reaches 28 days. By using prefabricated drop-head shores, the formwork under the floor can be removed without removing the shores.

Reshores are the shores that are placed snugly under a stripped concrete slab or other structural member after the original forms and shores have been removed from a large area, requiring the new slab or structural member to deflect and support its own weight (ACI 347 2005) and alleviating additional construction

loads on the lower levels (Kim 2010). Reshoring also reduces the amount of formwork and shores through early stripping of floor formwork and relocating shores according to the required amount and location. However, the reshoring also requires due caution (ACI 347 2005, AIA 2014, and AIK 2006) on engineering analysis and execution in the construction field against adverse effects on the floor, such as cracks and deflection, due to the early removal of shores.

Studies that evaluate the construction loads on shores have been performed using analytical methods and by monitoring field observations. Grundy and Kabaila (1963) developed a simplified method to evaluate the construction loads on slab and shores addressing the effects of the number of stories supported by shores, the construction period per story, and the material properties of the early-age concrete. Based on this method, ACI 347 (2005) provided a guideline for shoring/reshoring of concrete multistory buildings. Mosallam and Chen (1991) proposed a different method in which the total construction load is redistributed to the slabs according to the concrete stiffness ratio whenever a new construction load is superimposed. Kim (2010) calculated the construction loads on slabs considering various construction conditions.

Measured shore loads during construction have been reported. Fang et al. (2001) measured the axial forces of shores in two floor slabs during construction using strain gauges attached to the shores. Puente et al. (2007) and Kim et al. (2008) reported shore loads measured in a flat-plate structure under construction. Park et al. (2011) proposed a procedure to determine the slab construction load considering the effects of shore stiffness and concrete cracking. The proposed procedure was verified by comparing measured and predicted shore loads.

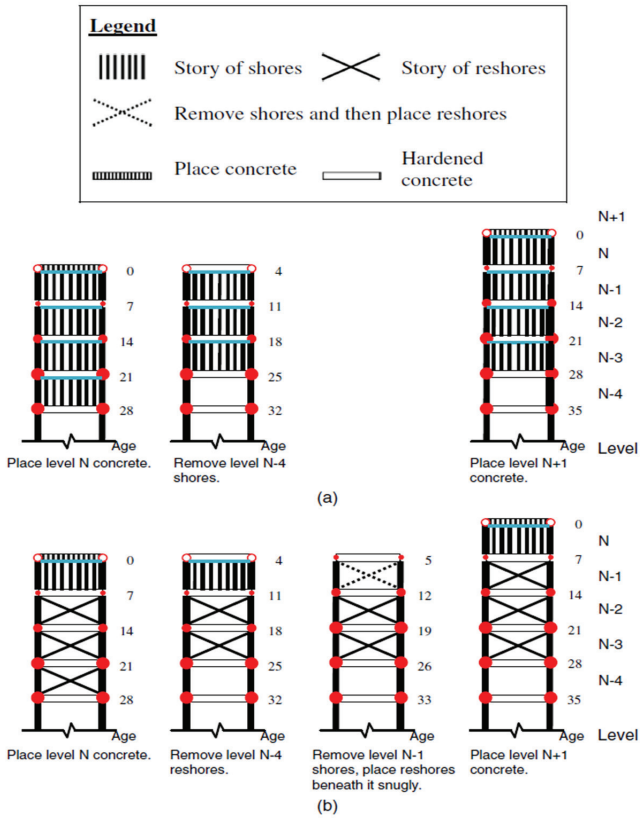


Fig. 1. Comparison of construction schemes: (a) shore, (b) reshore

The capacity of RC member subjected to early-age loading is one of main concern for the reshoring operation. Design codes assume that the specified strength of concrete is sufficiently developed and the concrete matures. However, most studies on early-age loading were focused on the deflection (Gardner and Fu 1987, Rosowsky et al. 2000, Park et al. 2012, Stivaros 2012, and Kang et al. 2013). Karayannis and Chalioris (2000) reported the influence of the early-age loading sequence on the final capacity of the RC beam-column joints.

Stivaros (2012) conducted case studies on two building constructions and indicated that ACI's requirements for the minimum slab thickness to control deflection are not sufficient since they do not account for the effects of high construction loads at early-age of concrete members and the resulting initial cracking. Analytical study on the serviceability of RC beams under early-age loading was also conducted by Rosowsky et al. (2000).

In this study, the development of loads in RC floors during the construction of a multistory building was first analyzed and compared for the case of keeping the shores and reshoring. Early age RC beam-column joints were then tested to evaluate the structural safety and serviceability of the RC floors during reshoring. To verify the test results, similar RC beams in the construction of the multistory building were monitored for their deflections and the strain in their longitudinal rebar. The differences in construction loads on shores were monitored in parallel for areas on shores and reshores to identify the reduction of shore loads in reshoring.

2 ANALYSIS OF THE CONSTRUCTION LOAD

Two construction sequences are illustrated in Fig. 1: Fig. 1(a) shows keeping the shores, and Fig. 1(b) shows reshoring. Common assumptions between the two construction sequences are that the construction period for each level is 7 days and the shores and reshores are kept on 4 consecutive levels under the level of concrete pouring. The shores and reshores at level N-4 are removed four days after the concrete pouring at level N. The reshoring occurs on day 5 when the original shores and forms are removed at level N-1 and the shores are placed snugly under the stripped concrete slab or beam.

To evaluate the construction loads on floors for these construction sequences, the simplified method developed by Grundy and Kabaila (1963) was used. The method assumes that the loads being applied or removed are distributed among the floors, connected by infinitely stiff shores or reshores, in proportion to the flexural stiffness of the floor structure. By neglecting the difference in the stiffness, the method is further simplified that the loads are distributed equally among the floors. It is also assumed that the shores are spaced close enough to treat the shore reactions as a uniformly distributed load. The deflection of the floors is considered purely elastic: creep and shrinkage of concrete are neglected.

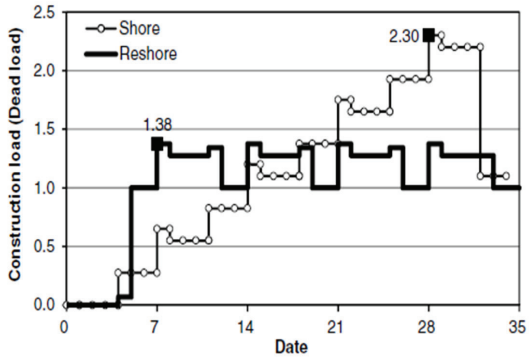


Fig. 2. Construction loads with different construction schemes

Result of the simplified method is shown in Fig. 2. The construction loads are considered as multiples of the floor's dead load, D, the assumed construction live load is 0.4D, and the assumed weight of the shore and form is 0.1D. The construction live load is assumed to exist only on the date of concrete pouring, and the weight of the shore and form is assumed to last until the date of reshoring.

As shown in Fig. 2, the maximum construction load on floors continually increases to 2.3D on day 28 when keeping shores, whereas for reshored floors, the maximum load reaches 1.38D on day 7 and is repeated when pouring concrete at each level. This difference is due to the accumulated loads on the lowest floor of

shoring when keeping shores. If the live load on a floor is assumed to be 65% of its dead load, then the design load of the floor is calculated as 2.24D (=1.2D+1.6L=1.2D+1.04D), which is lower than the construction load mentioned above when keeping shores. The structure will not fail in this condition considering the overstrength factor of the structure and other neglected inputs in the simplified method, such as the rotational stiffness of connections and the partial distribution of the load to columns and/or walls. However, as the floor's dead load occupies a high fraction of the total load which the floor is to carry in service, the load is greater than the structure's serviceability capacity (Grundy and Kabaila 1963) and is enough to cause structural cracks in the floors.

Although the reshoring redistributes the construction load to the already built levels below, the reshored floor structure, i.e., the beams and slabs, must support a relatively greater construction load at early ages—its own weight on day 5 plus a fraction of the construction load from level N+1—compared to keeping the shores. Therefore, sufficient strength is required for the reshored floor to support the expected maximum construction load at early ages. The reshored floor should also satisfy the serviceability requirements to control cracks and deflections, which influence the construction of follow-on trades and the durability of the structure.

3_EXPERIMENTS ON EARLY AGE REINFORCED CONCRETE BEAMS

3.1. Design of Specimens

The specimens were designed as shown in Fig. 3 to simulate an interior beam-column joint in the floor system of a multi-story building under reshoring condition. Figure 4(a) shows a bending moment diagram of the top frame of which the upper levels are not yet constructed when the shores at level N-1 are removed. The bending moment is the greatest around the beam-column joints. The specimens were modeled to simulate the joint of two beams and a column bounded by the inflection point of each beam as shown in Fig. 4(b). The distributed load is simplified as two point loads in Fig. 4(c) and the model is inverted for a better test configuration as shown in Fig. 4(d).

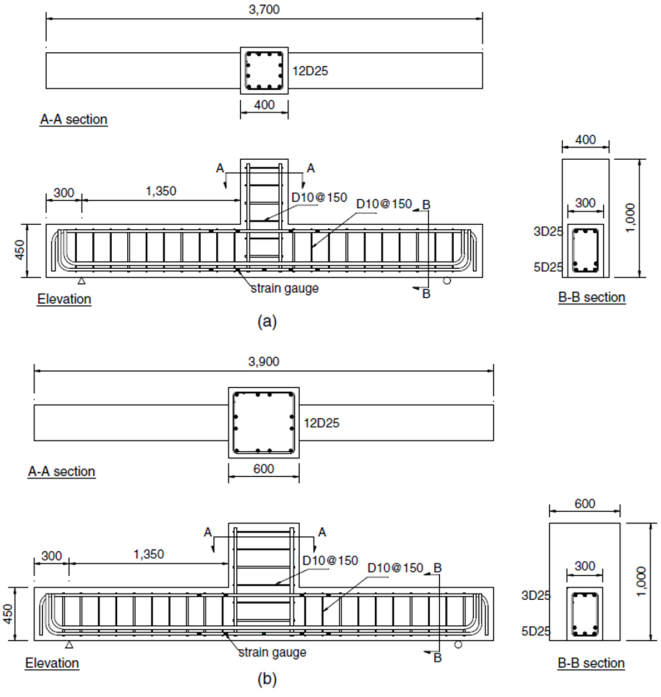


Fig. 3. Specimen details: (a) C400 specimens, (b) C600 specimens

The age of the specimen was set as the first variable of the experiment to identify the safety and serviceability of the early-age structure during the reshoring process. The size of the column section was selected as an additional variable because beam deflection, the most critical index of serviceability, is expected to be influenced by the stiffness of the beam-column joint. Two types of column dimensions were selected for the square section: one of 400 mm and another of 600 mm. The column dimensions were simply determined to meet the requirements on dimensions, strengths, stiffness, and details of columns and joints of ACI 318-14.

The sectional dimension of the beam is 300 × 450 mm, and the nominal distance from the column face to the support is 1,350 mm, which is designed to be three times the beam height. The beam dimensions of the monitored building of 400 × 500 mm were referred to in designing the specimens. For longitudinal reinforcing of the beam, 5 No. 25 rebars were used as bottom reinforcement and 3 No. 25 rebars were used for top reinforcement. In the actual structure, the position of the rebar needs to be inversed. For shear reinforcement, closed stirrups of No. 10 rebar were installed 150 mm apart. The material strength of the concrete was 27 MPa, which is typical for a floor structure, and that of the rebar was 400 MPa. The column of the specimen was designed to have a greater strength than the beams and had 12 No. 25 rebars enveloped by No. 10 hoops with 150 mm spacing.

3.2. Loading and Measurement

The load was applied in a monotonic manner by an actuator with a 1,000 kN capacity, as shown in Fig. 5(a). Until the load reached 250 kN, which is approximately 50% of the expected maximum load, the loading was controlled by the load on the actuator. Subsequently, the loading was controlled by the displacement of the actuator. The loading continued after the peak load until the strength of the specimen decreased to 85% of the peak load. The load was applied at a rate of 15 MPa/sec and below according to the requirements in ASTM E8/E8M-09 (2009).

The load was measured by an internal load cell in the actuator. The vertical deflection of the specimen was measured by LVDT (linear variable differential transformer) at five locations: one at the center and two each on the left and the right. The deformation of the specimen was measured in detail by dividing the specimen in five regions, as shown in Fig. 5(b). The LVDTs were installed in the horizontal direction at the top and bottom of each region to identify the specimen's curvature. Diagonally installed LVDTs were used to identify the shear deformation.

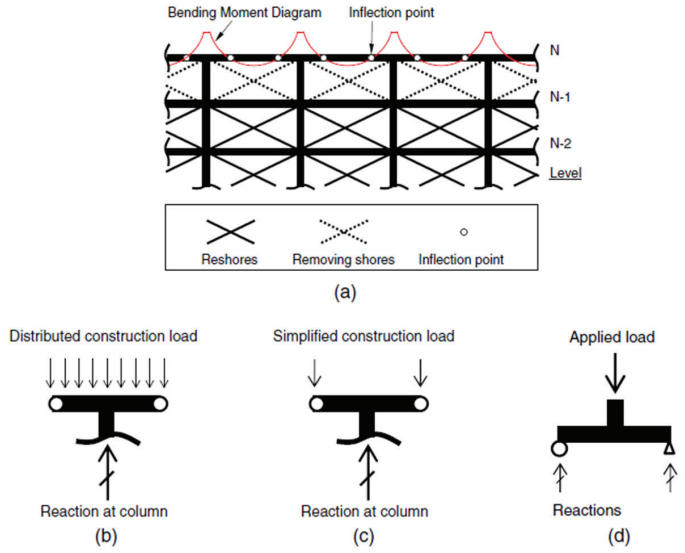


Fig. 4. Test model: (a) bending moment diagram of beams at level N when removing shores, (b) free body diagram between inflection points including column, (c) simplifying construction load as two point loads at the inflection points, (d) inverted model

Strains in the longitudinal rebar were measured by foil gauges, and their locations are shown in Fig. 3. Five strain gauges were installed for the tension rebar: one at the center, one at each of the interfaces of the column and beams, and the other two in the span of the beams on both the left and the right. For the compression rebar, four strain gauges were installed, omitting the one at the center compared to those on the tension rebar. The gauges were installed in pairs on the opposite rebar surfaces to prevent distortion from bending.

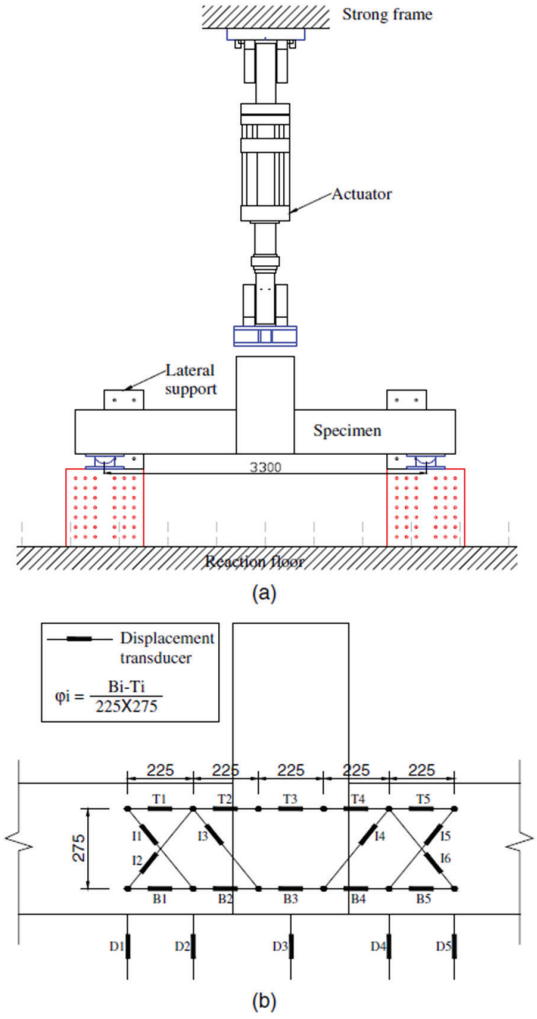


Fig. 5. Test setup and instrumentation: (a) test setup, (b) instrumentation

3.3. Results of the Material Tests

Material tests were performed for every three cylinder specimens on each day of the experiment on the beam-column joint specimens. The mean compressive strength of the concrete at 28 days was 32.2 MPa. The stress-strain relationship for each specimen was obtained from the internal load cell in the UTM (universal testing machine) and the strain gauges attached on the surface of the specimen, as shown in Fig. 6. All of the specimens, including those at early ages, exhibited typical stress-strain relationship. The strains at the maximum stress also showed no specific relationship to the concrete age, and their mean value was 1,800 μmm/mm. According to the tensile tests on the rebar, the mean yield strength and the tensile strength of the No. 25 rebar were 467.2 MPa and 609.5 MPa, respectively, whereas those of the No. 10 rebar were 504.2 MPa and 590.8 MPa, respectively.

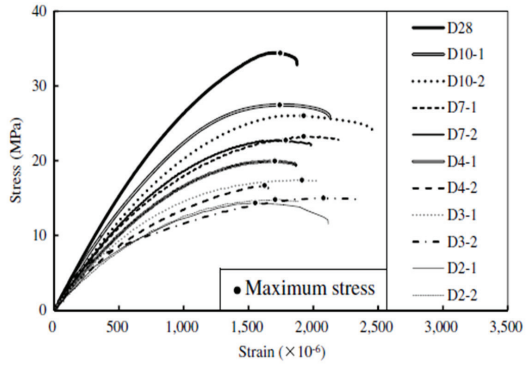


Fig. 6. Stress–strain relationships of concrete cylinders

3.4. Failure Mode and the Maximum Strength

Specimens of the beam-column joint after failure are shown in Fig. 7. Specimens at ages of 2 and 3 days failed in shear right after the extreme tension rebar yielded. The failure was of a shear-compression type where diagonal cracks penetrated into the compression region near the column surface. The specimens at an age of 4 days also failed by crushing of the compression region near the column surface but also with some deflection after the rebar yielded. The specimens at ages of 7 or more days exhibited flexural failure with shear cracks, where additional deflection of more than that required for the rebar yielding developed be-

fore the specimens failed by crushing of the compression region. Although differentiating each failure mode only by the visual inspection of the crack patterns on the specimens is difficult, a comprehensive analysis based on the load-deflection curves and the rebar strain data confirms the above classifications. The failure modes of each specimen with its maximum strength, predicted strength, deflection at rebar yielding, and deflection at failure are summarized in Table 1.

Two load-deflection curves are shown in Fig. 8, each grouped for the same column section. The hollow circle on each curve

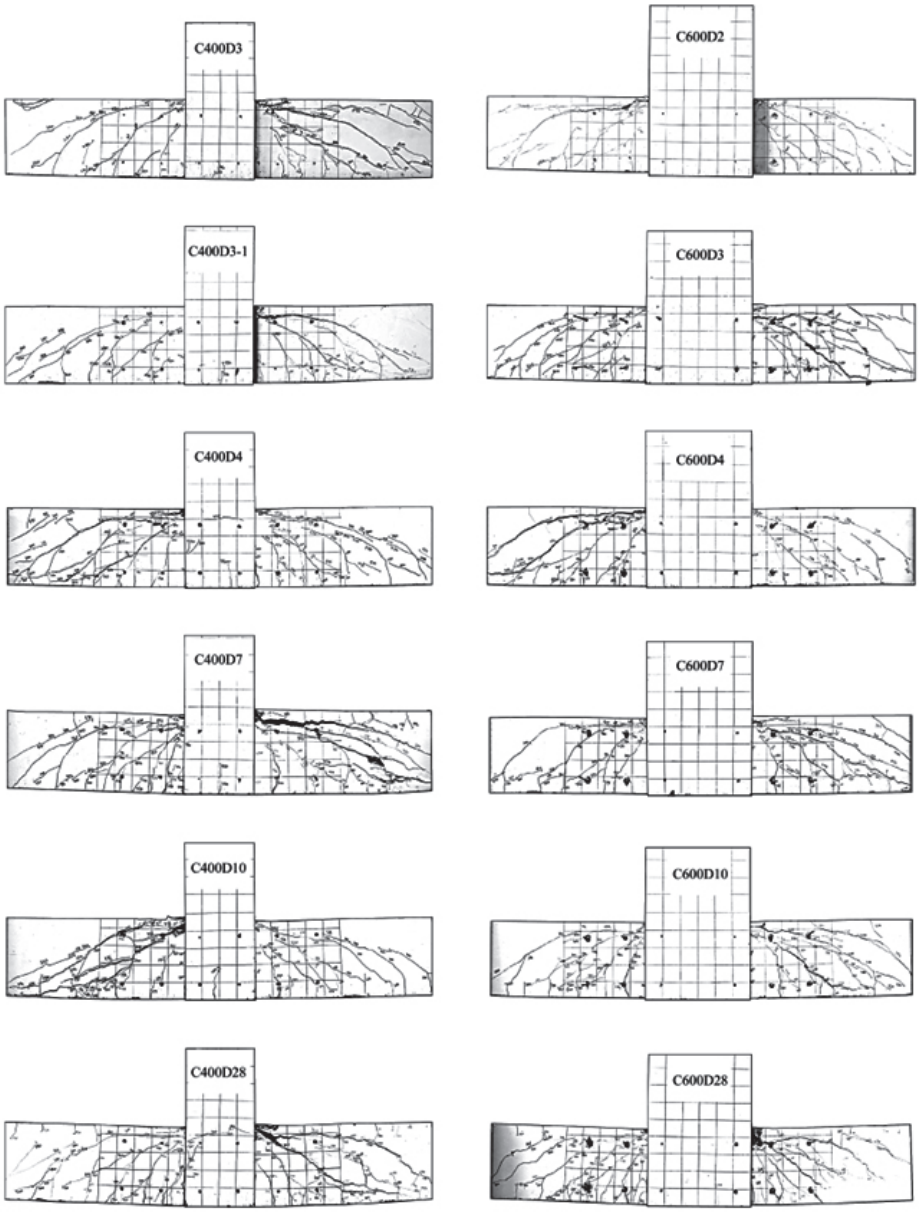


Fig. 7. Observed damage after testing

Table 1. Test results

Specimen	Age (days)	f_{ck} (MPa)	Failure mode	P_e (kN)	P_{ns1} (kN)	P_{ns2} (kN)	P_{nf} (kN)	δ_y (mm)	δ_u (mm)
C400D3	2.9	16.0	Shear	474	488	429	516	18.34	23.94
C400D3–1	3.2	16.9	Shear	469	491	441	518	16.76	14.08
C400D4	4.1	18.1	Flexural	556	497	457	521	15.82	39.06
C400D7	7.1	23.2	Flexural	574	518	518	530	15.22	56.30
C400D10	10.1	26.9	Flexural	576	531	531	536	13.82	39.36
C400D28	27.8	32.2	Flexural	602	549	549	544	13.96	67.90
C600D2	2.1	13.0	Shear	469	468	381	494	19.74	25.84
C600D3	3.1	16.7	Shear–Flexural	530	486	433	513	17.64	31.92
C600D4	3.9	17.8	Shear–Flexural	539	491	448	515	17.02	30.54
C600D7	6.9	22.9	Flexural	568	512	511	525	15.24	38.34
C600D10	10.0	26.7	Flexural	585	526	526	531	16.62	43.24
C600D28	28.0	32.2	Flexural	610	544	544	539	14.12	61.88

Note : In specimen name C①D②, ① represents column dimensions and ② represents the age of specimen after casting the concrete. P_e = measured strength, P_{ns} = predicted shear strength based on the actual material properties, P_{nf} = predicted flexural strength based on the actual material properties, δ_y = deflection at yielding of the extreme tension rebar, and δ_u = deflection at failure.

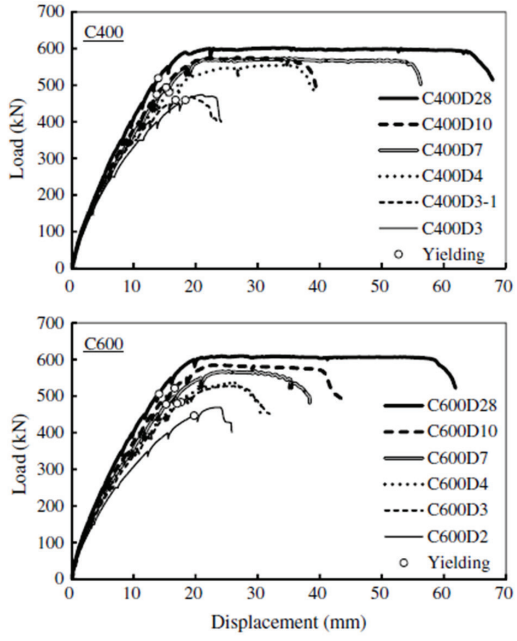


Fig. 8. Load–deflection relations

marks the point of yielding of the extreme tension rebar. Ductile behaviors are easily identified with clear yield plateaus for the C400 specimens at ages of 4 or more days and for the C600 specimens at ages of 7 or more days. In contrast, the specimens at ages of 2 and 3 days show brittle behaviors with a sudden decrease in load after reaching the peak value. Concrete age clearly affects the maximum strength, failure mode, and ductility. At early ages, low concrete strength accompanies limited strain in the tension rebar and leads to low ductility. At ages of 7 or more days, the specimens show sufficient flexural behavior in terms of strength, failure mode, and ductility.

The strengths corresponding to the shear and flexural capacities of the beam are defined as P_{ns1} and P_{nf}, respectively, and are shown in Fig. 9. The early age specimens C400D3, C400D3-1 and C600D2 failed at loads similar to or slightly below the shear strength, P_{ns1}. These specimens had low concrete strength and hence were expected to fail in shear. Due to the low concrete strength at early ages, the shear strength provided by the shear reinforcement, V_s, becomes more than twice the shear strength provided by the concrete, V_c. In this condition, the design code (ACI 318 2014) requires that the maximum spacing of the shear reinforcement, $d/2$, be reduced by one-half, to $d/4$. However, because the stirrups in the specimens were designed based on the concrete strength at 28 days, the spacing was determined to be

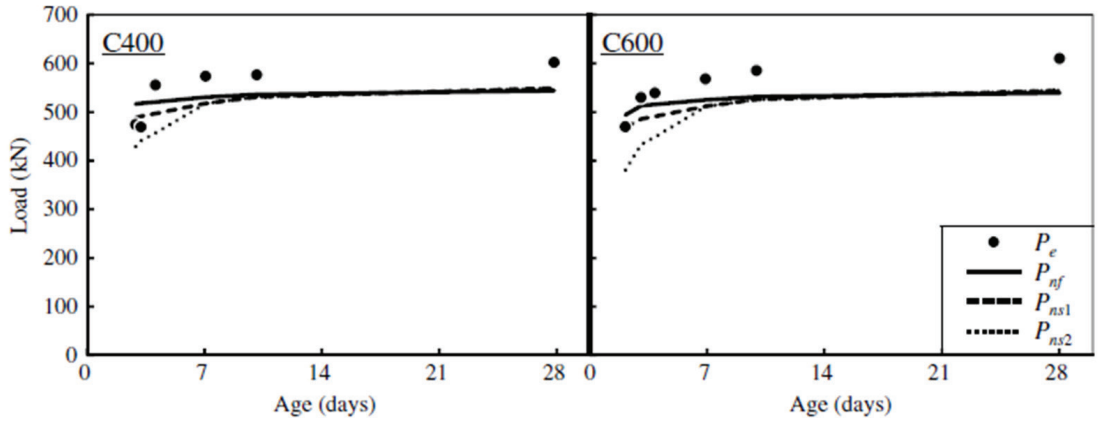


Fig. 9. Load resisting capacities with varying ages

150 mm, which is less than *d*/2 but greater than *d*/4. Therefore, the yield strength of the stirrups shown in the material tests is not expected to be fully developed in the test specimens.

In the seventh column of Table 1, the alternatively evaluated shear strengths, P_{ns2}, are presented; here, the shear strength provided by the stirrups is intentionally set as twice the shear strength provided by the concrete. These strengths are represented as smaller dotted lines in Fig.9. When compared to the revised shear strength, even the specimens that failed in shear show higher measured strength than the predicted strength by a minimum margin of 6%. The specimens that failed in flexure have more than 9% over-strength compared to the predicted strength.

3.5. Flexural Deformation

The curvature of the specimens was estimated by measuring the longitudinal deformation along the top and bottom of the beams at five regions, as shown in Fig. 5(b). At the joint area, the maximum curvatures of the C400 specimens are 0.0025 m^{-1}, and for the C600 specimens, all of the curvatures are below 0.0005m^{-1}. These curvatures amount to only a tenth of the curvature at the beam-column interface when yielding of the specimens occurs. Therefore, the curvature has a negligible effect on the total deformation and also on the deflection of specimens considering the curvature-deflection relationship. Moreover, because the curvatures are small irrespective of the specimen ages, the joints are considered to have sufficient stiffness even at early ages of concrete. The stiffness of the joint depends on the concrete modulus of elasticity. The material tests showed that the modulus of elasticity at 7 days was 75% of that at 28 days. The code predictions (ACI2092008) are even higher: the modulus of elasticity at 7 days according to Eq. (1) is 84% of that at 28 days. Therefore, the joint stiffness at 7 days is expected to have reached more than 75% of the design stiffness.

$$E_{ct} = 0.043\gamma_c^{1.5}\sqrt{f_{cmt}} \quad (1)$$

where E_{ct} is the secant modulus of elasticity of concrete according to Eq. (A-16) of ACI 209 (2008), g_c is the unit weight of concrete (kg/m^3), $f_{cmt} = f_{cm28}t/(4+0.85t)$ is the strength of concrete at age *t* in MPa according to Eq. (A-17) of ACI 209 (2008), and f_{cm28} is the strength of concrete at age 28 days in MPa.

In RC structures, the maximum moment usually develops at the beam-column interfaces, and plastic hinges also develop at these interfaces in the direction of the beams under ultimate load conditions. The load-curvature relations in the beam regions including the beam-column interface are shown in Fig. 10. The measured curvatures were calculated from the displacements measured by the LVDTs as shown in Fig. 5(b). The curvatures were evaluated from the averaged displacement in the small region of 225 mm width but still exhibit variations according to the formation and

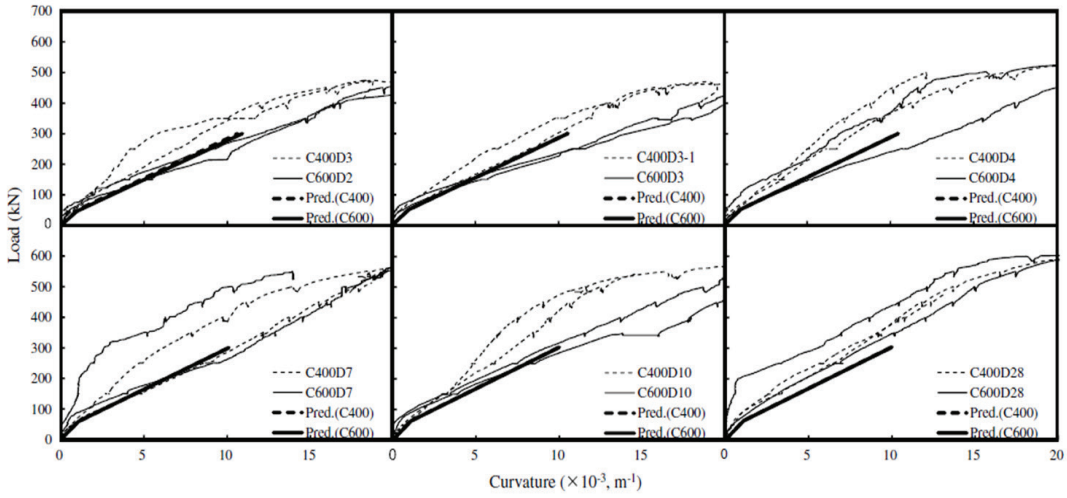


Fig. 10. Load–curvature relations at column faces

development of cracks: initially stiff slopes under cracking load and reduced stiffness after flexural cracks appear at the critical section. The flexural stiffness (*EI*) was calculated based on the result of the material tests and was then compared to the measured values in each graph in Fig. 10. The measured stiffness is greater than the predicted stiffness in most cases due to the differences in the moment of inertia. The predicted stiffness uses the moment of inertia of the cracked section, in which the concrete in tension is neglected after cracking, while the residual tensile strength of concrete between cracks is deemed to have contributed to the measured stiffness as a tension stiffening effect. Moreover, a partial contribution to the measured stiffness is expected to have come from the greater breadth of the column section along the measured distance. Greater measured stiffness than predicted stiffness is shown for all of the specimen ages. Therefore, the flexural stiffness and behaviors at early ages are considered to follow the assumptions in the design.

3.6. Shear Deformation

Although concrete at early ages has low strength and stiffness, the flexural strength of RC beams is less affected by the strength of concrete than it is by the amount and type of steel reinforce-

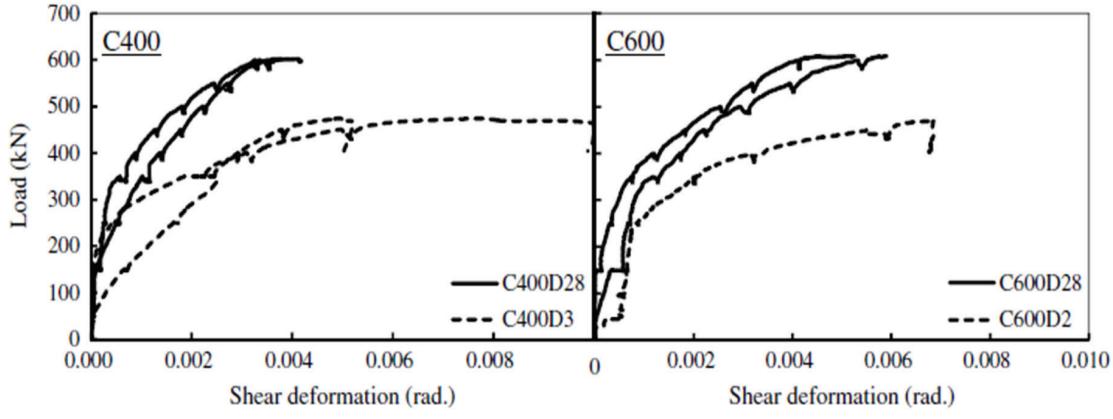


Fig. 11 Load–shear deformation relations with different ages

ment. According to the nominal flexural strength, P_{nf}, of the C600 specimens presented in Table 1, the flexural strengths at ages of 2 and 3 days are 92% and 95% of the flexural strength at 28 days, respectively. However, the ratios of the nominal shear strength, P_{ns1}, at the same days reach only 70% and 80%, respectively.

Shear deformations measured on the specimens at different beam locations are compared in Fig. 11 for different concrete ages. Shear deformations of specimens at 2 and 3 days are greater than those at 28 days, and the difference increases after the load reaches 300 kN. At this load, the flexural cracks dominated the whole span of a beam, and some of the cracks developed diagonally in the direction of the column. The measured shear deformation therefore includes not only pure shear deformation due to the shear modulus of concrete but also the deformation originating from the inclined cracks. Because the shear modulus is proportional to the modulus of elasticity, the former is not more affected by the concrete age than the latter is. The large shear deformation at early ages is considered to be more affected by the inclined cracks than by the shear modulus.

3.7. Safety and Serviceability of a Reshored Floor

Using the information with the test data of the strength and deformation at different ages, the reshored floor can be evaluated for its safety and serviceability. The relative safety factor, *R.S.F.*(*t*), is defined for this purpose, in which the strength at different ages normalized by the strength at 28 days is divided by the expected construction load at the corresponding age, also normalized by the load at 28 days.

$$R.S.F.(t) = \frac{P_e(t)/P_e(28)}{CL(t)/CL(28)} = \frac{P_e(t)/CL(t)}{P_e(28)/CL(28)} \qquad (2)$$

where $P_e(t)$ and $P_e(28)$ are the maximum measured strengths at ages t and 28, respectively, and CL(t) and $CL(28)$ are the expected construction loads at ages t and 28, respectively, as shown in Fig. 2. As been derived in the last term of Eq. (2), *R.S.F.*(*t*) is the safety factor evaluated at age t against the safety factor at 28 days.

As shown in Fig. 2, a reshored floor undergoes the maximum construction load at 7 days but the load is only 60% of the maximum construction load at 28 days when keeping shores. The strengths at that age, however, reached 95% and 93% of those at 28 days for the C400 and the C600 specimens, respectively. Relative safety factors with varying ages for C400 specimens are shown in Fig. 12 and those for C600 specimens show almost same trend of Fig. 12. Reshoring exhibits better safety than keeping shores because the former has a higher relative safety factor. This argument is still effective even if a ratio of different strength reduction factors, i.e., $f_s/f_f = 0.75/0.9 = 0.83$, is applied to the structure at 7 days with an assumption that the structure fails in shear.

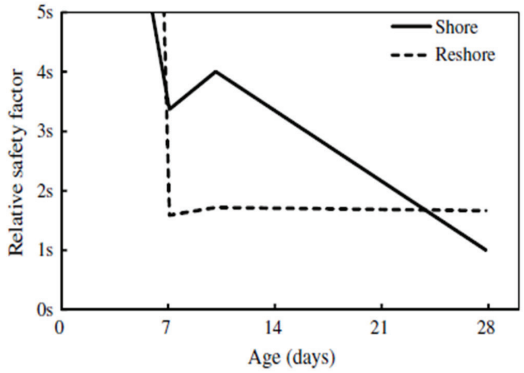


Fig. 12. Relative safety factors of C400 specimens with varying ages and construction schemes

Reshoring is also better than keeping shores in terms of the structural efficiency. While the relative safety factor for reshoring is kept almost consistent after 7 days, that of keeping shores is unnecessarily high at early ages and constantly decreases until 28 days.

To evaluate the serviceability of a reshored beam, the deflections and the tensile deformations are compared in Fig. 13. Because the condition of the construction loads is unique for each structure, the structure is assumed to be appropriately designed for the construction load. The construction load at an age of 28 days is also assumed to be the load that induces a rebar strain of 1,670 μmm/mm, i.e., 0.67 times the yield strain e_y. The criteria of $0.67e_y$ corresponds to the maximum rebar strain under service load (ACI 318 2014).

The deflections at $0.67e_y$ when keeping the shores until the age of 28 days are shown in Fig. 13(a) as solid circles. The expected construction loads at an age of 7 days for a reshored beam are 0.6

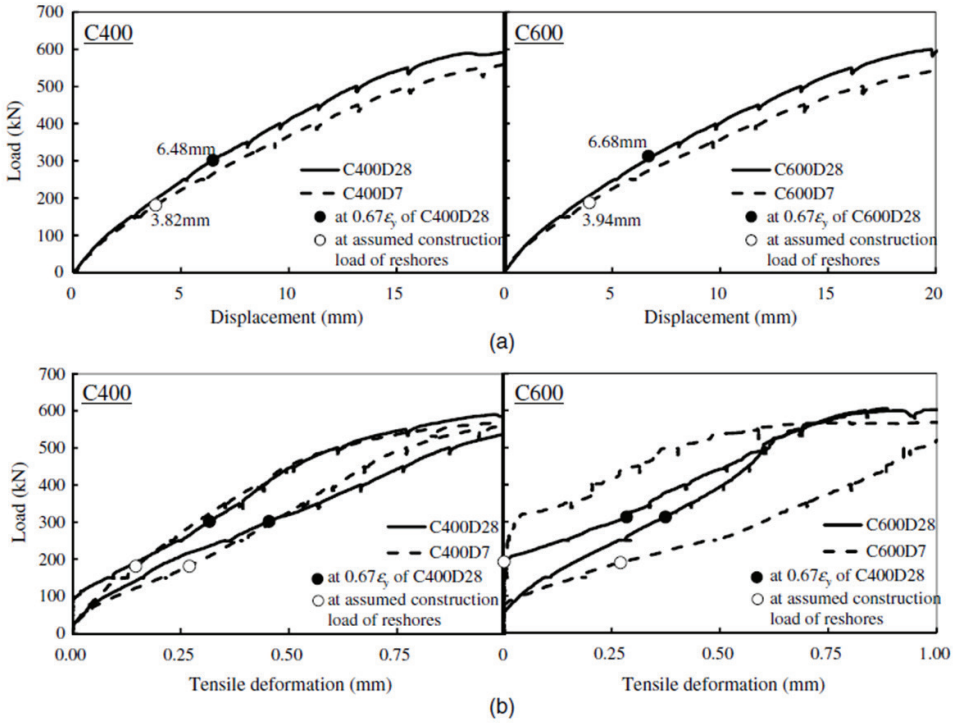


Fig. 13. Deflections and tensile deformation under expected maximum construction loads: (a) deflections, (b) tensile deformation at the centroid of tension bars at column faces

times of a shored beam as provided in Fig. 2. The deflections of the reshored beam, marked as void circles in Fig. 13(a), are almost proportional to the ratio of construction load that they reach only 60% of the deflection when keeping shores until 28 days.

The tensile deformations shown in Fig. 13(b) were derived from LVDT B2 and B4 in the region of the beam-column interface as shown in Fig. 5(b). These LVDTs were installed at the location of the centroid of tension bars. The region is composed of a column region of 87.5 mm and beam region of 137.5 mm. Because the region contained more than one crack, the tensile deformations in Fig. 13(b) mean the maximum crack width at the location of the tension rebar. The solid and void circles represent the tensile deformation under the expected construction loads at the ages of 28 days and 7 days, respectively. The maximum crack width under the expected construction load at 7 days is 70–82% of that when keeping shores until 28 days.

Despite the low strength and stiffness of the concrete at early ages, serviceability requirements are satisfied because the level of the expected construction load is also small.

4_FIELD MONITORING

As shown in the simplified analysis of the construction load, reshoring the floor structure is more effective than keeping shores in reducing the floor loads. However, the actual distribution of the construction load might be different in the construction of a real building compared to the ideal condition assumed in ACI 347.2R-05 (2005). A relatively higher construction load on the reshored floor, as shown in Fig. 2, might also damage the early age structure during the reshoring process. Field monitoring of the shores' load, the longitudinal rebar strain, and the beam deflection was performed to identify these issues.

4.1. Monitoring Scheme

The target structure is an RC-framed ten-story commercial building. To compare the construction loads in different shoring meth-

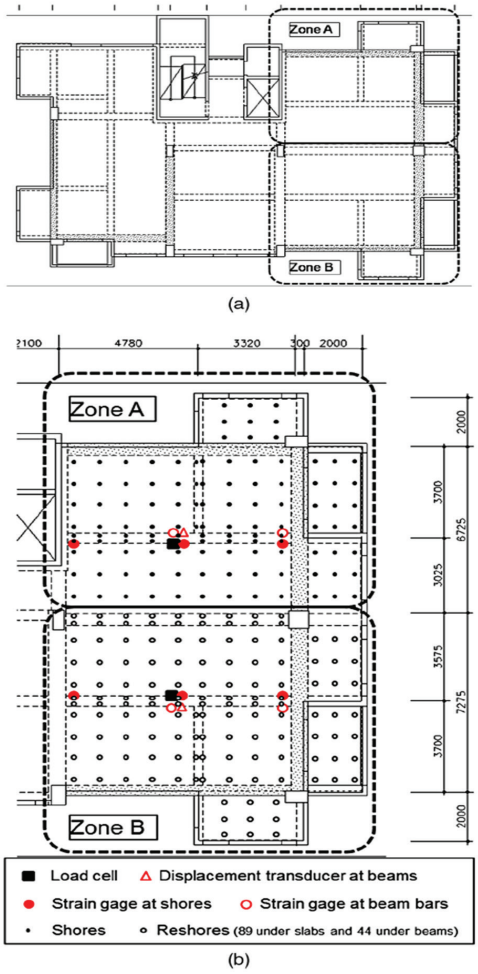
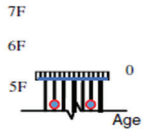
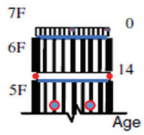
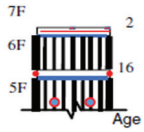
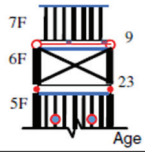


Fig. 14. Floor plan for construction load measurement (unit: mm): (a) plan, (b) locations of instrumentation

ods, two zones with similar plan layout were selected, as shown in Fig. 14. In Zone A, a conventional shoring method is adopted, i.e., the shores were kept continuously until the concrete of the floor of level 7 reached an age of 28 days or its design strength. In Zone B, the shores at level 6 were removed after the concrete strength reached more than 2/3 of the design strength and the shores were reinstalled at the same location before the concrete was poured on the floor of level 8. Special attention was paid during reshoring that the shores were snugly inserted between the floors so that they did not apply unwanted loads to the floors. The sequence of reshoring and the installation of monitoring devices are shown

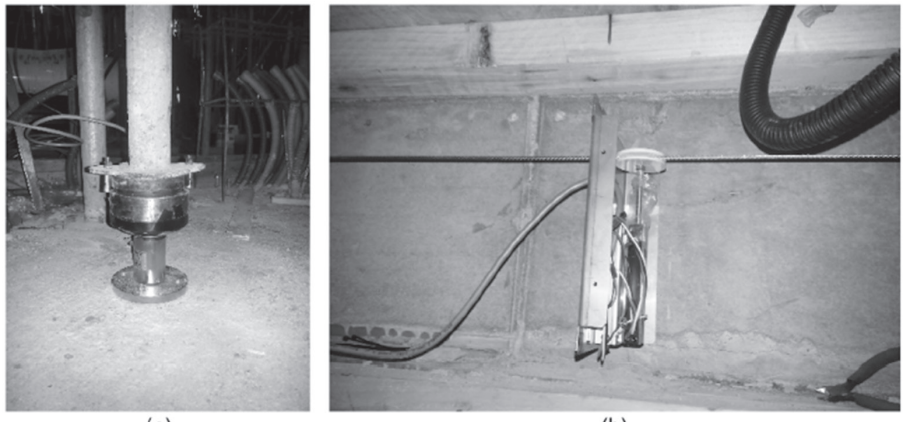
Table 2. Sequence of construction operations

Sequences	Operations
	Step 1 ▪ Install load cells and strain gauges at shores on the 5th floor. ▪ Place concrete at the 6th floor.
	Step 2 ▪ Install strain gauges at the beam longitudinal bars at the 7th floor. ▪ Place concrete at the 7th floor.
	Step 3 ▪ Install LVDT to measure the deflection of the beams at the 7th floor.
	Step 4 ▪ Rwmove shores on the 6th floor. ▪ Place the removed shores sung but not loaded.
Legend	Story of shores Story of reshores Strain gauges at beam longitudinal bars LVDT at beam Load cells and strain gauges at shores

in Table 2. The sequence of construction described in Table 2 is somewhat different from that in Fig. 2(b) because the target structure is reshored at level 6 only for the research purposes leaving all the other levels being kept shored until necessary.

To minimize the effect of neighboring spans with different shoring methods, two beams at the centers of each zone were selected as the monitoring locations. The shores' loads under the beams were measured at level 5, and the beam deflections and the top longitudinal rebar strains were measured for the floor beams at level 7. The monitoring locations and sensor types are presented in Fig. 14(b). The shores' loads were measured at the center and each end of the beams. Fig. 15(a) shows a load cell installed at the base of the shore and Fig. 15(b) shows an LVDT to measure the deflection of the reshored beam.

The concrete design strength is 27 MPa, and grade 75 (520 MPa)



(a) (b)

Fig. 15. Instrumentation settings: (a) load cell at the base of a shore, (b) LVDT at beam

rebar was used. The concrete strengths used in level 6 were 31.3 and 36.3 MPa at 7 and 28 days, respectively, and those used in level 7 were 27.0 and 31.3 MPa at 7 and 28 days, respectively. All the measured strengths at 7 days were above the design strength. The dead load on each shore equals a fraction of the beam weight and was evaluated as 2.12 kN. The beam has a rectangular section with b = 400 mm and h = 500 mm. Metal pipes were used to shore the slab in a grid pattern of 900 × 900 mm. These pipes were installed 900 mm apart in two rows under the beams.

measured data were initialized at the time of pouring concrete on the floor of level 6. The magnitudes of the loads are generally similar except for an abrupt gap when pouring the concrete on the floor of level 7 due to an unbalanced distribution of the load during concrete pouring. The difference gradually disappeared after one day and remained small until the load under the reshored region greatly decreased. The shores' predicted load when keeping shores as evaluated in the simplified analysis is also shown in the graph for comparison. The overall tendency of the loads is in

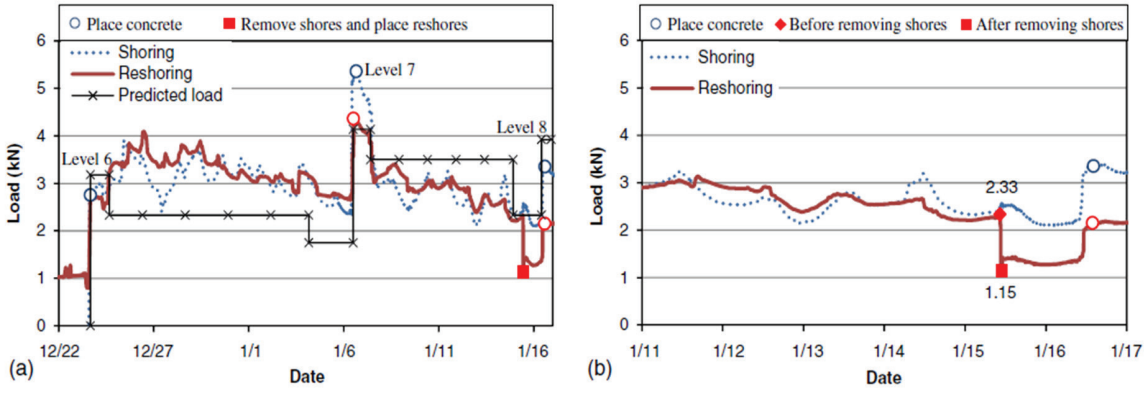


Fig. 16. Shores' loads measured at center: (a) during whole period of shores, (b) around placement of reshores

4.2. Result of Monitoring – Loads on Shores

The measured loads on the shores under the centers of the beams are shown in Fig. 16(a). To easily compare the loads, the

good agreement, but the measured values are higher than the predicted values after pouring the concrete on level 6 until pouring the concrete on level 7. Unexpected loads due to storage and/or

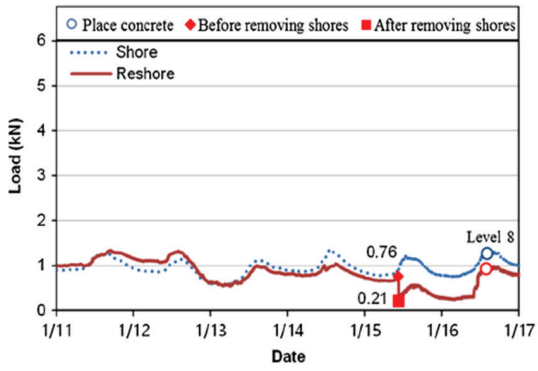


Fig. 17. Shores' loads measured at interior end

equipment on level 6 likely caused the difference.

The graph in Fig. 16(b) shows the shores' load during a part of the shoring period with an expanded time scale about the date of reshoring. When the reshoring is performed, the measured load on the shore under the reshored region instantly decreased from 2.33 kN to 1.15 kN, which equals a 50% drop in the load. After the reshoring process was over, the shore under the reshored region supported 35% less load than that under the shored region.

The shores' loads at the interior ends of the beams were generally less than those at the centers, and the reduction in the load due to reshoring was also less, as shown in Fig. 17. The construction loads on the shores under the ends of the beams are comparable to those under the center of the beams when the concrete in the shored structure is being poured. As the concrete age increases, however, the increased rotational stiffness of the beam-column joints restricts the beam deflections at the ends, and the loads on the shores under the ends of the beams decrease correspondingly. For example, when pouring the concrete on level 7, the maximum shores' load under the interior end of the beam in zone B is only 61% of the load under the center of the same beam. Considering the variation in deflections at different locations along the length of a beam, the number of shores can be reduced, especially at the interior end of the beam.

4.3. Result of Monitoring – Safety of the Reshored Floor

The safety of the reshored floor was evaluated by measuring the deflections and the rebar strains of the reshored beams. As shown in Fig. 18(a), little deflection was observed when the shores were removed. Because the concrete design strength in the floor of level 7 has already developed when the floor is reshored, the fully developed stiffness of the beams and joints resulted in

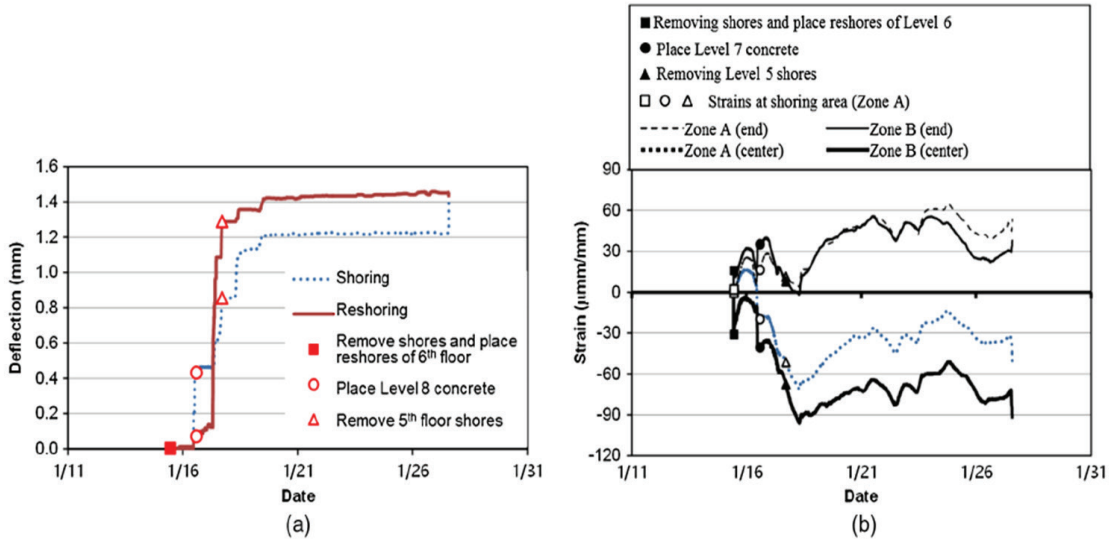


Fig. 18. Measured beam deflection and strains of beam longitudinal bars: (a) beam deflection, (b) strains of beam longitudinal bars

the small deflections. Further deflection of 0.23 mm developed in the reshored beam due to the pouring of concrete on the floor of level 8 and the removal of the shores on level 5. However, the maximum deflection corresponds to *L*/5,000 of the span length, *L* = 8,100 mm, and hardly affects the structure's safety and serviceability.

The strains of the longitudinal rebar at the top of the beams are shown in Fig. 18(b). Generally, the strains at the center of the beams are greater than those at the beams' exterior end due to greater positive moment than negative moment. During the reshoring process, the reshored beam had 30 μmm/mm more strain than the beams that were kept shored. The difference increased further by 48 μmm/mm afterwards and the maximum strain in the reshored beam reached 98 μmm/mm. This value amounts to 3.6% of the yield strain of grade 75 rebar and is in the sufficiently safe region considering that the full dead load was applied.

alized diagram of the load on the shores on level N-1 derived from Fig. 16(a). "A" represents the load increase due to pouring concrete on the floor of level N, and the corresponding measured value is 2.75 kN. "B" represents the load increase due to pouring concrete on the floor of level N+1 after placing reshores on level N-1 and is measured to be 1.64 kN. "C" represents the load decrease due to the reshoring process on level N and is measured to be 1.04 kN. The variation of the construction load on the floor structure under the reshoring process is estimated from that of the shores' load, as shown in Fig. 19(b). When placing concrete on the floor of level N, no construction load is applied on that floor and the load corresponding to D+A–B is applied on the floor of level N-1, where D represents the dead load of the floor. After placing reshores on level N-1, only the dead load is applied on the floor of level N and the load corresponding to D–B+C is applied on the floor of level N-1.

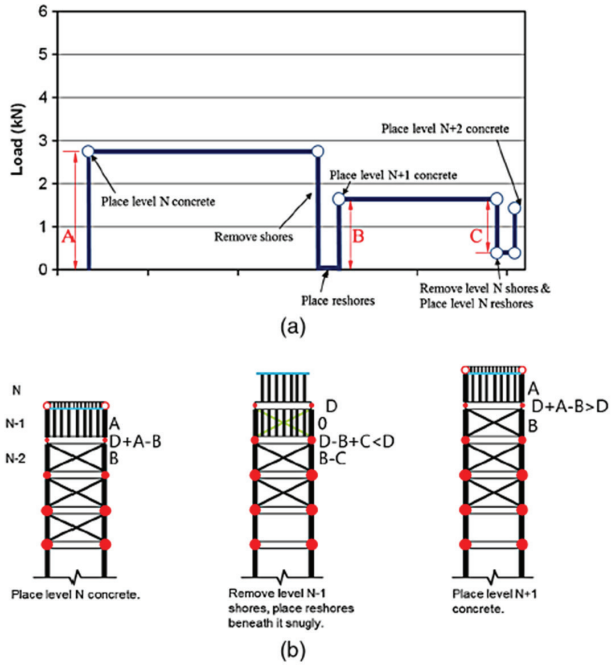


Fig. 19. Expected construction loads: (a) expected reshore loads, (b) expected floor structure loads

4.4. Evaluation of the Construction Load on the Floor

The purpose of measuring the shores' load was to evaluate the construction load on the floor structure. Fig. 19(a) is a generTherefore, the maximum construction load on floor structure is D+A–B, for which the measured value is 2.14 + 2.75 – 1.64 = 3.25 kN, corresponding to 1.52D. This value is similar to the

estimated theoretical value, 1.38D, obtained earlier from the simplified analysis.

5_CONCLUSIONS

In this study, the development of construction loads on the floor structure and the support structure was first predicted based on the simplified method recommended in ACI 347.2R-05. Early age RC beam-column joints were then tested to evaluate the structural safety and serviceability of RC structures during reshoring. Finally, on-site monitoring of a multistory building under construction was performed to verify the decrease of construction loads on a reshored floor compared to a floor that has been kept shored and to confirm the safety of the structure in the process of reshoring. The conclusions from this research are summarized below.

1) The test results of the RC beam-column joint specimens showed that the specimens at ages of 2 and 3 days failed in shear-compression and that the specimens at ages of 7 or more days exhibited sufficient flexural behavior where yielding of the tension rebar preceded the crushing failure of concrete in compression. Because the compressive strength of concrete influences the shear strength of an RC structure more than its flexural strength, careful evaluation of the shear strength is recommended when reshoring RC structures at early ages.

2) The maximum curvature of the specimens at the joints was only a tenth of the curvature at the beam-column interface when yielding of the specimens occurs. Because the joint provides a sufficient stiffness even at early ages, the assumption of a fixed connection used in the structural design is still effective for early-age RC structures.

3) If each floor is constructed in a 7-day cycle and the floors are reshored at an age of 5 days, the safety of the reshored floor is enhanced by 55% compared to the floors kept shored until 28 days. While the maximum construction load on reshored floors reaches only 60% of the maximum construction load when keeping shores, the strength of the structure at 5 days develops more than 93% of the structure strength at 28 days. The serviceability of the reshored structure is also satisfactory because the deflections and the crack widths of the structure at 7 days and under the expected construction load were less than those of the structure kept shored until 28 days and under increased construction load.

4) The results of the field monitoring showed that the load on the shores decreased by 50% when the floors just above the level are reshored. Furthermore, the reinstalled shores supported 35% less load than the shores that have been kept in position. The maximum deflections of the reshored beams were measured as *L*/5,000, and the rebar strain corresponded to only 3.6% of their yield strain. Therefore, for a conventional construction cycle of 7 days, reshoring a floor just before placing the concrete on the floor above will not cause problems in terms of structural safety or serviceability.

ACKNOWLEGEMENTS

This research is supported by the grant (Code#'09 R&D A01) from the High-Tech Urban Development Program funded by the Ministry of Land, Infrastructure and Transport in Korea.

REFERENCES

1. ACI Comm. 209. (2008). "Guide for modeling and calculating shrinkage and creep in hardened concrete." ACI 209.2R-08, Farmington Hills, MI, 44.
2. ACI Comm. 301. (2005). "Specifications for structural concrete." ACI 301-10, Farmington Hills, MI, 77.
3. ACI Comm. 318. (2014) "Building code requirements for structural concrete and commentary." ACI 318-14, Farmington Hills, MI, 315.
4. ACI Comm. 347. "Guide for shoring/reshoring of concrete multistory buildings." ACI 347.2R-05, Farmington Hills, MI, 18.
5. AIA. (2014). "AIA MasterSpec Section 033000 – Cast-in-place concrete." 17.
6. AIK. (2006). "Standard specification for building

construction." Seoul, 1470 (in Korean).

7. ASTM. (2009). "Standard test methods for tensile testing of metallic materials." E8/E8M-09, West Conshohocken, PA, 27.
8. Fang, D., Zhu, H., Geng, C., and Liu, X. (2001). "On-Site Measurement of Load Distribution in Reinforced Concrete Buildings during Construction." ACI Str. J., 98(2), 157-163.
9. Gardner, N., and Fu, H. (1987). "Effects of High Construction Loads on the Long-Term Deflections of Flat Slabs." ACI Str. J., 84(3), 349-360.
10. Grundy, P., and Kabaila, A. (1963). "Construction Loads on Slab with Shored Formwork in Multistory Buildings." ACI J., 60(12), 1729-1738.
11. Kang, S., Eom, T., and Kim, J. (2013). "Reshoring Effects on Deflections of Multi-Shored Flat Plate Systems under Construction." Str. Eng. & Mech., 45(4), 455-470.
12. Karayannis, C. G., Chalioris, C. E. (2000), "Capacity of RC joints subjected to early-age cyclic loading." J. Eq. Eng., 4(4), 479-509.
13. Kim, J. (2010). "Calculation of Slab Construction Loads in Multistory Shored RC Structure by Considering Construction Conditions." Comp. Str. Eng., 23(4), 44-54.
14. Kim, O., Kang, S., and Oh, J. (2008). "Field Instrumentation of Load Variation of Shoring in Apartment under Construction According to Construction Stage." Daelim Tech. Rev., (1), 67-75 (in Korean).
15. Mosallam, K., and Chen, W. (1991). "Determining Shoring Loads for Reinforced Concrete Construction." ACI Str. J., 88(3), 340-350.
16. Park, H., Hwang, H., Hong, G., Kim, J., and Kim, J. (2011). "Slab Construction Load Affected by Shore Stiffness and Concrete Cracking." ACI Str. J., 108(6), 679-688.
17. Park, H., Hwang, H., Hong, G., Kim, Y., and Kim, J. (2012). "Immediate and Long-Term Deflections of Reinforced Concrete Slabs Affected by Early-Age Loading and Low Temperature." ACI Str. J., 109(3), 413-422.
18. Puente, I., Azkune, M., and Insausti, A. (2007). "Shore-Slab Interaction in Multistory Reinforced Concrete Buildings during Construction: An Experimental Approach." Eng. Str., 29(5), 731-741.
19. Rosowsky, D., Stewart, M., and Khor, E. (2000). "Early -Age Loading and Long-Term Deflections of Reinforced Concrete Beams." ACI Str. J., 97(3), 517-524.
20. Stivaros, P. (2012). "Control of Deflection in Concrete Slabs and Effects of Construction Loads." ACI SP 284-17, 1-22.

Drying shrinkage cracking of concrete using dune sand and crushed sand

이의배
건축연구팀, 선임연구원
euibae.lee@daewooenc.com

본 논문은 2016년 Construction and Building Materials VOL.126, 517–526에 게재되었던 논문을 재게재한 것입니다.

Abstract

In this study, experimental results are presented to evaluate the properties of drying shrinkage cracking of concrete using dune sand (DS) and crushed sand (CS) as fine aggregate (FA). Concrete mixtures were made to meet the target workability with the variation of DS to FA ratio (DS/FA ratio) and water content. The results showed that the highest compressive strength and the highest tensile strength were shown in concrete mixtures of DS/FA ratio 20% and the strength decreased with the increase of DS/FA ratio when DS/FA ratio was over 20%. The lower water content led to higher net time-to-cracking. Also, the increase of DS led to decrease of CS and the increase of coarse aggregate (CA) in the mixture and this change led to decrease of the net time-to-cracking. It indicates that aggregate volume fraction could affect the drying shrinkage cracking under same total aggregate volume. Based on the changes of aggregate volume and the net time-to-cracking in this study, the restraint factor of CS could be calculated to minimum 54% of the restraint factor of CA and the restraint factor of DS could be less than that of CS.

Keywords : dune sand, crushed sand, drying shrinkage cracking, the net time-to-cracking, aggregate restraint

1_INTRODUCTION

In the Middle East and North Africa, dune sand (DS) is partially or wholly used as fine aggregate (FA) of concrete due to the scarcity of natural aggregate having satisfactory quality. The main purpose of the use of DS is the grading correction of crushed sand (CS) because CS has mostly coarser particles in the fine aggregate size range. Although the particle size of DS is different depending on the region, it is very fine, mostly in the range of 0.15~0.6mm, and its grading helps to correct poor grading of CS [1]. Also, the shape of DS particles is spherical and it can be beneficial to workability of concrete. But very fine particle size and large surface area of DS can make concrete cohesive and can lead to requirement of more water to meet suitable workability. Therefore, the important point for the use of DS is how much the replacement of DS can extract the optimum properties of concrete.

Several researches have been carried out to study the properties of DS concrete and optimum DS to FA ratio (DS/FA ratio) have been suggested [2-7]. The studies reported that use of DS improved the workability of the mix up to a certain limit and the limit was various with the characteristics of DS. However, there were different results in the mechanical properties of DS concrete; strength decreases with the increase of DS replacement [2-3] or maximum strength is achieved at a certain use of DS [4-5].

The suitability of the use of DS has been investigated focusing mainly on workability and strength as mentioned above. However, the region using DS as concrete fine aggregate generally has desert climate. This climate is characterized by strong sunlight,

high temperatures and dry air. These features of environment are the worst conditions in the drying shrinkage cracking of concrete. Therefore, the investigation of drying shrinkage is needed for DS concrete as well as the investigation for workability and strength. In this study, the drying shrinkage cracking of concrete using DS and CS was investigated. For this, concrete mixtures that can meet the target workability with variation of DS/FA ratio and water content were presented and their experimental results of drying shrinkage cracking were discussed.

2_EXPERIMENTAL PLAN AND METHODS

2.1. Experimental plan

Table 1 shows the experimental plan of this study. In concrete mix conditions, W/C ratio was 0.4 and target slump was 180±25mm. Two different water contents of 170kg/m^3 and 160kg/m^3 were set. As fine aggregate, DS and CS were mixed together with four DS/FA ratios; 10%, 20%, 40% and 60%. In order to evaluate mechanical properties of concrete, compressive strength and tensile strength were tested. Also, restrained drying shrinkage cracking was evaluated.

Table 1. Experimental plan

W/C	Slump (mm)	Cement type	Water content (kg/m^3)	DS/FA ratio[1] (%)	Tests
0.4	180±25	OPC	170 160	10 20 40 60	▪ Compressive strength ▪ Tensile strength ▪ Restrained drying shrinkage cracking

1) Volumetric replacement ratio in fine aggregate

2.2. Materials and mixture proportions

Table 2 shows the details of the materials. Ordinary Portland cement (OPC) was used as a binder. In aggregates, crushed aggregate with maximum size of 20mm was used as coarse aggregate and binary sand of CS and DS was used as fine aggregate. The appearances of CS and DS are presented in Fig.1 and Fig. 2. In particular, DS had rounded particle shape as shown in Fig. 3.

Table 2. Physical properties of materials

W/C	Physical properties
Cement	▪ Ordinary Portland cement (OPC) ▪ Density : 3.15g/cm^3 ▪ Fineness : 3,440cm^2/g
Coarse aggregate (CA)	▪ Crushed aggregate ▪ Max size : 20mm ▪ Density : 2.70g/cm^3 ▪ Absorption ratio : 0.77%
Crushed sand (CS)	▪ Max size : 5mm ▪ Density : 2.61g/cm^3 ▪ Fineness modulus. : 3.6 ▪ Absorption ratio : 1.53%
Dune sand (DS)	▪ Density : 2.61g/cm^3 ▪ Fineness modulus: 0.7 ▪ Absorption ratio : 1.19%
Admixture	▪ Naphthalene based ▪ Density : 1.23g/cm^3 ▪ pH : 6.79

Fig. 4 presents the particle size distribution of binary sand. Standard range of particle size distribution of fine aggregate is generally presented in KS F 2526 [8] (ASTM C 33 [9]). However, CS and DS did not meet the standard range of particle size distribution. Also, even if DS/FA ratio was changed 10% to 60%, the particle size distribution of binary sand did not meet the standard range. The fineness modulus of CS and DS were 3.6 and 0.7, respectively, and did not meet the limit value of 2.3~3.1 of KS 2526 (ASTM C 33). However, the fineness modulus of binary sands with DS/FA ratio

To select concrete mixtures, lab trial mixing tests were carried out. S/a ratio and admixture content were adjusted through trial



Fig. 1. Crushed sand (CS)

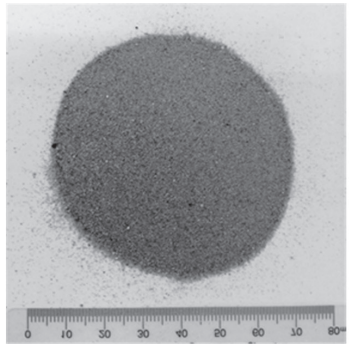


Fig. 2. Dune sand (DS)

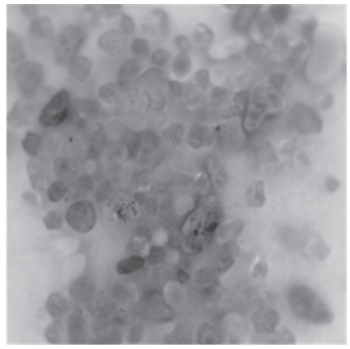


Fig. 3 Particle shape of DS

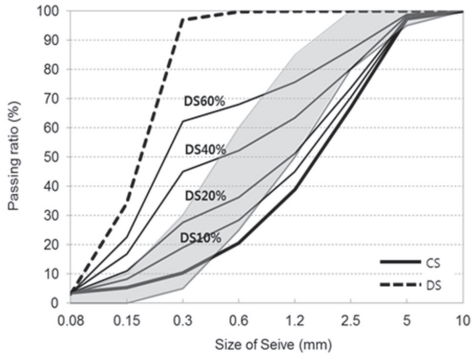


Fig. 4. Particle size distribution of sands

Table 3. Chemical composition of DS

Chemical	SiO_2	CaO	Al_2O_3	MgO	Fe_2O_3	K_2O
%	47.1	38.8	5.65	3.03	2.68	1.44

mixing to meet target slump. At the beginning of this study, there was an attempt to find a concrete mixture using only CS without DS. However, although fine aggregate ratio and admixture content were highly adjusted, its slump did not meet the target slump. DS replacement of minimum 10% was needed to meet the target slump. For this reason, the concrete mixture without DS was excluded in this study. Table 4 shows the selected concrete mixture proportions with variation of water content and DS/FA ratio.

2.3. Test methods

Compressive strength and split tensile strength were tested at ages of 3, 7, 14, 28 days according to KS F 2405 [10] (ASTM C 39 [11]) and KS F 2423 [12] (ASTM C 496 [13]).

To evaluate the properties of drying shrinkage cracking, restrained drying shrinkage test was conducted according to ASTM

Table 4. Concrete mixture proportions

Mixture ID[1]	Slump (mm)	W/C	S/a[2]	Unit weight (kg)					AD[8] (cw%)
				W[3]	C[4]	CS[5]	DS[6]	CA[7]	
W170–DS10	180 ±25	0.4	0.60	170	425	951	106	729	0.80
W170–DS20			0.50	170	425	705	176	911	0.80
W170–DS40			0.45	170	425	476	317	1002	0.70
W170–DS60			0.40	170	425	282	423	1094	0.80
W160–DS10			0.65	160	400	1058	118	655	1.00
W160–DS20			0.55	160	400	796	199	842	1.00
W160–DS40			0.45	160	400	488	326	1029	1.00
W160–DS60			0.42	160	400	304	456	1085	1.10

1) D10–W170 = DS/FA ratio 10% – water content 170kg/m^3
2) S/a : fine aggregate ratio, 3) W : water, 4) C : cement, 5) CS : crushed sand,
6) DS : dune sand, 7) CA : coarse aggregate 8) AD : chemical admixture

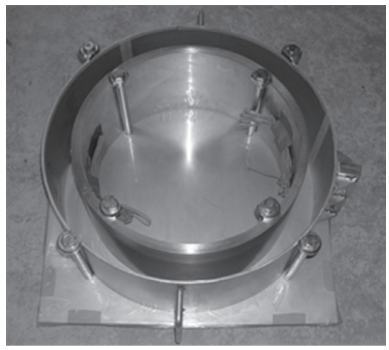


Fig. 5. Test apparatus

C 1581 [14]. Fig. 5 shows the test apparatus.

It was mainly composed of outer ring, inner ring and base plate and they were all manufactured by steel. To minimize the friction, the top of base plate was covered with two layers of polyethylene (PE) film. The thickness of the inner ring is 13mm and the outside diameter is 330mm. The inside diameter of outer ring is 405mm. The height of rings is 150mm. To make test specimen, coarse aggregate of size of over 13mm was removed from fresh concrete after mixing. The mold was filled with concrete in two layers and each layer was consolidated by steel rod. The test specimen was transferred to the testing room adjusted with temperature of 23±2℃ and relative humidity of 50±4%. Upon transfer of the test specimens, the bolts were immediately removed so the inner ring was not fixed to the base plate. After removal of bolts, the strain gages were connected to the data acquisition system and recoding data started at intervals of 20 minutes. The test specimen was covered with PE film to prevent drying. After curing of 24 hours, the PE film and outer ring were removed and drying of test specimen was started.

ASTM C 1581 suggests net time-to-cracking and stress rate to evaluate the cracking potential of concrete. The net time-to-cracking is the difference between the age at cracking and the drying was initiated and the age at cracking is determined when a sudden decrease in strain occurs. If there was no sudden decrease of strain, the net time-to-cracking was determined to the time when the shrinkage strain showed the maximum value and then slowly decreased in this study. The stress rate was calculated by Eq. (1) and Eq. (2). To calculate the strain rate factor in Eq. (1), regression analysis was conducted through the data, by using regression program of NLLEG.

$$\varepsilon_{net} = \alpha\sqrt{t} + k \quad (1)$$

Where, ε_{net} : net strain (m/m)
α : strain rate factor for each strain gage on the test specimen ((m/m)/day$^{1/2}$)
t : elapsed time (days)
k : regression constant

$$q = \frac{G|\alpha_{avg}|}{2\sqrt{t_r}} \quad (2)$$

Where, q : stress rate in each test specimen (MPa/day)
G : 72.2 GPa
|αavg| : absolute value of the average strain rate factor for each test specimen ((m/m)/day$^{1/2}$)
t_r : elapsed time at cracking (days)

Also, in this study, drying shrinkage stress was calculated by Eq. (3) [15].

$$\sigma_c(t) = \varepsilon_s E_s \frac{R_{IS}^2}{R_{OS}^2} \frac{(R_{OS}^2 - R_{IS}^2)}{(1+\upsilon_s)R_{OS}^2 + (1-\upsilon_s)R_{IS}^2} \frac{(R_{OC}^2 + R_{IC}^2)}{(R_{OC}^2 - R_{IC}^2)} \quad (3)$$

Where, σ : shrinkage stress of concrete (MPa)
ε_s : strain of steel ring (×10^{-6})
E_s : elastic modulus of steel ring (MPa)
υ_s : Poisson's ratio of steel ring
R_{IS} : inner diameter of steel ring (mm)
R_{OS} : outer diameter of steel ring (mm)
R_{IC} : inner diameter of concrete (mm)
R_{OC} : outer diameter of concrete (mm)

3_RESULTS ANALYSIS AND DISCUSSION

3.1. Compressive strength and tensile strength

The results of compressive strength and split tensile strength at measurement ages are presented in Table 5 and Table 6. Fig. 6

shows the compressive strength at age of 28 days. Test results of compressive strength were in the range of 44.7MPa to 53.8MPa. In W170 (Water content 170kg/m^3) mixtures, DS10(DS/FAratio10%) mixtures howed the compressive strength of 48.1MPa. DS20 mixture showed highest compressive strength which increased 10% than that of DS10 mixture. This increase could be due to the high compactness of aggregate[6]. However, compressive strength decreased with the increase of DS/FA ratio when DS/FA ratio was over 20%. The compressive strength of DS60 mixture decreased 7% in comparison with DS10 mixture. This decrease in strength could be attributed to the reduction of the bond strength between aggregate surface and cement paste. DS has rounded shape and smooth surface and the sephysical properties of DS can reduce the aggregate-paste bond strength[16].

The results for W160 mixtures showed the same manner with W170 mixtures. D20 mixture showed the highest compressive strength of 53.8MPa which was slightly higher than that of DS10 mixture. The results of compressive strength of DS40 and DS60 mixtures were lower than those of DS10 mixture.

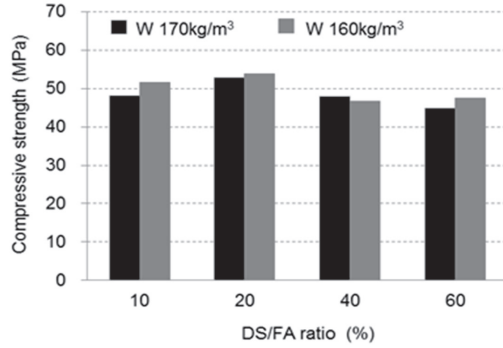


Fig. 6. Compressive strength at age 28 days

Table 5. Compressive strength

Mixture	Strength at ages (MPa)			
	3 days	7 days	14 days	28 days
W170–DS10	36.3	43.3	46.8	48.1
W170–DS20	37.7	43.9	47.7	52.9
W170–DS40	37.8	41.7	46.7	48.0
W170–DS60	33.4	40.1	42.6	44.7
W160–DS10	38.8	44.5	46.6	51.7
W160–DS20	38.9	45.3	48.9	53.8
W160–DS40	35.4	41.7	46.2	46.6
W160–DS60	35.5	41.8	44.5	47.6

Table 6. Split tensile strength

Mixture	Strength at ages (MPa)			
	3 days	7 days	14 days	28 days
W170–DS10	2.6	3.2	3.1	3.3
W170–DS20	2.3	2.9	3.0	3.4
W170–DS40	2.3	2.8	3.1	3.4
W170–DS60	2.6	2.6	2.7	2.8
W160–DS10	2.4	3.0	3.0	2.9
W160–DS20	2.3	2.7	3.0	3.7
W160–DS40	2.6	2.6	3.0	3.0
W160–DS60	2.3	2.7	2.8	3.1

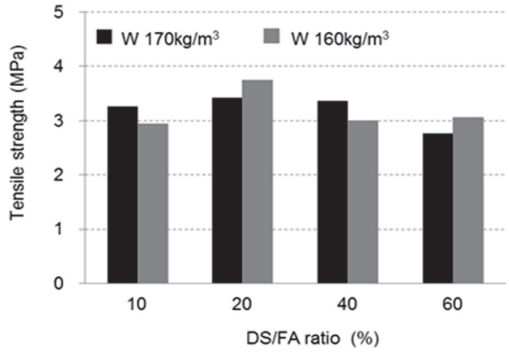
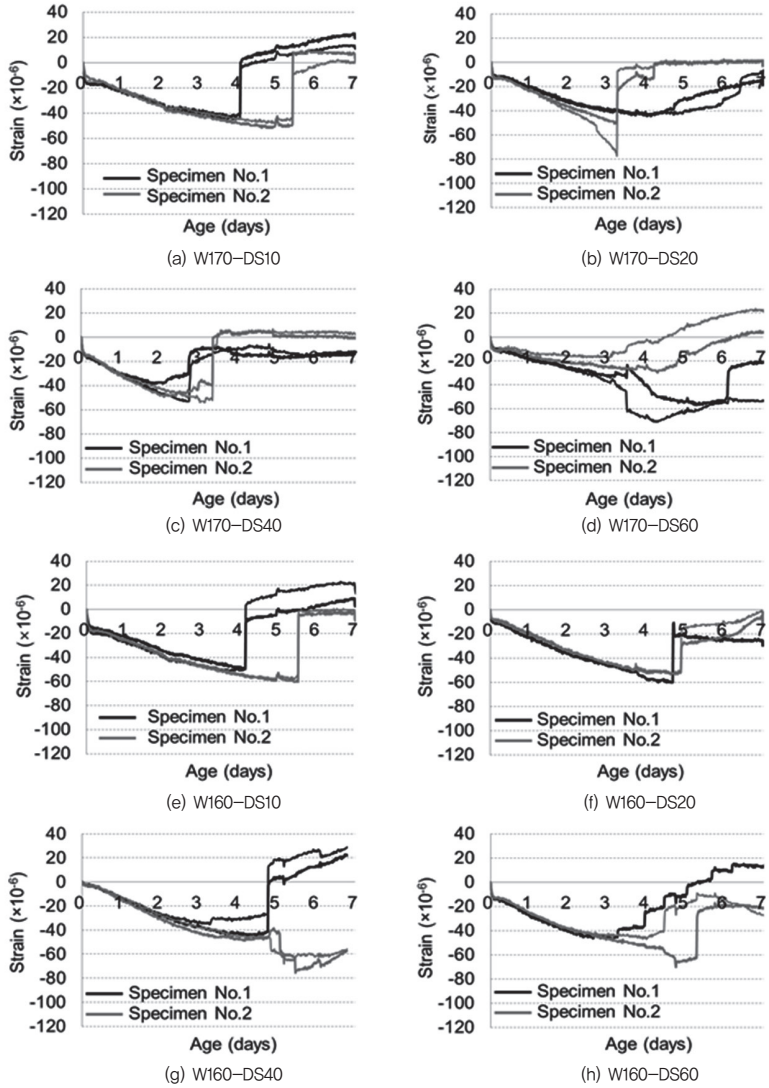


Fig. 7. Tensile strength at age 28 days

The tensile strength results at 28days are presented in Fig. 7. The results of tensile strength showed a similar tendency to the results of compressive strength. In W170 mixtures, the tensile strength of DS10 mixture was 3.3MPa. DS20 and DS40 mixtures showed the same tensile strength of 3.4MPa. When DS/FA ratio is 60%, the tensile strength decreased to 2.8MPa.

In W160 mixtures, DS20 mixture showed the highest tensile strength of 3.7MPa. The tensile strength of DS40 and DS60 mixtures were lower than that of DS20 mixture. The lowest tensile strength of 2.9MPa was observed in DS10 mixture.



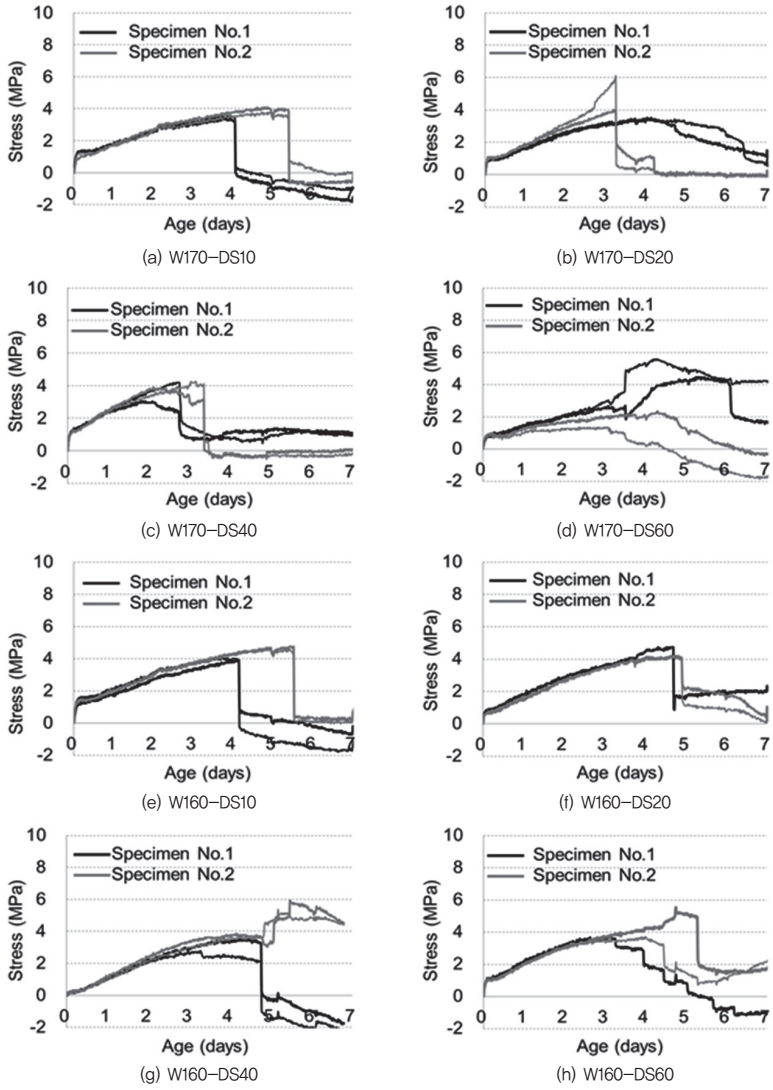
(a) W170–DS10 (b) W170–DS20

(c) W170–DS40 (d) W170–DS60

(e) W160–DS10 (f) W160–DS20

(g) W160–DS40 (h) W160–DS60

Fig. 8. Shrinkage of inner ring



(a) W170–DS10 (b) W170–DS20

(c) W170–DS40 (d) W170–DS60

(e) W160–DS10 (f) W160–DS20

(g) W160–DS40 (h) W160–DS60

Fig. 9. Shrinkage stress of concrete

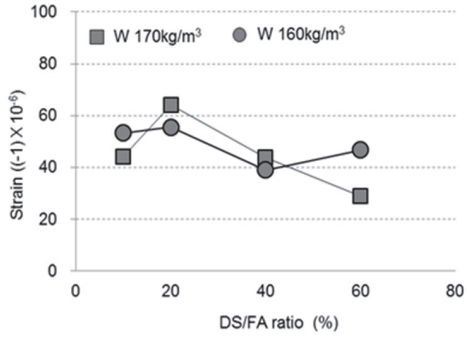


Fig. 10. Shrinkage strain at cracking

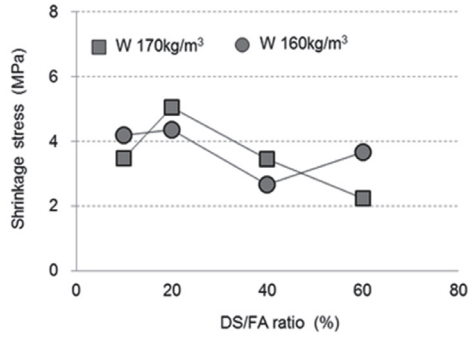


Fig. 11. Shrinkage stress at cracking

3.2. Restrained drying shrinkage cracking

Fig. 8 and Fig. 9 show the shrinkage strain of the inner ring and the shrinkage stress of concrete, respectively, after drying of test specimen.

(1) Strain and stress at cracking

Fig. 10 shows the measured strain of the inner ring just before cracking. Drying shrinkage cracking has averagely occurred at shrinkage strain of 47×10^{-6}.

In W170 mixtures, DS10 mixture showed shrinkage strain of 44×10^{-6}. The highest shrinkage strain was observed in DS20 mixture. The shrinkage strain decreased with the increase of DS/FA ratio when it was over 20%. DS40 and DS60 mixtures showed shrinkage strain of 44×10^{-6} and 29×10^{-6}, respectively.

W160 mixtures showed similar tendency with 170 mixtures, excepting for the result of DS60 mixture. DS20 mixture showed the highest shrinkage strain of 56×10^{-6}. However, the lowest shrinkage strain was shown in DS40 mixture.

The shrinkage stress just before cracking is presented in Fig. 11. It shows the same tendency as strain results because stress was calculated from measured shrinkage strain data of the inner ring as shown in Eq. (3). The calculated shrinkage stress was in range of 2.3MPa to 5.0MPa and average value was 3.6MPa. In W170 mixtures, DS20 mixture showed the highest shrinkage stress of 5.0MPa and the shrinkage stress decreased as DS/FA ratio increased when it was over 20%. In W160 mixtures, the highest shrinkage stress of 4.4MPa was observed in DS20 mixture and the lowest shrinkage stress of 2.7MPa was observed in DS40 mixture.

Fig. 12 presents the tensile strength development and shrinkage stress just before cracking of all mixtures. The tensile strength development was calculated from measured data of split tensile strength by Eq. (4) suggested in ACI 209 [17].

$$f_{ts}(t) = \left[\frac{t}{a+bt}\right] f_{ts}28 \qquad (4)$$

Where, f_{ts} : tensile strength at age t (MPa)

t : age (day)

f_{ts28} : tensile strength at age 28days (MPa)

a, b : constants

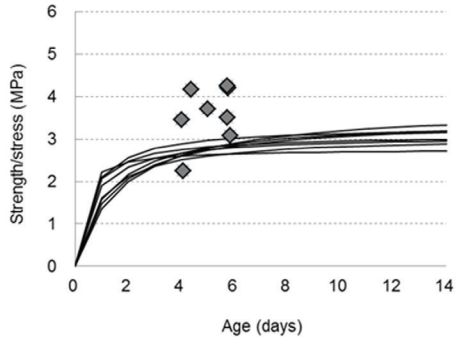


Fig. 12. Tensile strength development and shrinkage stress at cracking

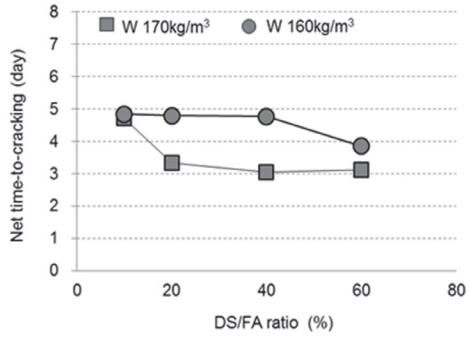


Fig. 13. Net time-to-cracking

As a result of comparison, almost drying shrinkage stress values were over the tensile strength when the cracking occurred. Shrinkage stress is not the only factor governing the cracking of restrained concrete. Cracking resistance of concrete under restrained shrinkage depends on the combined properties of shrinkage potential, shrinkage rate, tensile creep and tensile strength [18]. Therefore, it could be inaccurate to predict cracking based on a simple analysis of restrained shrinkage stress and tensile strength of concrete.

(2) Net time-to-cracking

Fig. 13 shows the net time-to-cracking of mixtures. The highest value of net time-to-cracking was 4.84days of D10-W160 mixture. D40-W170 mixture showed the lowest value of 3.06 days which was decreased by 37% compared to the value of D10-W160 mixture.

In W170 mixtures, the net time-to-cracking of D10 mixture was 4.73 days and the net time-to-cracking decreased as the DS/FA ratio increased up to 40%. However, when DS ratio was 60%, the net time-to-cracking very slightly increased more than that of DS40 mixture.

In W160 mixtures, the net time-to-cracking of D10 mixture was 4.84 days and the net time-to-cracking decreased as the DS/FA ratio increased.

(3) Stress rate

Fig. 14 shows the stress rate of mixtures. The highest value of stress rate was 0.55MPa/day of D20-W170 mixture. And D40-W170 mixture showed the lowest value of 0.31MPa/day which was decreased by 44% compared to the value of D20-W170 mixture.

In W170 mixtures, the stress rate of D10 mixture was 0.63MPa/day. A sharp increase of the stress rate was observed in D20 mixture and the stress rate was reduced as DS/FA ratio increased after DS/FA ratio of 20%. Also, a sharp decrease of the stress rate was shown in D60 mixture. However, W160 mixtures showed the narrow stress rate range of 0.42MPa/day-0.48MPa/day and waved result; the higher stress rate of D20 mixture than that of D10 mixture, the lower stress rate of D40 mixture than that of D20 mixture and the higher stress rate of D60 mixture than that of D40 mixture.

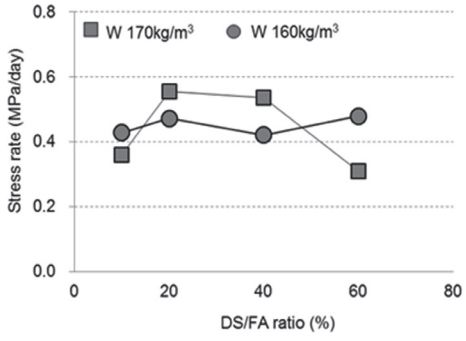


Fig. 14. Stress rate

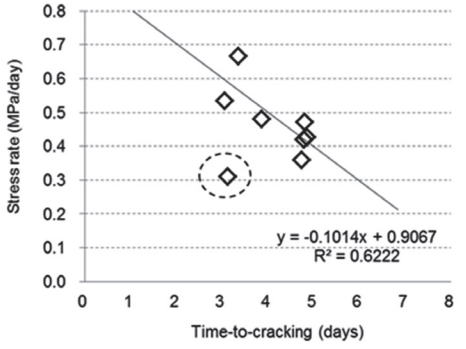


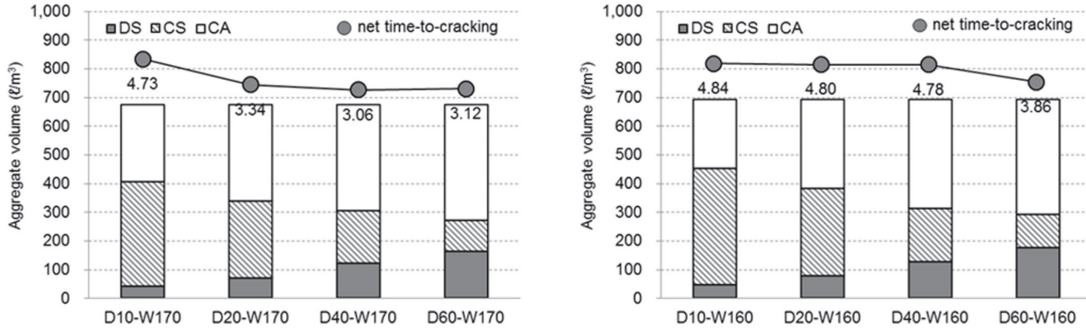
Fig. 15. Relationship between net time–to–cracking and stress rate

Fig. 15 shows the relationship between net time-to-cracking and stress rate. Excepting for the result of D60-W170, the inverse relationship could be observed; higher the net time-to-cracking, lower the stress rate.

(4) Restraint effect of DS and CS on drying shrinkage cracking

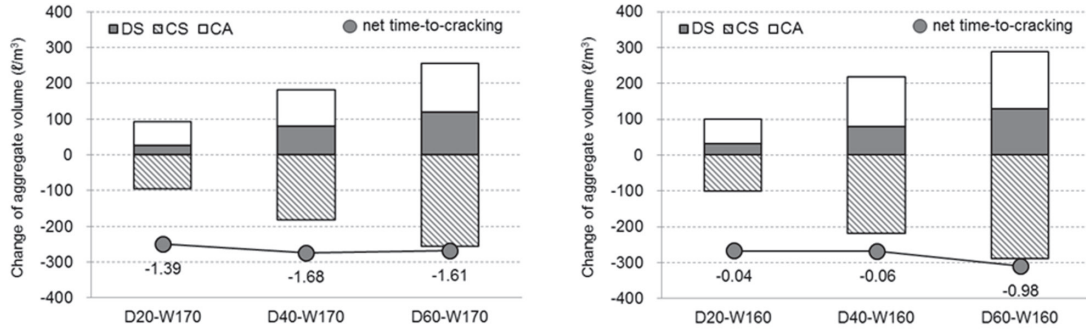
In mixture proportions, the increase of DS/FA ratio led to the decrease of CS and the increase of CA to meet the target workability of concrete in this study. These change led different results in drying shrinkage cracking. As mentioned above, net time-to-cracking and stress rate were suggested to evaluate the cracking potential of concrete in ASTM 1581. The effect of DS on drying shrinkage cracking was analyzed based on the result of the net time-to-cracking in this study. The aggregate volume with type and the net time-to-cracking at every mixture was compared and the Fig. 16 presents the results. This result generally shows that the decrease of CS, the increase of DS and the increase of CA lead to the decrease of the net time-to-cracking. Moreover, the change of aggregate volume and the change of the net time-to-cracking were compared as shown in Fig. 17 and the change meant the difference to the value of DS10 mixture. The greater change of the net time-to-cracking was shown in W170 mixtures compare to that of W160 mixtures; the change of the net time-to-cracking in W170 mixtures was in range of 1.39 days to 1.68 days, the change of the net time-to-cracking in W160 mixtures was in range of 0.04 day to 0.98 day.

It has been reported that the decrease of cement paste volume and the increase of aggregate volume can reduce the drying shrinkage cracking [19-22]. However, in conditions of same water-binder ratio and water content, all mixtures had the same volume of cement paste and aggregate volume in this study. There was only the change of aggregate volume fraction with aggregate



(a) W 170 mixtures (b) W 160 mixtures

Fig. 16. Aggregate volume fraction and net time–to–cracking



(a) W 170 mixtures (b) W 160 mixtures

Fig. 17. Change of aggregate volume and change of net time–to–cracking

types as shown in Fig. 16.

Aggregate composition could change the restraining of aggregate and it could affect inner structure and moisture movement [23]. DS has rounded shape and smooth surface. In contrast, CS and CA have angular shape and rough surface. These differences of shape and surface of aggregate could affect the bond strength between cement paste and aggregate and also could affect the restraint between cement paste and aggregate. Therefore, the increase of DS volume could lead the decrease of aggregate restraint and the increase of the volume of CS and CA can lead the increase of aggregate restraint. Moreover, the drying shrinkage decreases with increase in the size of aggregate and this is due to the restraining action of the larger size aggregate [21]. Therefore, it is easily considered that the increase of CA volume could lead to the decrease of drying shrinkage and the increase of net time-to-cracking. However, the result showed that, although CA volume increased, the net time-to-cracking decreased. It indicates that total decrease of restraint due to the increase of DS and the decrease of CS is larger than the increase of restraint due to the increase of CA.

Based on the result of Fig. 17, the effect of aggregate volume change on the net time-to-cracking could be presented as below Eq. (5)

$$\Delta TTC = a \cdot \Delta DS + b \cdot \Delta CS + c \cdot \Delta CA \quad (5)$$

Where, ΔTTC : change of time-to-cracking (day)
ΔDS : change of DS volume (kg/m³)
ΔCS : change of CS volume (kg/m³)
ΔCA : change of CA volume (kg/m³)
a : restraint factor of DS affecting the time-to-

cracking (day · m^3/kg)

b : restraint factor of CS affecting the time-to-cracking (day · m^3/kg)

c : restraint factor of CA affecting the time-to-cracking (day · m^3/kg)

Also, the comparison of restraint factors affecting the net time-to-cracking could be assumed as below.

$$0 < a < b < c$$

If the restraint factor of CA is 1 (c=1), the effect factors of DS and CS which satisfy above results and the assumption could be calculated as shown in Table 7.

This results show that the restraint factor of CS could be calculated to minimum 54% of the restraint factor of CA and restraint factor of DS could be less than that of CS. Also, the restraint factor of DS was calculated to be sharply decreased as the restraint factor of CS decreases.

Table 7. Analysis result of effect factor of aggregates

Mixture	Change of aggregate volume (kg/m^3)			Change of net time-to-cracking (day)	Effect factor of aggregates (day · m^3/kg)		
	CA	CS	DS		c	b	a
W170-DS20	67	-94	27	-1.39	1	0.74~0.99	0.04~0.91
W170-DS40	101	-182	81	-1.68	1	0.57~0.99	0.01~0.96
W170-DS60	135	-256	121	-1.61	1	0.54~0.99	0.01~0.96
W160-DS20	69	-100	31	-0.04	1	0.70~0.99	0.03~0.97
W160-DS40	139	-218	80	-0.06	1	0.64~0.99	0.01~0.97
W160-DS60	159	-289	130	-0.98	1	0.56~0.99	0.01~0.97

4_CONCLUSIONS

In this study, the drying shrinkage cracking of concrete using DS was investigated and the following conclusions can be drawn.

1) The highest values of compressive strength and tensile strength were shown in concrete mixtures with DS ratio 20% and the strength decreased with increase of DS ratio when DS ratio was over 20%. It could be due to the compactness of aggregate and the bond strength between aggregate surface and cement paste, which were affected by the change of DS ratio.

2) Drying shrinkage cracking by restrained test was averagely occurred at inner ring shrinkage strain of 47×10^{-6} and at shrinkage stress of 3.6MPa, in this study.

3) Almost drying shrinkage stress values just before cracking were higher than the tensile strength measured by the split tensile strength test. It means that prediction of cracking based on a simple analysis of restrained shrinkage stress and tensile strength of concrete could be inaccurate.

4) The lower water content of mixture led the higher net time-to-cracking. The net time-to-cracking decreased as DS ratio increased. Also, sharp decrease of the net time-to-cracking was shown at DS ratio 20% in W 170 mixtures and at DS ratio 60% in W 160 mixtures.

5) While the sharp increase or the sharp decrease of stress rate was shown in W170 mixtures, W160 mixtures showed similar stress rate. Also, excepting for the result of D60-W170, the stress rate showed the inverse relationship with the net time-to-cracking; higher the net time-to-cracking, lower the stress rate.

6) Aggregate volume fraction with type could affect the drying shrinkage cracking under same total aggregate volume. The increase of DS led the decrease of CS and the increase of CA in mixture and this change led the decrease of the net time-to-cracking due to the restraint reduction of DS.

7) The restraint factor of CS could be calculated to minimum 54% of the restraint factor of CA and the restraint factor of DS could be less than that of CS. Also, the calculation showed that the restraint factor of DS sharply decreases as the restraint factor of CS decreases.

REFERENCES

1. E. Lee and Y. Kim, Application and Characteristics of Dune Sand Concrete in the Middle East and North Africa, Magazine of the Korea Concrete Institute, 2014; 26(6):55-9.
2. A.S. Al-Harthy, R. Taha, The properties of concrete made with fine dune sand, Construction and Building Materials, 2007; 2: 1803–8.
3. E. S. A. Sief, Performance of Cement Mortar Made with Fine Aggregates of Dune Sand, Kharga Oasis, Western Desert, Egypt: An Experimental Study, Jordan Journal of Civil Engineering, 2013; 7(3): 270-84
4. A.Rmili,M.B.Ouezdou,M.Added,E.Ghorbel,Incorporation of CrusHed Sands and Tunisian Desert Sandsin the Composition of Self Compacting Concretes Part I: Study of Formulation, International Journal of Concrete Structures and Materials, 2009; 13(1): 3-9.
5. T. Bouziani, M. Bedrinas, M, Hadjoudja, Effect of Dune Sand on the Properties of Flowing sand-concrete, International Journal of Concrete Structures and Materials, 2012; 6(1): 59-64.
6. F. J. Luo, L. Heb, Z. Pan, W. H. Duan, X. L. Zhao, F. Collins, Effect of very fine particles on workability and strength of concrete made with dune sand, Construction and Building Materials, 2013; 47: 131-7.
7. B. Belhadj, M. Bederina, K. Benguettache, M. Queneudec, Effect of the type of sand on the fracture and mechanical properties of sand concrete, Advances in Concrete Construction, 2014; 1: 13-27
8. KS F 2526, Concrete aggregate, Korea Standards Association, 2007
9. ASTM C 33, Standard Specification for Concrete Aggregates, American Society for Testing and Materials, 2013
10. KS F 2405, Standard test method for compressive strength of concrete, Korea Standards Association, 2010
11. ASTM C 39, Standard Test Method for Compressive Strength of Cylindrical Concrete Specimens, American Society for Testing and Materials, 2009
12. KS F 2423, Method of test for splitting tensile strength of concrete, Korea Standards Association, 2006
13. ASTM C 496, Standard Test Method for Splitting Tensile Strength of Cylindrical Concrete Specimens, American Society for Testing and Materials, 2004
14. ASTM C 1581, Standard Test Method for Determining Age at Cracking and Induced Tensile Stress Characteristics of Mortar and Concrete under Restrained Shrinkage, American Society for Testing and Materials, 2009
15. G. Kim, H. Choi, E. Lee, J. Nam, M. Han, A study on the development of flat-ring type restrained test method and performance evaluation for evaluating shrinkage cracking properties of concrete in early age, Journal of Korea Institute for Structural maintenance Inspection, 2009; 13(3): 188-96
16. P. K. Mehta, P. J. M. Monteiro, CONCRETE - microstructure, properties and materials, Third Edition, McGraw-Hill, 2005: 56-7
17. ACI 209.1R Report on Factors Affecting Shrinkage and Creep Hardened Concrete, American concrete institute, 2005
18. H.T.. See, E.K. Attiogbe, and M.A. Miltenberger, Shrinkage cracking characteristics of concrete using ring specimens, ACI materials journal, 2003; 84(2): 239-245
19. J.A. Almudaiheem, W. Hansen, Effect of specimen size and shape on drying shrinkage of concrete, ACI materials journal, 1987; 100(3): 130-135
20. W. Hansen, J.A. Almudaiheem, Ultimate drying shrinkage of concrete - influence of major parameters, ACI materials journal, 1987; 84(3): 217-223
21. G.A. Rao, Long-term drying shrinkage of mortar – influence of silica fume and size of fine aggregate, Cement and Concrete Research, 2001; 31: 171-175
22. B. Bissonnette, P. Pierre, M. Pigeon, Influence of key parameters on drying shrinkage of cementitious materials, Cement and Concrete Research, 1999; 29: 1655-1662
23. A. M. Neville, Properties of concrete, Longman. 1995: 429, 438, 442

Effect of connection rotation capacities on seismic performance of IMF systems

Moon, Ki Hoon
Architectural Engineering Research Team, Senior Research Engineer
kihoon.moon@daewooenc.com

본 논문은 2016년 Earthquakes and Structures Vol.10, No.1, pp. 73-89에 게재되었던 논문을 재게재한 것입니다.

Abstract

The seismic performance of moment frames could vary according to the rotation capacity of their connections. The minimum rotation capacity of moment connections for steel intermediate moment frames (IMF) was defined as 0.02 radian in AISC 341-10. This study evaluated the seismic performance of IMF frames with connections having a rotation capacity of 0.02 radian. For this purpose, thirty IMFs were designed according to current seismic design provisions considering different design parameters such as the number of stories, span length, and seismic design categories. The procedure specified in FEMA P695 was used for conducting seismic performance evaluation. It was observed that the rotation capacity of 0.02 radian could not guarantee the satisfactory seismic performance of IMFs. This study also conducted seismic performance evaluation for IMFs with connections having the rotation capacity of 3% and ductile connections for proposing the minimum rotation capacity of IMF connections.

Keywords : rotation capacity; connections; intermediate moment frame; seismic performance; seismic design

1_INTRODUCTION

The rotation capacity of moment connections may significantly affect the seismic performance of moment frames. AISC 358-10 (2010) classifies moment frames into special, intermediate, and ordinary moment frames (SMF, IMF, OMF) according to their inelastic rotation capacities. AISC 341-10 (2010) requires minimum rotation capacities for SMFs and IMFs as 0.04 and 0.02 radian, respectively, whereas only minimal level of inelastic rotation is required for OMFs. SMFs are expected to produce deformation and energy dissipation capacities larger than IMFs and OMFs. For this reason, ASCE 7-10 (2010) assigns a response modification factor (R) as 8 for SMF, whereas factors for IMF and OMF are assigned as 4.5 and 3.5, respectively.

After the 1994 Northridge earthquake, numerous studies were conducted for evaluating the rotation capacities of moment connections (Luco and Cornell 1998a, Malley 1998, Stojadinovic et al. 2000, Sotirov et al. 2000). Those studies identified the cause of premature brittle fracture occurred in pre-Northridge moment connections, and developed new connections that avoid brittle connection fracture. In particular, many experimental researches were conducted for developing pre-qualified SMF connections (FEMA 350 2000, FEMA 355D 2000). The effect of ductile and brittle connections on the seismic response of moment frames

was investigated by Maison and Kasai (1997), Luco and Cornell (1998b, 2000), and Gupta and Krawinkler (1999). Most research has focused on evaluating the rotation capacity of SMF connections and the seismic performance of SMFs (Lee and Foutch, 2002; Jeong et al. 2015). Regarding the IMFs and OMFs, only limited research was conducted (Han et al. 2007, Han et al. 2015). Han et al. (2015) reported that the seismic performance of 20 story IMFs with reduced beam section-bolted shear tab (RBS-B) moment connections failed to meet the performance criteria specified in FEMA P695 (2009), which is a provision for collapse risk evaluation (Elkady and Lignos, 2015) .

AISC 341-10 states that the rotation capacity of 0.02 radian has been established based on engineering judgment applied to available tests and analytical studies, primarily those in FEMA 355C (2000) and 355F (2000). There was no study found so far, which evaluated the seismic performance of IMFs with respect to the rotation capacity of their connections.

In this study, the seismic performance evaluation was conducted according to FEMA P695 for IMFs with moment connections having different rotation capacities. For this purpose, IMFs with various numbers of stories and span lengths were designed for seismic design category (SDC) using design seismic forces determined according to ASCE 7-05 (2005) and ASCE 7-10. From the results of this study, the minimum rotation capacity for IMF connections was proposed.

2_CONNECTIONS FOR INTERMEDIATE STEEL MOMENT FRAMES

The In AISC 358-10, six prequalified moment connections are listed, which can be used as moment connections for SMFs and IMFs: (1) reduced beam section (RBS), (2) bolted unstiffened extended end plate (BUEEP), (3) bolted stiffened extended end plate (BSEEP), (4) bolted flange plate (BFP), (5) welded unreinforced flange-welded web (WUF-W), and (6) Kaiser bolted bracket (KBB). Among the pre-qualified moment connections, the RBS connections have been commonly used for seismic application. Many experimental researches were conducted for RBS connections, so that sufficient test results for the rotation capacity of RBS connections have been available.

The RBS connection can be classified into RBS-welded web connection and RBS-bolted web (RBS-B) connection. In this study, the rotation capacity of RBS-B connections, which are only valid for IMF connections (AISC 358-10), were estimated using test results (Tremblay et al. 1997; Engelhardt et al. 2000; Iwankiw and Carter, 1996; Lee et al. 2005; Chen et al. 1996; Anderson and Duan, 1998; Tsai and Chen, 1996; Han et al. 2009). Fig. 1 shows backbone curves for fracture-resistant and fracture-prone RBS-B connections, representing the relationship between the moment normalized by beam plastic moment (M/M_p) and total rotation (θ_t) measured at the connection. The fracture-resistant connection

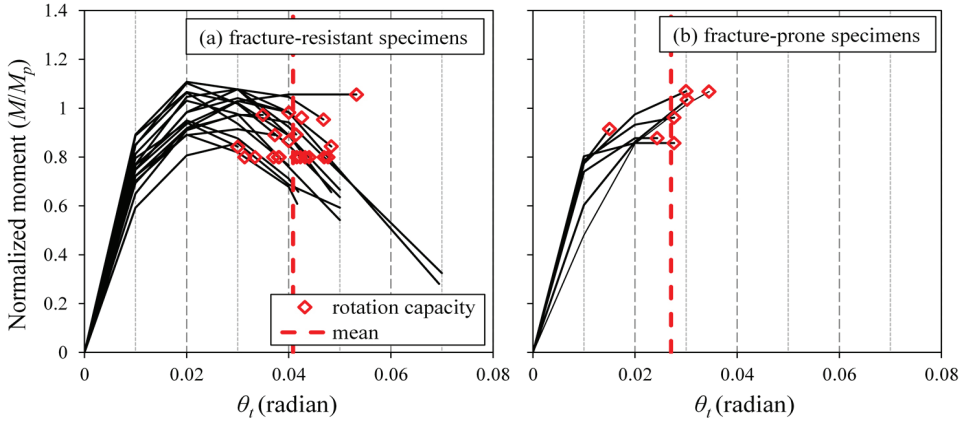


Fig. 1. Backbone curves of RBS-B connections

was defined as the connection that did not experience connection fracture until the completion of the test, whereas the fracture-prone connection experienced connection fracture during tests. As shown in Figs. 1(a)-(b), some connections behaved in a ductile manner, whereas other connections experienced premature fracture, resulting in a small rotation capacity. When premature brittle fracture occurs at the connection, the seismic performance of IMF systems could be significantly reduced.

No study can be found, which evaluated the seismic performance of code-complied IMFs with connection having the minimum rotation capacity of 0.02 radian that is required for IMF connections by AISC 341-10 as the minimum rotation capacity. This study evaluated the seismic performance of IMFs with their connections having the minimum rotation capacity (0.02 radian). Moreover, this study also considered connections with a rotation capacity of 0.03 radian as well as ductile connections (fracture resistant connection) because the rotation capacity of IMF connections varied as shown in Fig. 1. The seismic performance evaluation was conducted for IMFs with connections having different rotation capacities.

3_ANALYTICAL MODEL FOR MOMENT CONNECTIONS

For obtaining the reliable results from the seismic performance evaluation, the use of an accurate analytical model is very important. In this study, the IMF connection was modeled using OpenSees (Mazzoni et al. 2007) as shown in Fig. 2. The connection model was mainly based on 'M2' model developed by Gupta and Krawinkler (1999). As shown in Fig. 2, the actual dimension of the panel zone was precisely reflected in this model. 0.044SDSIe

The fiber section model was used for simulating the behavior of columns. In this model, the inelastic behavior of a member is predicted using the stress-strain relationship assigned for fiber sections. The interaction between axial force and moment can be accurately reflected using this model. For panel zones, rigid link elements were used along the perimeter of the panel zone. To simulate the tri-linear inelastic behavior of the panel zone, two rotational springs were installed at one corner of the panel zone (Fig. 2(b)), whereas pins were placed at the other three corners to connect the rigid link elements. The strength and stiffness of the two springs were determined based on Gupta and Krawinkler (1999).

The beam member was modeled using rigid element and inelastic rotational spring element that was placed at the ends of the beam (Fig. 2(c)). For fracture prone connections having rotation capacities of 0.02 and 0.03 radian, the rotational spring was modeled to drop its strength suddenly when the rotation of the spring reaches its rotation capacity. However, for ductile connections without connection fracture, the rotation spring was modeled based on Lignos (2014), which behaved in a ductile manner without a sudden strength drop.

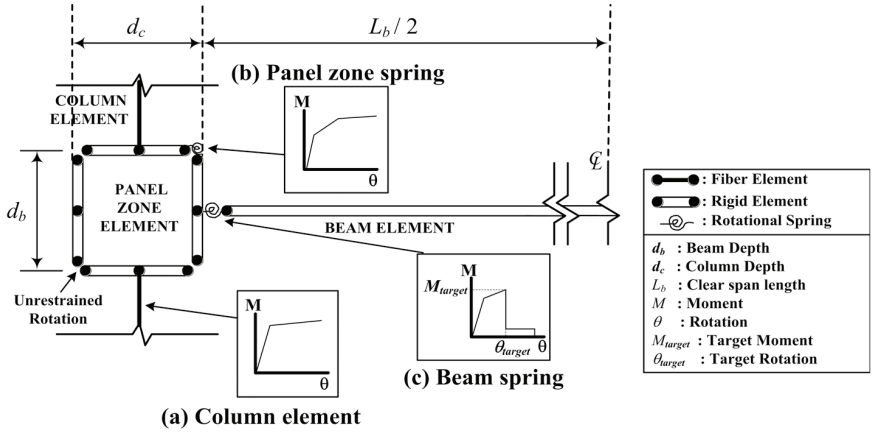


Fig. 2. Analytical model for IMF connections used in this study

4_MODEL FRAMES

For conducting seismic performance evaluation for IMFs, model frames were designed considering various important design parameters such as the number of stories, span length, seismic design category, and seismic response coefficient. To investigate the effect of the design parameter on the seismic performance of the IMF system, the model buildings with the same design parameters are grouped, which is named 'performance group.' (FEMA P695).

Since the higher mode contribution varies according to the number of stories, this study considered four different numbers of stories (3, 6, 9, and 20 stories). To account for the effect of gravity loads on beams, three different span lengths were included: 6.1m (20ft), 7.6m (25ft), and 9.1m (30ft).

Seismic design category (SDC) C was used for determining the design spectral acceleration parameters at short period (S_{DS}) and at 1-s period (S_{D1}) for model frames considering possible maximum and minimum seismic criteria of SDC: SDC Cmin(S_{DS}= 0.33g, S_{D1} = 0.133g) and SDC Cmax(S_{DS}= 0.50g, S_{D1} = 0.20g) where g is the gravitational acceleration. Since there is no height limitation on IMFs for SDC C (ASCE 7-10), high-rise buildings, which are strongly affected by higher mode contributions, can be designed.

The seismic response coefficient (C_s) was determined according to ASCE 7-05 and ASCE 7-10. The seismic base shear can be determined as C_s times the weight of the building (W). Both standards produced the same C_s in entire period range; however, they specify different minimum values of C_s, which may govern for long-period structures. ASCE 7-05 requires that seismic response coefficient C_s should be 0.01 or larger, whereas in ASCE 7-10, C_s should not be less than the smaller of 0.044 $S_{DS}I_e$ and 0.01g, where I_e is the importance factor. The values determined according to ASCE 7-05 and ASCE 7-10 were the same for 3-, 6- and 9-story model frames, whereas they were different for 20 story model frames because minimum values of C_s controlled for the 20 story frames (Fig. 3). Therefore, 3-, 6- and 9-story frames were designed using ASCE 7-10 design seismic forces, whereas 20-story frames were designed for design seismic forces determined according to ASCE 7-05 and ASCE 7-10.

Considering all design parameters as mentioned above, twenty four IMFs were designed, which were summarized in Table 1. The frames were classified into 6 performance groups according to span length (6.1, 7.6, and 9.1m) and seismic design categories (SDC Cmin and SDC Cmax).To investigate the effect of different design seismic forces determined from ASCE7-05 and ASCE7-10 on the seismic performance of IMFs, six 20-story model frames were designed, which were grouped as an additional performance group. Thus, this study considered a total of thirty IMFs and seven performance groups.

To investigate the effect of connection rotation capacity on the seismic performance of IMFs, moment connections were modeled using rotational spring element with three different rotation capacities: (1) 2%, (2) 3%, and (3) ductile connection. For connections with rotation capacities of 2% and 3%, the rotational

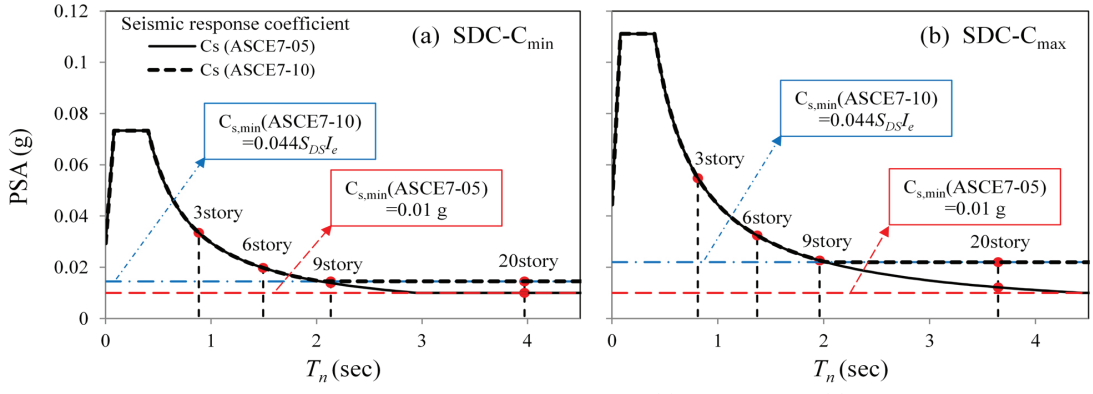


Fig. 3. Seismic response coefficient of model frames for (a) SDC Cmin and (b) SDC Cmax

spring element was forced to fracture at rotations of 2% and 3%, respectively. The ductile connection was modeled with a ductile spring element without fracture. Since three different connection models for each model frame were used, the number of model frames used for performance evaluation were 90 (=30x3). In Table 1, frame ID 'MIN6-10-2%' represents the IMF with a span length of 6.1 m and a connection rotation capacity of 2%, which were designed for seismic loads for SDC Cmin according to ASCE7-10 design seismic forces.

The model frames were assumed to be used in office buildings located at a site with soil condition D (ASCE 7-10). Fig. 4 shows floor plans and elevations for the model frames. As seen in Fig. 4, the seismic resistance for buildings was provided by perimeter frames. Steel material ASTM A992/A992M was used for beams and columns. According to ASCE 7-10, for IMFs, the response modification factor (R), overstrength factor (Ω), and deflection amplification factor (C_d) are 4.5, 3.0, and 4.0, respectively.

Table 1. Summary of model frames and performance groups

No.	Performace Group	No.	Arch.ID	Design Load (ASCE 7)	Bay Size	No. Of Stories	Seismic Design Criteria				
							SDC	Mass (ton)	T_n^* (sec)	T_1^* (sec)	C_s^+ (g)
1	Min6-10-x^{++}%	1	3CMIN10-6.1	2005/2010	6.1m (20ft)	3	Cmin	582	0.858	1.479	0.0345
		2	6CMIN10-6.1			6		1,188	1.493	2.084	0.0198
		3	9CMIN10-6.1			9		1,902	2.135	2.893	0.0138
		4	20CMIN10-6.1	2010		20		5,223	3.972	3.804	0.0145
2	Max6-10-x%	5	3CMAX10-6.1	2005/2010		3	Cmax	582	0.787	1.160	0.0565
		6	6CMAX10-6.1			6		1,191	1.371	1.914	0.0324
		7	9CMAX10-6.1			9		1,902	1.960	2.658	0.0227
		8	20CMAX10-6.1	2010		20		5,236	3.646	3.577	0.0220
3	Min7-10-x%	9	3CMIN10-7.6	2005/2010	7.6m (25ft)	3	Cmin	910	0.858	1.522	0.0345
		10	6CMIN10-7.6			6		1,849	1.493	2.125	0.0198
		11	9CMIN10-7.6			9		2,944	2.135	2.658	0.0138
		12	20CMIN10-7.6	2010		20		8,171	3.972	3.540	0.0145
4	Max7-10-x%	13	3CMAX10-7.6	2005/2010		3	Cmax	918	0.787	1.155	0.0565
		14	6CMAX10-7.6			6		1,853	1.371	1.920	0.0324
		15	9CMAX10-7.6			9		2,951	1.960	2.625	0.0227
		16	20CMAX10-7.6	2010		20		8,194	3.646	3.406	0.0220
5	Min9-10-X%	17	3CMIN10-9.1	2005/2010	9.1m (30ft)	3	Cmin	1,318	0.858	1.524	0.0345
		18	6CMIN10-9.1			6		2,680	1.493	2.159	0.0198
		19	9CMIN10-9.1			9		4,293	2.135	2.587	0.0138
		20	20CMIN10-9.1	2010		20		11,933	3.972	3.570	0.0145
6	Max9-10-X%	21	3CMAX10-9.1	2005/2010		3	Cmax	1,329	0.787	1.162	0.0565
		22	6CMAX10-9.1			6		2,686	1.371	1.916	0.0324
		23	9CMAX10-9.1			9		4,297	1.960	2.539	0.0227
		24	20CMAX10-9.1	2010		20		11,981	3.646	3.570	0.0220
7	20F-05-x%	25	20CMIN10-6.1	2005	6.1m (20ft)	20	Cmin	5,284	3.972	3.600	0.0100
		26	20CMAX10-6.1			20	Cmax	5,182	3.646	3.742	0.0122
		27	20CMIN10-7.6		7.6m (25ft)	20	Cmin	8,168	3.972	3.547	0.0100
		28	20CMAX10-7.6			20	Cmax	8,172	3.646	3.526	0.0122
		29	20CMIN10-9.1		9.1m (30ft)	20	Cmin	11,930	3.972	3.576	0.0100
		30	20CMAX10-9.1			20	Cmax	11,934	3.646	3.672	0.0122

* T_n^* : Fundamental period(= $C_u T_a$), T_1^{**} : 1st mode period, C_s^+ : Seismic response coefficient,
x^{++}% : connection rotation capacity (2%, 3% radian, and ductile)

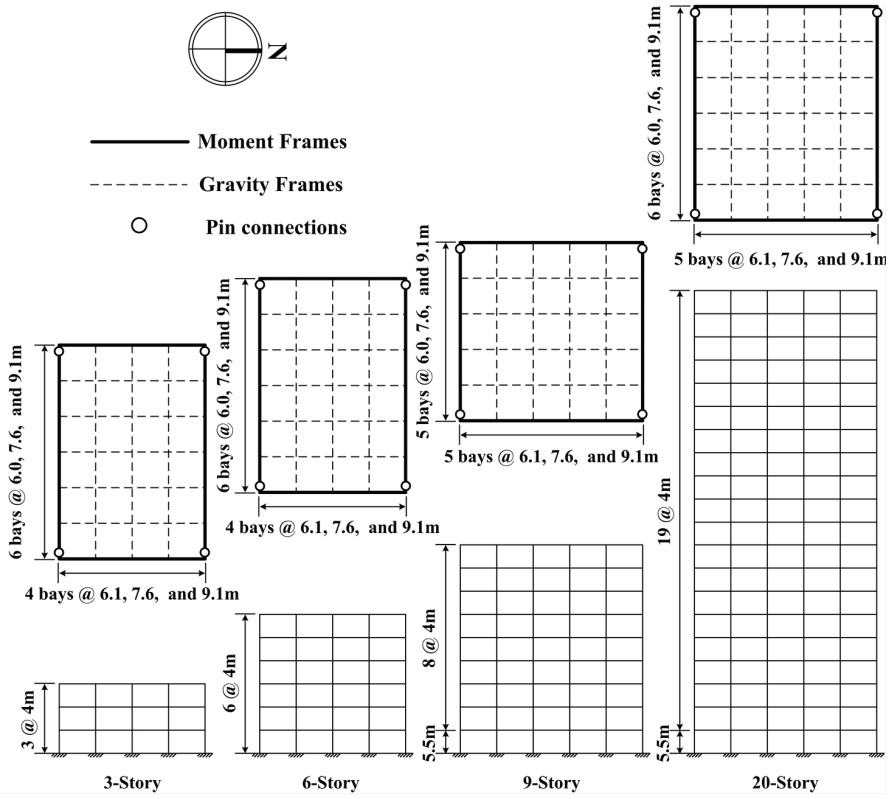


Fig. 4. Floor plans and elevations of model buildings

Members were designed according to AISC 341-10 and AISC 360-10 (2010). The dead load and live load for member deign were assumed as 4.12 kPa (86 lb/ft2) and 0.96 kPa (20 lb/ft2), respectively. The basic wind speed of 51 m/sec was used, and surface roughness was assumed as B for urban office buildings [Chapters 26 and 27 in ASCE 7-10]. Fig. 3 shows the seismic design coefficient for SDC Cmin and SDC Cmax determined according to ASCE7-05 and ASCE7-10. As mentioned earlier, two dimensional analytical model was used for analysis, which can account for P - Δ effect using an additional dummy column.

5_SEISMIC PERFORMANCE EVALUATION

Seismic performance evaluation was conducted according to FEMA P695, which is a provision for evaluating collapse risk. The collapse is defined as global dynamic instability (Adam and Jäger, 2012; Qi et al. 2012; Eads et al. 2013; Hamidia et al. 2014). Acceptable performance is defined by two collapse prevention objectives: (1) the probability of collapse for maximum considered earthquake (MCE) ground motions is 10% or less on average across a performance group, and (2) the probability of collapse for MCE ground motions is 20% or less for each frame within a performance group. Acceptable performance is achieved when adjusted collapse margin rations, *ACMR*, for each model frame and performance group, meet the following two criteria: (1) The average value ($\overline{ACMR_i}$) of for each performance group exceeds $ACMR_{10\%}$, and (2) individual values ($ACMR_i$) of *ACMR* for each model frame within a performance group exceeds $ACMR_{20\%}$, where $ACMR_{10\%}$ and $ACMR_{20\%}$ are the limiting values of *ACMR* corresponding to the probabilities of collapse of 10% and 20% for MCE ground motions, respectively. The procedure for estimating $ACMR_i$ and $\overline{ACMR_i}$ is summarized as follows. Fig.

5 illustrates the procedure.

(1) Conduct a static pushover analysis, and determine the overstrength factor (Ω) and period dependent ductility factor (μ_T) using Eqs. (1)-(2). (Fig. 5(a))

$$\Omega = V_{\max} / V_T \quad (1)$$

$$\mu_T = \delta_u / \delta_{y,eff} \quad (2)$$

where $V_{\max}$ is the maximum base shear force, V_d is the design base shear force, δ_u is the ultimate roof displacement defined in Fig. 5(a), and $\delta_{y,eff}$ is the effective yield roof displacement.

(2) Conduct incremental dynamic analyses (IDA), and determine the median collapse strength ($\widehat{S_{CT}}$) and collapse margin ratio (*CMR*) using Eq. (3) (Fig. 5(b)).

$$CMR = \widehat{S_{CT}} / S_{MT} \quad (3)$$

where S_{MT} is the 5% damped pseudo spectral acceleration at T_n for the MCE ground motions.

(3) To account for the effect of the spectral shape of ground motions used for performance evaluation, the spectral shape factor (*SSF*) is calculated (Fig. 5(c)), which is the function of μ_T, T_n and the level of SDC.

(4) Calculate $ACMR_i$ for each model frame using Eq. (4). Then, the average value of $ACMR_i$ for model frames within each performance group is calculated ($\overline{ACMR_i}$).

$$ACMR_i = CMR \times SSF \quad (4)$$

(5) Find the acceptable values $ACMR_{10\%}$ and $ACMR_{20\%}$ from the Table provided in FEMA P695 (Table 7-3).

(6) Check whether acceptance criteria are met using Eqs. (5)-(6). (Fig. 5(d))

$$\overline{ACMR_i} \geq ACMR_{10\%} \quad (5)$$

$$ACMR_i \geq ACMR_{20\%} \quad (6)$$

6_SEISMIC PERFORMANCE OF IMFS WITH CONNECTIONS HAVING A ROTATION CAPACITY OF 2%

Seismic performance evaluation was conducted for thirty IMFs.

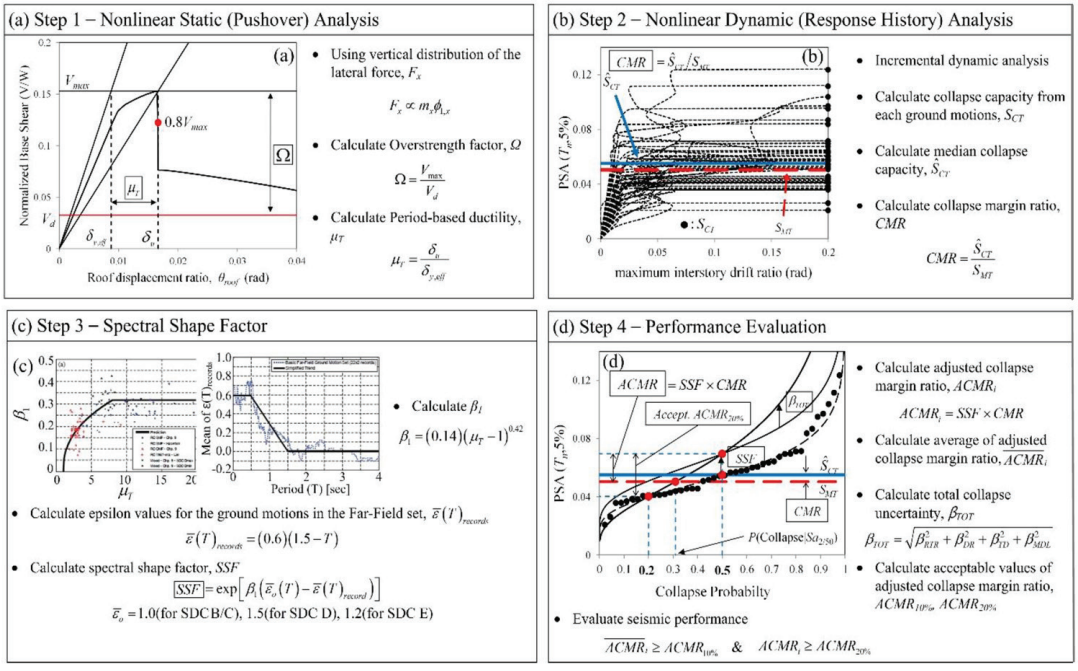


Fig. 5. The summarized procedure for seismic performance evaluation in FEMA P695

The rotation capacity of IMFs was assumed as 0.02 radian, which is defined as the minimum rotation capacity for IMF in AISC 341-10. Table 2 summarizes the results of the performance evaluation conducted according to FEMA P695 procedure. As seen in this table, twelve frames and one performance group did not meet the criteria specified in FEMA P695.

To investigate the vulnerability of IMFs, the probability of collapse for MCE ground motions ($P(Collapse|S_{MT})$) was calculated. Fig. 6 shows the collapse probabilities according to design parameters.

The collapse probability varied significantly according to the number of stories as well as design seismic forces determined

Table 2. Summary of collapse margin parameters and acceptance check for IMF systems with connections having a rotation capacity of 0.02 radian

Performance group	Arch.ID	Computed overstrength and collapse margin parameters							Acceptance check		
		S_{MT}	Ω	μ_T	S_{CT}	*CMR*	*SSF*	*ACMR*	β_{TOT}	Accept. *ACMR*	Pass /Fail
Min6–10–2%	3CMIN10–6.1	0.233	4.99	2.00	1.158	4.96	1.09	5.41	0.68	1.77	Pass
	6CMIN10–6.1	0.134	6.11	1.97	0.382	2.85	1.15	3.27	0.68	1.76	Pass
	9CMIN10–6.1	0.094	8.98	1.55	0.243	2.60	1.11	2.89	0.66	1.74	Pass
	20CMIN10–6.1	0.050	4.34	3.15	0.137	2.73	1.21	3.31	0.73	1.84	Pass
	Average		6.11	2.17		3.28		3.72	0.68	2.40	Pass
Max6–10–2%	3CMAX10–6.1	0.381	4.57	2.20	1.624	4.26	1.09	4.65	0.69	1.78	Pass
	6CMAX10–6.1	0.219	4.71	2.37	0.841	3.84	1.16	4.46	0.69	1.79	Pass
	9CMAX10–6.1	0.153	5.55	1.95	0.265	1.73	1.15	1.99	0.67	1.76	Pass
	20CMAX10–6.1	0.082	5.32	2.14	0.113	1.38	1.16	1.60	0.68	1.78	Fail
	Average		5.04	2.17		2.80		3.17	0.68	2.40	Pass
Min7–10–2%	3CMIN10–7.6	0.233	4.87	2.05	1.196	5.13	1.09	5.60	0.68	1.77	Pass
	6CMIN10–7.6	0.134	6.12	2.14	0.387	2.89	1.16	3.35	0.68	1.78	Pass
	9CMIN10–7.6	0.094	8.61	1.61	0.178	1.90	1.12	2.13	0.66	1.74	Pass
	20CMIN10–7.6	0.050	6.28	1.46	0.069	1.36	1.11	1.51	0.65	1.73	Fail
	Average		6.47	1.82		2.82		3.15	0.67	2.36	Pass
Max7–10–2%	3CMAX10–7.6	0.381	4.88	2.11	1.941	5.09	1.09	5.54	0.68	1.77	Pass
	6CMAX10–7.6	0.219	4.99	2.40	0.921	4.21	1.16	4.88	0.70	1.80	Pass
	9CMAX10–7.6	0.153	5.53	1.78	0.236	1.54	1.13	1.75	0.67	1.75	Fail
	20CMAX10–7.6	0.082	5.38	1.82	0.108	1.31	1.14	1.49	0.67	1.76	Fail
	Average		5.20	2.03		3.04		3.42	0.68	2.38	Pass
Min9–10–2%	3CMIN10–9.1	0.233	4.85	2.03	1.186	5.08	1.09	5.55	0.68	1.77	Pass
	6CMIN10–9.1	0.134	6.25	1.93	0.426	3.18	1.14	3.64	0.67	1.76	Pass
	9CMIN10–9.1	0.094	8.97	2.15	0.194	2.07	1.16	2.40	0.68	1.78	Pass
	20CMIN10–9.1	0.050	7.36	1.46	0.067	1.32	1.11	1.46	0.65	1.73	Fail
	Average		6.86	1.89		2.91		3.26	0.67	2.37	Pass
Max9–10–2%	3CMAX10–9.1	0.381	4.82	2.09	1.653	4.34	1.09	4.71	0.68	1.77	Pass
	6CMAX10–9.1	0.219	5.08	2.26	0.923	4.22	1.15	4.87	0.69	1.79	Pass
	9CMAX10–9.1	0.153	6.32	1.98	0.225	1.47	1.15	1.69	0.68	1.77	Fail
	20CMAX10–9.1	0.082	4.76	1.81	0.121	1.48	1.14	1.68	0.67	1.75	Fail
	Average		5.25	2.04		2.87		3.24	0.68	2.38	Pass
20F–05–2%	20CMIN05–6.1	0.050	9.10	1.94	0.096	1.90	1.15	2.17	0.67	1.76	Pass
	20CMAX05–6.1	0.082	8.40	1.66	0.082	0.99	1.12	1.12	0.66	1.75	Fail
	20CMIN05–7.6	0.050	8.82	1.44	0.061	1.20	1.10	1.33	0.65	1.73	Fail
	20CMAX05–7.6	0.082	7.26	1.68	0.073	0.88	1.13	0.99	0.66	1.75	Fail
	20CMIN05–9.1	0.050	10.38	1.43	0.059	1.17	1.10	1.29	0.65	1.73	Fail
	20CMAX05–9.1	0.082	7.73	2.07	0.074	0.90	1.15	1.04	0.68	1.77	Fail
	Average		8.61	1.71		1.17		1.32	0.66	2.34	Fail

from ASCE 7-05 and ASCE 7-10. With an increase in the number of stories, the collapse probability becomes larger (Fig. 6(a)). The average values for the collapse probabilities of 3-, 6-, 9-, and 20-story frames were 0.008, 0.024, 0.1423, and 0.2972, respectively. All 3- and 6-story model frames had the probability of collapse less than 20%, which satisfied the FEMA P695 criteria, whereas some of 9- and 20-story model frames did not satisfy the criteria. In particular, ten 20-story frames did not meet the criteria among twelve 20-story model frames (Table 2).

Fig. 6(d) shows that the numbers of 20-story frames, which did not meet the criteria, were the same, regardless of ASCE 7-05 and ASCE 7-10 design seismic forces. However, the average collapse probability (=0.223) of the 20-story frames designed using the ASCE 7-10 design seismic force is smaller than that (=0.370) of the frames designed using the ASCE 7-05 design seismic force.

As shown in Fig. 6(b)-(c), the collapse probability did not vary significantly according to span length and the level of SDC. The average values of the collapse probabilities of IMFs having span lengths 6.1, 7.6 and 9.1m were 0.114, 0.177, and 0.170, respectively.

Regarding the level of SDC, the number of the frames with unsatisfactory seismic performance became larger with increasing the level of SDC from SDC Cmin to SDC Cmax (Fig.6(c)).The average collapse probabilities of the frames designed for SDC Cmin and Cmax were 0.120 and 0.187, respectively.

7_SEISMIC PERFORMANCE OF IMFS ACCORDING TO DIFFERENT ROTATION CAPACITIES OF CONNECTIONS

This study evaluated the effect of connection rotation capacities on the seismic performance of IMFs. This study considered IMF connections fractured at rotations of 0.02 and 0.03 radian (connection rotation capacity) as well as ductile connection without fracture. Figs. 7-8 shows the collapse probabilities of IMFs for

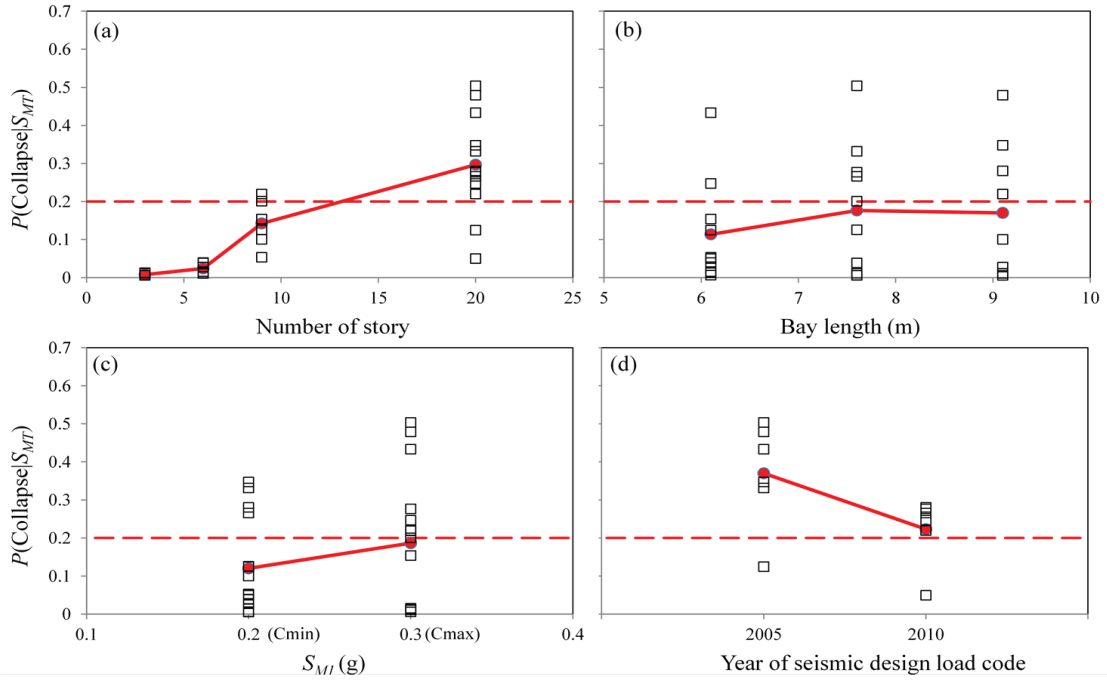


Fig. 6. Seismic response coefficient of model frames for (a) SDC Cmin and (b) SDC Cmax

MCE ground motions with respect to different rotation capacities of their connections. Since 3- and 6- story frames with connections having a rotation capacity of 0.02 radian, satisfied the FEMA P695 criteria, those frames were not included in Figs. 7-8. Tables 3-4 summarize the results of seismic performance evaluation for IMFs with connections having a rotation capacity of 0.03 radian and ductile capacity, respectively.

As shown in Fig. 7(a), all 9 story IMFs designed for SDC Cmin using ASCE7-10 design seismic forces satisfied the FEMA P695 criteria irrespective of the ir rotation capacities. The IMFs designed for SDC Cmax with a span length of 6.1m satisfied the seismic performance criteria when their connections had a rota-

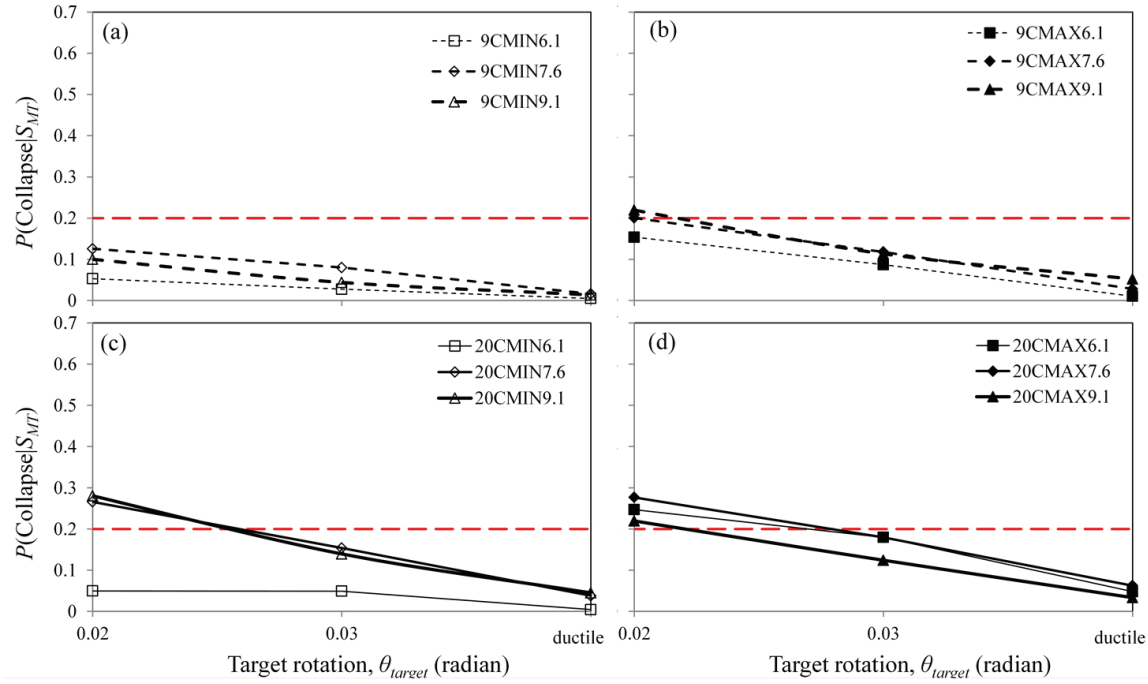


Fig. 7. Probability of collapse for MCE earthquake with response to rotation capacity for each building designed by ASCE7–10 seismic load

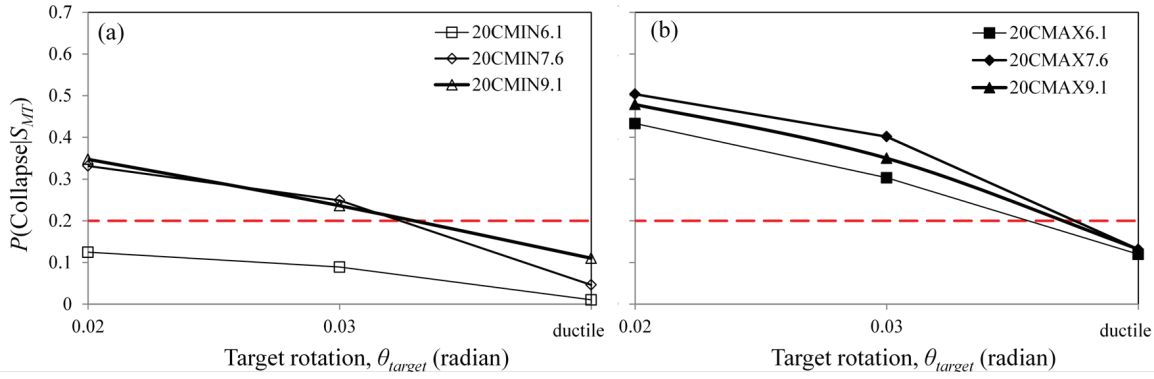


Fig. 8. Probability of collapse for MCE earthquake with response to rotation capacity for 20–story building designed by ASCE7–05 seismic load

tion capacity of 0.02 radian or larger, whereas the frames with span lengths of 7.6 and 9.1 m met the criteria only when their connections had a rotation capacity of 0.03 radian or larger (Fig.7(b)).

Fig. 7(c) shows that 20 story frames with a span length of 6.1m designed for SDC Cmin satisfied the FEMA P695 criteria when their connections had a rotation capacity of 0.02 radian or larger. However ,the frames with span lengths of 7.6 and 9.1 m met the criteria only when their connections had a rotation capacity as large as 0.03 radian. As shown in Fig.7(d), 20 story frames designed for SDC Cmax did not satisfied the criteria when their

Table 3. Summary of collapse margin parameters and acceptance check for IMF systems with connections having a rotation capacity of 0.03 radian

Performance group	Arch.ID	Computed overstrength and collapse margin parameters							Acceptance check		
		S_{MT}	Ω	μ_T	S_{CT}	*CMR*	*SSF*	*ACMR*	β_{TOT}	Accept. *ACMR*	Pass /Fail
Min6–10–3%	3CMIN10–6.1	0.233	5.06	2.76	1.394	5.98	1.12	6.66	0.71	1.82	Pass
	6CMIN10–6.1	0.134	6.27	2.60	0.434	3.24	1.19	3.84	0.70	1.81	Pass
	9CMIN10–6.1	0.094	9.13	1.99	0.298	3.18	1.15	3.65	0.68	1.77	Pass
	20CMIN10–6.1	0.050	4.56	3.50	0.136	2.71	1.23	3.32	0.73	1.84	Pass
	Average		6.26	2.71		3.77		4.37	0.71	2.47	Pass
Max6–10–3%	3CMAX10–6.1	0.381	4.69	3.05	1.919	5.04	1.11	5.61	0.73	1.84	Pass
	6CMAX10–6.1	0.219	4.75	3.11	0.964	4.40	1.19	5.25	0.73	1.84	Pass
	9CMAX10–6.1	0.153	5.64	2.64	0.337	2.20	1.19	2.62	0.71	1.81	Pass
	20CMAX10–6.1	0.082	5.34	2.49	0.132	1.61	1.18	1.90	0.70	1.80	Pass
	Average		5.11	2.82		3.31		3.84	0.71	2.50	Pass
Min7–10–3%	3CMIN10–7.6	0.233	4.90	2.86	1.403	6.01	1.12	6.73	0.72	1.83	Pass
	6CMIN10–7.6	0.134	6.35	2.78	0.446	3.33	1.19	3.98	0.71	1.82	Pass
	9CMIN10–7.6	0.094	8.82	1.96	0.210	2.25	1.15	2.58	0.67	1.76	Pass
	20CMIN10–7.6	0.050	6.42	1.81	0.088	1.74	1.14	1.98	0.67	1.75	Pass
	Average		6.62	2.35		3.33		3.81	0.69	2.43	Pass
Max7–10–3%	3CMAX10–7.6	0.381	4.94	2.98	2.455	6.44	1.11	7.17	0.73	1.84	Pass
	6CMAX10–7.6	0.219	5.04	3.12	1.061	4.85	1.19	5.79	0.73	1.84	Pass
	9CMAX10–7.6	0.153	5.70	2.37	0.297	1.94	1.17	2.28	0.69	1.79	Pass
	20CMAX10–7.6	0.082	5.47	2.20	0.133	1.61	1.16	1.88	0.69	1.78	Pass
	Average		5.29	2.67		3.71		4.28	0.71	2.48	Pass
Min9–10–3%	3CMIN10–9.1	0.233	4.92	2.82	1.459	6.25	1.12	6.99	0.72	1.83	Pass
	6CMIN10–9.1	0.134	6.47	2.55	0.492	3.67	1.18	4.34	0.70	1.81	Pass
	9CMIN10–9.1	0.094	9.23	1.88	0.258	2.75	1.14	3.14	0.67	1.76	Pass
	20CMIN10–9.1	0.050	7.54	1.78	0.091	1.81	1.13	2.06	0.67	1.75	Pass
	Average		7.04	2.26		3.62		4.13	0.69	2.42	Pass
Max9–10–3%	3CMAX10–9.1	0.381	4.94	2.78	2.049	5.38	1.11	5.95	0.71	1.82	Pass
	6CMAX10–9.1	0.219	5.12	2.82	1.011	4.62	1.18	5.45	0.72	1.83	Pass
	9CMAX10–9.1	0.153	6.43	2.51	0.302	1.98	1.18	2.33	0.70	1.80	Pass
	20CMAX10–9.1	0.082	4.85	2.22	0.156	1.90	1.16	2.21	0.69	1.78	Pass
	Average		5.34	2.58		3.47		3.99	0.70	2.47	Pass
20F–05–3%	20CMIN05–6.1	0.050	9.22	2.49	0.110	2.18	1.18	2.57	0.70	1.80	Pass
	20CMAX05–6.1	0.082	8.72	1.87	0.102	1.24	1.14	1.41	0.67	1.76	Fail
	20CMIN05–7.6	0.050	9.02	1.77	0.070	1.39	1.13	1.57	0.67	1.75	Fail
	20CMAX05–7.6	0.082	7.43	2.04	0.084	1.03	1.15	1.18	0.68	1.77	Fail
	20CMIN05–9.1	0.050	10.64	1.71	0.072	1.43	1.13	1.61	0.66	1.75	Fail
	20CMAX05–9.1	0.082	7.85	2.55	0.091	1.11	1.18	1.31	0.70	1.81	Fail
	Average		8.81	2.07		1.39		1.61	0.68	2.39	Fail

Table 4. Summary of collapse margin parameters and acceptance check for IMFs with ductile connections

Performance group	Arch.ID	Computed overstrength and collapse margin parameters							Acceptance check		
		S_{MT}	Ω	μ_T	S_{CT}	*CMR*	*SSF*	*ACMR*	β_{TOT}	Accept. *ACMR*	Pass /Fail
Min6–10–ductile	3CMIN10–6.1	0.233	5.09	5.31	1.908	8.18	1.17	9.59	0.73	1.84	Pass
	6CMIN10–6.1	0.134	6.41	5.26	0.683	5.10	1.29	6.59	0.73	1.84	Pass
	9CMIN10–6.1	0.094	9.19	2.95	0.498	5.31	1.20	6.39	0.72	1.84	Pass
	20CMIN10–6.1	0.050	4.75	6.17	0.255	5.07	1.32	6.70	0.73	1.84	Pass
	Average		6.36	4.92		5.92		7.32	0.73	2.53	Pass
Max6–10–ductile	3CMAX10–6.1	0.381	4.69	5.92	2.755	7.23	1.17	8.45	0.73	1.84	Pass
	6CMAX10–6.1	0.219	4.75	4.42	1.406	6.42	1.24	7.98	0.73	1.84	Pass
	9CMAX10–6.1	0.153	5.64	3.67	0.660	4.31	1.24	5.32	0.73	1.84	Pass
	20CMAX10–6.1	0.082	5.34	2.94	0.228	2.77	1.20	3.33	0.72	1.84	Pass
	Average		5.11	4.24		5.18		6.27	0.73	2.53	Pass
Min7–10–ductile	3CMIN10–7.6	0.233	4.90	4.90	1.911	8.19	1.16	9.54	0.73	1.84	Pass
	6CMIN10–7.6	0.134	6.46	4.16	0.752	5.61	1.25	7.04	0.73	1.84	Pass
	9CMIN10–7.6	0.094	9.02	3.05	0.367	3.92	1.21	4.73	0.73	1.84	Pass
	20CMIN10–7.6	0.050	6.46	2.83	0.150	2.98	1.20	3.56	0.72	1.83	Pass
	Average		6.71	3.73		5.18		6.22	0.72	2.53	Pass
Max7–10–ductile	3CMAX10–7.6	0.381	4.94	4.99	3.118	8.18	1.15	9.44	0.73	1.84	Pass
	6CMAX10–7.6	0.219	5.04	4.07	1.360	6.21	1.23	7.64	0.73	1.84	Pass
	9CMAX10–7.6	0.153	5.70	3.80	0.493	3.22	1.24	4.00	0.73	1.84	Pass
	20CMAX10–7.6	0.082	5.47	2.70	0.205	2.49	1.19	2.97	0.71	1.82	Pass
	Average		5.29	3.89		5.03		6.01	0.72	2.52	Pass
Min9–10–ductile	3CMIN10–9.1	0.233	4.92	5.17	1.941	8.32	1.17	9.73	0.73	1.84	Pass
	6CMIN10–9.1	0.134	6.51	4.51	0.809	6.04	1.27	7.65	0.73	1.84	Pass
	9CMIN10–9.1	0.094	9.49	3.06	0.383	4.09	1.21	4.95	0.73	1.84	Pass
	20CMIN10–9.1	0.050	7.54	2.10	0.138	2.74	1.16	3.17	0.68	1.77	Pass
	Average		7.12	3.71		5.30		6.38	0.71	2.50	Pass
Max9–10–ductile	3CMAX10–9.1	0.381	4.94	4.94	2.706	7.10	1.15	8.19	0.73	1.84	Pass
	6CMAX10–9.1	0.219	5.12	4.11	1.485	6.79	1.23	8.35	0.73	1.84	Pass
	9CMAX10–9.1	0.153	6.43	3.09	0.411	2.68	1.21	3.25	0.73	1.84	Pass
	20CMAX10–9.1	0.082	4.85	3.24	0.256	3.11	1.22	3.78	0.73	1.84	Pass
	Average		5.34	3.85		4.92		5.89	0.73	2.54	Pass
20F–05–ductile	20CMIN05–6.1	0.050	9.22	3.14	0.223	4.43	1.21	5.38	0.73	1.84	Pass
	20CMAX05–6.1	0.082	8.86	2.38	0.159	1.93	1.17	2.26	0.69	1.79	Pass
	20CMIN05–7.6	0.050	9.10	2.77	0.140	2.78	1.19	3.32	0.71	1.82	Pass
	20CMAX05–7.6	0.082	7.50	3.00	0.154	1.87	1.21	2.25	0.73	1.84	Pass
	20CMIN05–9.1	0.050	10.68	2.07	0.100	1.99	1.15	2.30	0.68	1.77	Pass
	20CMAX05–9.1	0.082	7.85	3.33	0.152	1.84	1.22	2.25	0.73	1.84	Pass
	Average		8.87	2.78		2.47		2.96	0.71	2.49	Pass

connections had a rotation capacity of 0.02 radian.

Fig. 8 shows the collapse probability of 20-story frames designed using ASCE 7-05 design seismic forces rather than using ASCE 7-10 design seismic forces. IMFs with a span length of 6.1m designed for SDC Cmin satisfied the criteria irrespective of the rotation capacity of their connections (Fig.8(a)). However, the frames with span lengths of 7.6m and 9.1 m satisfied the criteria only when they had ductile connections. It is noted that 20 story frames designed using the ASCE7-10 design seismic forces satisfied the criteria when their connections had a rotation capacity of 0.03 radian or larger.

As shown in Fig. 8(b), the collapse probabilities of 20 story IMF

frames designed for SDC Cmax using ASCE7-05 design seismic forces is much larger than those for SDC Cmin. Regardless of span length, the frames designed SDC Cmax failed to satisfy the criteria even though the rotation capacity of their connections was 0.03 radian. The frames were only satisfactory only when they had ductile connections. Note that, regardless of the level of SDC and connection rotation capacity, 20-story frames designed for ASCE7-10 design seismic forces (Fig.7(c)) satisfied the criteria when their connections had a rotation capacity of 0.03radian.

8_CONCLUSIONS

This study evaluated the seismic performance of steel intermediate moment frames designed considering different design parameters and seismic design forces. To conduct the seismic performance evaluation according to FEMA P695, three different rotation capacities of IMF connections were considered. The conclusions are summarized as follows:

Even though IMF connections had a rotation capacity of 2%, which is the minimum rotation capacity required by AISC 341-10, twelve IMFs failed the acceptance criteria among 30 model frames, and one performance group did not satisfy the acceptance criteria among 7 performance groups.

The number of stories significantly affected the probability of collapse for MCE ground motions. With an increase in the number of stories, the collapse probability became larger. The frames designed using ASCE 7-05 design seismic forces have larger collapse probability than that of the frames designed using ASCE 7-10. The probability of collapse was not significantly affected by different span lengths. The frames designed for SDC Cmax had a larger collapse probability than corresponding frames designed for SDC Cmin.

To satisfy the FEMA P695 criteria, it is recommended that nine-story (9-story) and twenty (20-story) IMFs designed using ASCE 7-10 design seismic forces should have a rotation capacity of 0.03 radian or larger.

The collapse probability of the 20-story frames designed using ASCE 7-05 seismic force was larger than that of the frames designed using ASCE 7-10 design seismic forces because ASCE 7-05 design seismic forces for the 20-story frame was lower than the ASCE 7-10 design seismic forces. Twenty story (20-story) IMFs designed using the ASCE 7-05 design seismic forces satisfied the acceptance criteria only when they had ductile connections.

ACKNOWLEGEMENTS

This study was supported by grants from the National Research Foundation of Korea (2014R1A2A1A11049488).

REFERENCES

1. Adam, C. and Jäger, C. (2012), "Simplified collapse capacity assessment of earthquake excited regular frame structures vulnerable to P-delta", Eng. Struct., 44, 159-173.
2. American Institute of Steel Construction. (2010), "Prequalified connections for special and intermediate steel moment frames for seismic applications", ANSI/AISC 358-10, Chicago, IL.
3. American Institute of Steel Construction. (2010), "Seismic provisions for structural steel buildings", ANSI/AISC 341-10, Chicago, IL.
4. American Institute of Steel Construction. (2010), "Specification for structural steel buildings", ANSI/AISC 360-10, Chicago, IL.
5. American Institute of Steel Construction. (2005), "Minimum design loads for buildings and other structures", ASCE/SEI 7-05, Reston, VA.
6. American Institute of Steel Construction. (2010), "Minimum design loads for buildings and other structures", ASCE/SEI 7-10, Reston, VA.
7. Anderson, J. and Duan, X. (1998), "Repair/Upgrade Procedures for Welded Beam to Column Connections", Pacific Earthquake Engineering Research center, Report No. PEER-98/03.
8. Chen, S.J., Yeh, C.H. And Chu J.M. (1996), "Ductile steel beam-to-column connections for seismic resistance", J. Struct. Eng., 122(11), 1292-1299.
9. Eads, L., Miranda, E., Krawinkler, H., and Lignos D.G.

(2013), "An efficient method for estimating the collapse risk of structures in seismic regions", Earthq. Eng. Struct. D., 42(1), 25-41.

10. Engelhardt MD., Fry, G., Jones, S., Venti, M. and Holliday, S. (2000), "Behavior and Design of Radius-Cut Reduced Beam Section Connections", Report No. SAC/BD-00/17, SAC Joint Venture. Sacramento, CA.
11. Elkady, A. and Lignos D.G. (2015), "Effect of gravity framing on the overstrength and collapse capacity of steel frame buildings with perimeter special moment frames", Earthq. Eng. Struct. D., 44(8), 1289-1307.
12. FEMA, (2009), "Quantification of Building Seismic Performance Factors", FEMA P695, SAC Joint Venture and FEMA, Washington, DC.
13. FEMA, (2000), "Recommended Seismic Design Criteria for New Steel Moment-Frame Buildings", FEMA 350, SAC Joint Venture and FEMA, Washington, DC.
14. FEMA, (2000), "State of the Art Report on Connection Performance", FEMA 355D, SAC Joint Venture and FEMA, Washington, DC.
15. FEMA, (2000), "State of the Art Report on Performance Prediction and Evaluation of Steel Moment-Frame Buildings", FEMA 355F, SAC Joint Venture and FEMA, Washington, DC.
16. FEMA, (2000), "State of the Art Report on Systems Performance of Steel Moment Frames Subject to Earthquake Ground Shaking", FEMA 355C, SAC Joint Venture and FEMA, Washington, DC.
17. Gupta, A. and Krawinkler, H. (1999), "Seismic demands for performance evaluation of steel moment resisting frame structures (SAC Task 5.4.3)", John A, Blume Earthquake Engineering Research Center, Rep. No. 132, Dept. Civil Engineering, Stanford University.
18. Hamidia, M., Filiatrault, A. and Aref, A. (2014), "Simplified seismic sidesway collapse analysis of frame buildings", Earthq. Eng. Struct. D., 43(3), 429-448.
19. Han, S.W., Kwon, G. and Moon, K.H. (2007), "Cyclic behavior of post-Northridge WUF-B connections", J. Constr. Steel Res., 63(3), 365-374.
20. Han, S.W., Moon, K.H. and Stojadinovic. B. (2009), "Design equations for moment strength of RBS-B connections", J. Constr. Steel Res., 65(5), 1087-1095.
21. Han, S.W., Moon, K.H., Hwang, S.H. and Stojadinovic. B. (2013), "Seismic performance evaluation of intermediate moment frames with reduced beam section and bolted web connections", Earthq. Spectra., 31(2), 895-919.
22. Iwankiw, N.R. and Carter, C. (1996), "Dogbone: a new idea to chew on", Mod. Steel Constr., 36(4), 18-23.
23. Jeong, S.H, Kwon, O.S. and Lee, K. (2015), "Effective periods and seismic performance of steel moment resisting frames designed for risk categories I and IV according to IBC 2009", Earthq. Eng. Struct. D., 44, 1427-1447.
24. Lee, C.H., Jeon, S.W., Kim, J.H. and Uang, C.M. (2005), "Effects of panel zone strength and beam web connection method on seismic performance of reduced beam section steel moment connections", J. Struct Eng., 131(12), 1854-1865.
25. Lee, K. and Foutch, D.A. (2002), "Seismic Performance Evaluation of Pre-Northridge Steel Frame Buildings with Brittle Connections", J. Struct. Eng., 128(4), 546-555.
26. Lignos, D.G. (2014), "Modeling of the composite action in fully restrained beam-to-column connections: implications in the seismic design and collapse capacity of steel special moment frames", Earthq. Eng. Struct. D., 43(13), 1935–1954. (Lignos 2008 neglect)
27. Luco, N. and Cornell, C.A. (2000), "Effects of connection fractures on SMRF seismic drift demands", J. Struct Eng., 126(1), 127-136.
28. Luco, N. and Cornell, C.A. (1998a), "Effects of random connection fractures on the demands and reliability for a 3-story pre-Northridge SMRF structure", Proceedings of the Sixth US National Conference on Earthquake Engineering, Seattle, Washington, May.
29. Luco, N. and Cornell, C.A. (1998b), "Seismic drift demands for two SMRF structures with brittle connections", First International Congress of Structural Engineers, San

Francisco, California, Washington, May.

30. Maison, B. and Kasai, K. (1997), "Analysis of Northridge damaged thirteen-story WSMF building", Earthq, Spectra., 13(3), 451-473.
31. Malley, J. (1998), "SAC steel project: Summary of phase 1 testing investigation results", Eng. Struct., 20(4-6), 300-309.
32. Mazzoni, S., McKenna, F., Scott, M.H. and Fenves, G.L. (2007), "OpenSees command language manual", The Univ. of California. Berkeley, Calif. Available from: http://opensees.berkeley.edu/index.php
33. Sotirov, P., Rangelov, N., Ganchev, O., Georgiev, T., Milev, J. and Petkov, Z. (2000), "Influence of haunching", Moment resisting connections of steel frames in seismic area, design and reliability, E& FN SPON. [Chapter 3.3].
34. Stojadinovic, B., Goel, S.C. and Lee, K.H. (2000), "Parametric test on unreinforced steel moment connections", J. Struct. Eng., 126(1), 40-49.
35. Tsai, K.C. and Chen, C.Y. (1996), "Performance of Ductile Steel Beam-Column Moment Connections", Eleventh World Conference on Earthquake Engineering, Acapulco, Mexico, August.
36. Tremblay, R., Tchebotarev, N. and Filiatrault, A. (1997) "Seismic performance of RBS connections for steel moment resisting frames: Influence of loading rate and floor slab", Proceedings STESSA '97, Kyoto, Japan, August.
37. Qi, Y., Gu. Q. and Li. D. (2012), "Efficient and automated method of collapse assessment", Steel Compos. Struct., 13(6), 561-570.